

Lattice Gauge Theory with Fixed Point Actions

Inauguraldissertation
der Philosophisch-naturwissenschaftlichen Fakultät
der Universität Bern

vorgelegt von

Urs Wenger

von Strättligen (BE)

Leiter der Arbeit: Prof. P. Hasenfratz
Institut für theoretische Physik
Universität Bern

Lattice Gauge Theory with Fixed Point Actions

Inauguraldissertation
der Philosophisch-naturwissenschaftlichen Fakultät
der Universität Bern

vorgelegt von

Urs Wenger

von Strättligen (BE)

Leiter der Arbeit: Prof. P. Hasenfratz
Institut für theoretische Physik
Universität Bern

Von der Philosophisch-naturwissenschaftlichen Fakultät angenommen.

Der Dekan:

Bern, den 18. Mai 2000

Prof. Dr. A. Pfiffner

Contents

1	Introduction and summary	1
2	A new parametrization of the FP action for SU(3) lattice gauge theory	5
2.1	Introduction	5
2.2	The FP action	6
2.3	The parametrization	7
2.4	The quadratic approximation	9
2.5	The FP action on rough configurations	9
2.6	Summary and conclusion	13
3	The deconfining phase transition in pure Yang-Mills theory	15
3.1	Introduction	15
3.2	Finite temperature in lattice gauge theory	16
3.3	The phase structure of lattice gauge theory	21
3.3.1	Polyakov loop correlator as the order parameter of the phase transition	21
3.3.2	Center symmetry	23
3.4	Determination of the temporal scale	24
3.5	Determination of the critical couplings	28
3.5.1	Simulation details	29
3.5.2	Analysis details	31
3.5.3	Error estimation	37
3.6	Conclusions and outlook	40
4	Scaling properties of the FP action	42
4.1	Introduction	42
4.2	Scaling of the static quark-antiquark potential	43
4.2.1	The static potential	44
4.2.2	Determination of the spatial scale	45
4.2.3	Simulation details	46
4.2.4	Analysis details and results	48
4.3	Scaling of the critical temperature and $r_0\sqrt{\sigma}$	52
4.3.1	$T_c/\sqrt{\sigma}$	53
4.3.2	r_0T_c	54
4.3.3	$r_0\sqrt{\sigma}$	58
4.4	Conclusions and outlook	59

5	Glueballs	61
5.1	Introduction	61
5.2	Glueball operators from Wilson loops	62
5.2.1	Glueball states	63
5.2.2	Construction of basis functions of irreducible representations	64
5.2.3	Irreducible representations of the cubic group on Wilson loops	65
5.3	Simulation details	69
5.4	Analysis details	70
5.4.1	Results	71
5.4.2	Signal/noise ratio of the operators	75
5.5	Conclusions and outlook	76
6	Conclusions and outlook	77
A	The $\mathcal{O}(a^2)$ and $\mathcal{O}(a^4)$ Symanzik conditions	79
A.1	The $\mathcal{O}(a^2)$ Symanzik conditions	79
A.2	Conditions from constant abelian gauge fields	80
B	Instanton classical solutions on the lattice	83
B.1	Construction of SU(2) single instanton configurations	84
B.2	Results and comments on SU(2) single instanton configurations .	85
C	The Ferrenberg-Swendsen reweighting	90
C.1	The single-histogram reweighting	90
C.2	The multi-histogram reweighting	92
C.3	Reweighting at first order phase transitions	96
D	Extracting masses from correlation functions	100
D.1	Variational techniques	101
D.2	Correlated fits	102
E	The cubic point group O_h	104
E.1	The group elements of O_h	104
E.2	The character table	106
E.3	Wave functions of glueball operators	106
F	Collection of data	115
F.1	Data from the static potential	115
F.2	Data from the glueball simulations	117

Chapter 1

Introduction and summary

Quantum chromodynamics (QCD) has been the generally accepted theory of strong interactions over the last 20 years. However, basic features of non-perturbative low-energy QCD physics, such as the spectrum or the structure of hadrons, have proven to be notoriously difficult to calculate.

One way of doing non-perturbative calculations is by using a discrete space-time lattice as an ultraviolet regulator [1]. The QCD action is discretized by replacing space-time integrals with sums and derivatives with finite differences. Then the path integral defining the field theory can be evaluated numerically using for example Monte Carlo techniques. The main problem for such numerical lattice calculations, however, is the control of lattice artifacts which are introduced through the finite lattice spacing a .

The standard discretization of the QCD action is the Wilson gauge action in the pure gauge sector and the Wilson Dirac action in the fermionic sector. These discretized actions introduce errors of $\mathcal{O}(a^2)$ and $\mathcal{O}(a)$, respectively, which are large when the lattice spacing is larger than $a \simeq 0.1$ fm. On the other hand, typical maximal lattice sizes which can be simulated in quenched QCD with high statistics on computers in the 10 GFLOPS range are around $32^3 \times 64$. For full QCD this marks the maximal lattice size for obtaining reliable results even with the most powerful TFLOPS-class computers like CP-PACS and QCDSF currently available to the lattice community. Reflecting the fact that the needed physical lattice sizes are around $L \simeq 2.0 - 3.0$ fm in order to avoid finite volume effects, the smallest lattice spacing accessible with reasonable effort is of the order of $a \simeq 0.1 - 0.2$ fm. These observations suggest the use of improved discretizations of lattice actions, for which finite lattice spacing errors are removed or at least dramatically reduced. This can be achieved by systematically introducing new irrelevant interactions into the lattice actions. Among the approaches proposed, there are methods using perturbatively calculated correction terms in order to improve the lattice gauge action beyond $\mathcal{O}(a^2)$, like the Symanzik program or the meanfield and tadpole improvement approach.

An entirely different approach is suggested by Hasenfratz and Niedermayer [2], namely to use perfect lattice actions, which are completely free of lattice artifacts. According to Wilson's renormalization group (RG) theory such quantum

perfect actions follow the renormalized trajectory under repeated RG transformation steps and describe the long-distance physics of the theory properly at any finite lattice spacing. The RG trajectory runs into the fixed point (FP) of the RG transformation in the continuum and forms the FP action. The FP action at finite coupling values is classically perfect, that is, it reproduces all the physical properties of the classical action in the continuum at finite lattice spacing, and is thought to be a very good approximation to the quantum perfect action. As was pointed out in [2], the determination of the classically perfect FP action in the continuum limit reduces to a saddle-point problem for asymptotically free theories. This approach was successfully applied to the two-dimensional non-linear σ -model [2, 3] and the two-dimensional CP^3 model [4]. For the $SU(3)$ gauge theory the classically perfect FP action was constructed and tested in [5, 6, 7, 8] and the ansatz was extended to include FP actions for fermions as well [9, 10]. In the case of $SU(2)$ gauge theory the FP action was constructed in [11, 12, 13], and its classical properties were tested on classical instanton solutions, both in $SU(2)$ and $SU(3)$ [14]. In this context, the question arises whether one can find a simple but flexible parametrization which is still easy to simulate. The need for a new parametrization which can describe the FP action arbitrarily precise becomes even more urgent regarding the recent developments in the fermionic sector, where the FP Dirac operator was shown to fulfill the Ginsparg-Wilson relation assuring nice properties related to chiral symmetry on the lattice [15, 16]. In view of the computational cost related to the FP Dirac operator (inversion, determinant), the expense for a well parametrized FP gauge action becomes almost negligible and an additional effort in finding an improved parametrization of the FP gauge action is justified. It is mainly on the background of these considerations that the present work has to be seen.

The new parametrization on which we report in this work has a much richer structure and is much more flexible than the ones previously studied. However, using a more complex parametrization naturally incorporates the danger of overshooting and doing things wrong. Therefore the main part of the work is devoted to study the properties of the parametrized FP action in order to assure that no instabilities are introduced through the more complex parametrization. In addition, one would like to have unquestionable confidence in the parametrized FP action for the whole range of coarse lattice spacings at which the action will be used in future applications.

Additionally, one would like to produce interesting physical results using a very different formulation of lattice gauge theory in order to confirm universality. Universality is the generally accepted assumption that in the continuum limit, where the lattice spacing goes to zero, the physically meaningful quantities do not depend on the actual discretization, but contain only a few relevant parameters.

The work presented here has been mostly accomplished in collaboration with Philipp R ufenacht and Ferenc Niedermayer. In the following we give an outline of the work and summarize the main results.

In chapter 2 we present the construction and parametrization of a FP gauge action on the lattice starting from the analytically calculated couplings of the FP action in the quadratic approximation, where care was taken not to vio-

late the $\mathcal{O}(a^2)$ Symanzik conditions. Emphasis is laid on how the FP action is parametrized at lattice spacings suitable for performing simulations on coarse lattices and it is pointed out that the parametrization respects approximate scale invariance of instanton solutions. We briefly comment on the computational cost of the parametrized FP action and, in this context, on its usefulness and importance in possible practical applications. Some technical details on how $\mathcal{O}(a^2)$ and $\mathcal{O}(a^4)$ Symanzik conditions can be calculated analytically are relegated to appendix A, while appendix B contains details on how to put single instanton solutions on a periodic lattice and on the process of the falling through the lattice of such classical instanton solutions.

Chapter 3 deals with the finite temperature deconfining phase transition in pure gauge theory and the determination of the critical temperature T_c . Some effort is spent on how finite temperature is introduced in lattice gauge theory in a clean way and how Polyakov loop correlators figure as an order parameter for the phase transition. For the purpose of subjecting the parametrized FP action to scaling tests we determine its critical couplings β_c on lattices with temporal extensions $N_\tau = 2, 3$ and 4. For each N_τ we perform simulations on several lattices for a finite size scaling study. Emphasis is put on the error calculation and estimation of the critical couplings. Technical details on the Ferrenberg-Swendsen reweighting used for the determination of the critical couplings are postponed to appendix C, where the machinery is set up and tested on the two-dimensional Ising and 10-state Potts model.

In chapter 4 the parametrized FP action is subject to several scaling tests. Using spatially smeared Wilson loops we measure the static quark-antiquark potential at various values of the gauge coupling and examine its scaling behavior. From the potentials we extract the commonly used reference scale r_0 and an effective string tension σ in order to check the scaling behavior of the renormalization group invariant quantities $r_0 T_c$, $T_c/\sqrt{\sigma}$ and $r_0\sqrt{\sigma}$. Despite the fact that the determination of the reference scale r_0 is hampered by systematic ambiguities even at modest lattice spacings around $a \simeq 0.1$ fm, when different but equivalent methods are applied, we observe excellent scaling of the parametrized FP action on the one percent level down to coarse lattice spacings of around $a \simeq 0.33$ fm. Details on variational techniques and correlated fits, which are employed for extracting potential energies from correlation functions of Wilson loops, can be found in appendix D.

In the following the parametrized FP action is extensively tested on the glueball spectrum in chapter 5. We describe the construction of glueball operators from Wilson loops up to length eight and we review, in the context of glueballs, some aspects of representation theory in general and of the cubic group in particular. We perform several large simulations and measure the glueball spectrum in all 20 symmetry channels. However, due to the coarse lattice spacings, we are able to resolve only a few lowest lying glueball masses. The lowest lying 0^{++} channel shows particularly large cut-off effects, when measured with the Wilson gauge action, and therefore provides an excellent candidate for testing the improvements achieved with the parametrized FP action. Indeed, we observe much reduced lattice artifacts as compared to the Wilson gauge action even at moderate lattice spacings between $a \simeq 0.10 - 0.18$ fm and the parametrized FP

action shows a perfect scaling behavior. Performing the continuum limit for this channel we obtain an estimate of 1627(83) MeV for the 0^{++} glueball mass and 2354(95) MeV for the 2^{++} glueball mass¹.

The last chapter finally contains some general conclusions and prospects for the future.

¹Only the 0^{++} value represents a continuum extrapolation, while the 2^{++} value corresponds to the one measured at a lattice spacing of $a = 0.10$ fm.

Chapter 2

A new parametrization of the FP action for $SU(3)$ lattice gauge theory

2.1 Introduction

While the FP action can be calculated numerically to arbitrary precision in principle, one has to resort to an approximate parametrization of the FP action in practice due to limited computer power. It turns out, that finding an appropriate parametrization is not an easy task.

In this chapter we present a new ansatz for the parametrization which is very general and flexible, and which allows to parametrize the FP action using more and more couplings without any further complications. Nevertheless, it is still easy to handle in contrast to earlier attempts. The approach we use is building simple loops (plaquettes) from single gauge links as well as smeared links. In this manner we are able to reproduce the classical properties of the FP action excellently.

The new ansatz is motivated by the success of using fat links in simulations with fermionic Dirac operators [17, 18, 19]. Fat links are gauge links, which are locally smeared over the lattice. In this way the unphysical short-range fluctuations inherent in the gauge field configurations are averaged out and lattice artifacts are reduced dramatically [20]. It is mainly in view of possible future applications of the FP gauge action in connection with FP Dirac operators that a new and more accurate parametrization of the FP action is undertaken.

Earlier parametrizations of FP actions were based on powers of the traces of loop products along generic closed paths [6]. Restricting the set of paths for production runs to loops of length 8 or less and fitting in a 2^4 hypercube, one is still left with 28 topologically different loops, some of them having a multiplicity as large as 384. In addition, it turned out that the quality of the parametrization of the FP action did not improve upon enlarging the set beyond the 12

most important loop paths. Presumably this is an indication of the fact that loop paths beyond length 8 are important for an accurate parametrization of the FP action. However, when extending this earlier ansatz beyond Wilson loops of length 8, it becomes nearly impossible to keep track of all topologies and multiplicities, and the computational overhead is unaffordable. That such an extension is needed is evident also from studies of topology with the FP gauge action [14, 13], where it became clear that at least one operator of length eight has to be included. Such an extension, however, already introduces a computational overhead factor of 35-225 compared to the Wilson action.

The new parametrization presented here provides a way around these problems. Although the computational overhead is still considerable, the ansatz is flexible enough to easily respect scale invariance of instanton solutions and is therefore expected to describe the classical and topological properties of the pure gauge theory properly. Equally important is the capability of the new parametrization to be extendable without further complications and with only a slight additional effort in order to describe the FP action more and more accurately.

The rest of this chapter is organized as follows. In the first section we will very briefly review the essential ingredients forming the FP action approach without giving arguments on its working mechanism. In section 2.3 we will present the general ansatz for the parametrization and then calculate the couplings of the FP action in quadratic approximation while taking care of the $\mathcal{O}(a^2)$ Symanzik conditions in section 2.4. In section 2.5 we will explain in detail the construction of a parametrized FP action suitable for simulations on coarse lattices in physically interesting regions. We will check that the parametrization respects approximate scale invariance of instanton solutions. It is pointed out that the action is especially suited for the use in Monte Carlo simulations, since we are not only parametrizing the FP action values but also the derivatives with respect to the gauge fields as well. Finally, we add some remarks about the computational overhead of the parametrized FP action in the last section and give an estimation of its usefulness in possible applications.

2.2 The FP action

We consider $SU(N)$ pure gauge theory¹ in four dimensional Euclidean space defined on a periodic lattice. The partition function is defined through

$$Z(\beta) = \int dU e^{-\beta \mathcal{A}(U)}, \quad (2.1)$$

where dU is the invariant group measure and $\beta \mathcal{A}(U)$ is some lattice regularization of the continuum action. We can perform a real space renormalization group transformation (RGT),

$$e^{-\beta' \mathcal{A}'(V)} = \int dU \exp -\beta(\mathcal{A}(U) + T(U, V)), \quad (2.2)$$

¹The following equations are given for general N , although the numerical analysis and simulations are done for $SU(3)$.

where V is the blocked link variable and $T(U, V)$ is the blocking kernel defining the transformation,

$$T(U, V) = -\frac{\kappa}{N} \sum_{n_B, \mu} (\text{ReTr}(V_\mu(n_B) Q_\mu^\dagger(n_B)) - \mathcal{N}_\mu^\beta). \quad (2.3)$$

Here, $Q_\mu(n_B)$ is a $N \times N$ matrix representing some mean of products of link variables $U_\mu(n)$, connecting the sites $2n_B$ and $2(n_B + \hat{\mu})$ on the fine lattice and \mathcal{N}_μ^β is a normalization constant ensuring the invariance of the partition function. By optimizing the averaging function in Q_μ and the parameter κ , it is possible to obtain an action on the coarse lattice, which has a short interaction range. Such an optimization has been done and we refer to [8] for the explicit form of the RGT block transformation. The main idea of the RGT III block transformation is that, instead of using just simple staples, one additionally builds 'diagonal staples' along the planar and spatial diagonal directions orthogonal to the link direction. In this way one achieves that each link on the fine lattice contributes to the averaging function.

On the critical surface at $\beta \rightarrow \infty$ equation (2.2) becomes a saddle point problem representing an implicit equation for the FP action, \mathcal{A}^{FP} ,

$$\mathcal{A}^{\text{FP}}(V) = \min_{\{U\}} \{\mathcal{A}^{\text{FP}}(U) + T(U, V)\}. \quad (2.4)$$

The normalization constant in the blocking kernel, \mathcal{N}_μ^β , becomes in the limit $\beta \rightarrow \infty$

$$\mathcal{N}_\mu^\infty = \max_{W \in \text{SU}(N)} \{\text{ReTr}(W Q \mu^\dagger)\}. \quad (2.5)$$

The FP equation (2.4) can be studied analytically up to quadratic order in the vector potentials [8]. However, for solving the FP equation on coarse configurations with large fluctuations one has to resort to numerical methods, and a sufficiently rich parametrization for the description of the solution is required.

2.3 The parametrization

The approach we use for the parametrization is building simple loops (plaquettes) from single gauge links as well as from smeared links. The smeared links are built out of staples of gauge links and depend on the plane of the plaquette to which they are contributing.

Let us introduce the notation $S_\mu^{(\nu)}(n)$ for the sum of two staples of gauge links in direction μ in the $\mu\nu$ -plane²:

$$S_\mu^{(\nu)}(n) = U_\nu(n) U_\mu(n + \hat{\nu}) U_\nu^\dagger(n + \hat{\mu}) + U_\nu^\dagger(n - \hat{\nu}) U_\mu(n - \hat{\nu}) U_\nu(n - \hat{\nu} + \hat{\mu}). \quad (2.6)$$

²Following the notation introduced in [21] this is equivalent to $S_\mu^{(\nu\pm)}$, where the subscript denotes the direction of the staple and the superscript specifies the plane $\mu\nu$ and the parity in ν .

We shall use besides the usual symmetric smearing also a non-symmetric smearing. For the symmetric smearing define

$$Q_\mu^s(n) = \frac{1}{6} \sum_{\lambda \neq \mu} S_\mu^{(\lambda)}(n) - U_\mu(n) \quad (2.7)$$

and

$$x_\mu(n) = \text{Re Tr} (Q_\mu^s(n) U_\mu^\dagger(n)) . \quad (2.8)$$

To build a plaquette in the $\mu\nu$ -plane from smeared links it is convenient to introduce asymmetrically smeared links. First define³

$$Q_\mu^{(\nu)} = \frac{1}{4} \left(\sum_{\lambda \neq \mu, \nu} S_\mu^{(\lambda)} + \eta(x_\mu) S_\mu^{(\nu)} \right) - \left(1 + \frac{1}{2} \eta(x_\mu) \right) U_\mu . \quad (2.9)$$

Using these matrices we build the asymmetric smeared links

$$W_\mu^{(\nu)} = U_\mu + c_1(x_\mu) Q_\mu^{(\nu)} + c_2(x_\mu) Q_\mu^{(\nu)} U_\mu^\dagger Q_\mu^{(\nu)} + \dots . \quad (2.10)$$

Here $\eta(x)$, $c_i(x)$ are polynomials with free coefficients, to be determined later by a fit to the FP action,

$$\eta(x_\mu) = \eta^{(0)} + \eta^{(1)} x_\mu + \eta^{(2)} x_\mu^2 + \dots \quad (2.11)$$

and

$$c_i(x_\mu) = c_i^{(0)} + c_i^{(1)} x_\mu + c_i^{(2)} x_\mu^2 + \dots \quad (2.12)$$

These asymmetrically smeared links are no longer elements of the SU(3) gauge group, but they can be projected back to the nearest element in the SU(3) gauge group. However, the projection is expensive for the use in actual simulations and in addition our numerical studies have shown that this is not really necessary but reduces the degrees of freedom in defining the action, such that for larger fluctuations the FP action cannot be fitted accurately enough. We will thus use the smeared links $W_\mu^{(\nu)}$ as they are.

From these asymmetrically smeared links we construct a 'smeared plaquette' variable

$$w_{\mu\nu} = \text{Re Tr} (1 - W_{\mu\nu}^{\text{pl}}) , \quad (2.13)$$

and the ordinary Wilson plaquette variable

$$u_{\mu\nu} = \text{Re Tr} (1 - U_{\mu\nu}^{\text{pl}}) , \quad (2.14)$$

where

$$W_{\mu\nu}^{\text{pl}}(n) = W_\mu^{(\nu)}(n) W_\nu^{(\mu)}(n + \hat{\mu}) W_\mu^{(\nu)\dagger}(n + \hat{\nu}) W_\nu^{(\mu)\dagger}(n) , \quad (2.15)$$

and

$$U_{\mu\nu}^{\text{pl}}(n) = U_\mu(n) U_\nu(n + \hat{\mu}) U_\mu^\dagger(n + \hat{\nu}) U_\nu^\dagger(n) . \quad (2.16)$$

³The argument n is suppressed in the following.

Finally, the parametrized action has the form

$$\mathcal{A}[U] = \frac{1}{N} \sum_{\mu < \nu} f(u_{\mu\nu}, w_{\mu\nu}), \quad (2.17)$$

where we choose a polynomial in both plaquette variables,

$$\begin{aligned} f(u, w) &= \sum_{kl} p_{kl} u^k w^l \\ &= p_{10}u + p_{01}w + p_{20}u^2 + p_{11}uw + p_{02}w^2 + \dots \end{aligned} \quad (2.18)$$

Again, the coefficients p_{kl} are free parameters and will be determined later, so that the FP action is approximated closely.

2.4 The quadratic approximation

The couplings of the FP action can be calculated analytically in the quadratic approximation [6, 8]. By fitting the leading order nonlinear parameters $\eta^{(0)}$, $c_1^{(0)}$, $c_2^{(0)}$ and p_{10}, p_{01} to the quadratic part of the FP action we can check the flexibility and the quality of the parametrization. Of course every (approximate) parametrization introduces $\mathcal{O}(a^2)$ artifacts and violates the nice properties of the FP action, however, one can exploit the freedom in the parametrization to correct for this and to explicitly fulfill the Symanzik ('on-shell') conditions⁴ up to $\mathcal{O}(a^2)$ or even $\mathcal{O}(a^4)$. In this way the linear parameters p_{10} and p_{01} are determined as functions of the rest by the norm and the $\mathcal{O}(a^2)$ Symanzik condition. The fit in the three nonlinear parameters yields the following result:

$$\eta^{(0)} = 0.082, \quad c_1^{(0)} = 0.282, \quad c_2^{(0)} = 0.054, \quad (2.19)$$

with the corresponding plaquette coefficients

$$p_{10} = -0.3681, \quad p_{01} = 0.6292. \quad (2.20)$$

It is interesting to note that for the present ansatz of the parametrization the second $\mathcal{O}(a^2)$ Symanzik condition is automatically fulfilled. The action, where only the leading parameters are present, is denoted by $\mathcal{A}_0(U)$ and is a good approximation to the FP action for sufficiently small fields.

Checks involving simple configurations with only one or two non-trivial links sufficiently close to unity, show that $\mathcal{A}_0(U)$ approximates indeed well the FP action to quadratic order, in fact the relative error between $\mathcal{A}_0(U)$ and the true FP action value is found to be less than 2%.

For simulations with the FP action in physically interesting regions it is important to have a parametrization for gauge fields on coarse lattices. We turn to this problem in the next section.

2.5 The FP action on rough configurations

The parametrization of the FP action on strongly fluctuating fields is a difficult and delicate problem. In this section we describe briefly the procedure of

⁴For details on the $\mathcal{O}(a^2)$ and $\mathcal{O}(a^4)$ Symanzik conditions see appendix A.

obtaining a parametrization, which uses only a compact set of parameters, but which describes the FP action still sufficiently well for the use in actual simulations. We also provide some details about the fitting procedure used.

Obtaining the FP action values on rough configurations involves a multi-grid procedure. One starts with configurations $\{V\}$ on a coarse lattice and applies inverse blocking steps to obtain finer configurations $\{U^{(n)}\}$, $n = 1, 2, \dots$:

$$\{V\} \rightarrow \{U^{(1)}\} \rightarrow \{U^{(2)}\} \rightarrow \dots \rightarrow \{U^{(k)}\}. \quad (2.21)$$

In each step the fluctuations of the fields are typically reduced by a factor of 30 to 40 and after a sufficiently large number of steps k the fine configuration $\{U^{(k)}\}$ is so smooth that any discretization of the gauge action can be used on it. In practise, however, memory and time prevents from doing more than one step at once and one has to resort to building the FP action iteratively.

Starting on the finest level with configurations for which the quadratic approximation \mathcal{A}_0 is appropriate, one ends up with physically interesting configurations and a suitable parametrization of the FP action after three or four steps. On each intermediate level one has to find a new parametrization which describes the FP action accurately enough and it shows that one has to include more and more parameters on each level to do so. However, since these intermediate FP actions are not intended to be used in simulations, one can be generous with respect to the numbers of parameters included. This is no longer the case for the last step, where we restricted ourselves to the smallest possible set of parameters, which still meets our requirements for the accuracy of the action.

During this iterative procedure it turned out to be favorable to release from the $\mathcal{O}(a^2)$ Symanzik condition and, indeed, it is not clear how important it is in the presence of large fluctuations. In this sense the final action is only intended to work in a given range of fluctuations, which, however, covers the physically interesting fluctuations accessible with today's computer power.

The determination of the coefficients of the intermediate and the final parametrization is done by minimizing a χ^2 -function involving the derivatives of the gauge action with respect to the gauge links in a given colour direction a (N_c denoting the number of colours),

$$\frac{\delta \mathcal{A}(U)}{\delta U_\mu^a(n)}, \quad \mu = 1, \dots, 4 \text{ and } a = 1, \dots, N_c^2 - 1, \quad (2.22)$$

the action values of the FP action on equilibrated configurations and, maybe somewhat less important, on classical solutions of the FP action. The values to be fitted are calculated using the information we have about the fine configuration. Fitting the derivatives has the advantage that one single configuration provides $V \cdot (N_c^2 - 1) \cdot 4$ residues, where V is the volume of the lattice, instead of just one for the action value. As the inverse blocking involves minimization of the fine configuration, which is quite expensive, the approach reduces computing time considerably. In addition what counts in MC simulations are really the local changes of the action and not the total action value itself, thus the present FP action is especially suited for the use in MC simulations. However, one has to keep in mind that not all of the residues are independent from each other and we carefully checked that enough independent information is included in the fit. An interesting and important test for the flexibility of the parametrization is

whether both the requirements for fitting the derivatives and the action values can be met at the same time and it shows that this is indeed the case.

For addressing questions concerning topology it turned out to be crucial to include scale-invariant instanton solutions [11, 12, 13, 14]. A good parametrization of the FP action should also be able to respect approximate scale invariance of instanton solutions. For this purpose we generated sets of SU(2) single instanton configurations on a 12^4 lattice with instanton radius ρ/a ranging from 3.0 down to 1.1 centered in a hypercube, in a cube and in a plaquette⁵. We then blocked the configurations down to a 6^4 lattice to get approximate classical solutions. In fact it turns out that they are classical solutions of the FP action for radii larger than $\rho/a \sim 0.88$ as can be seen for example from figure 2.1.

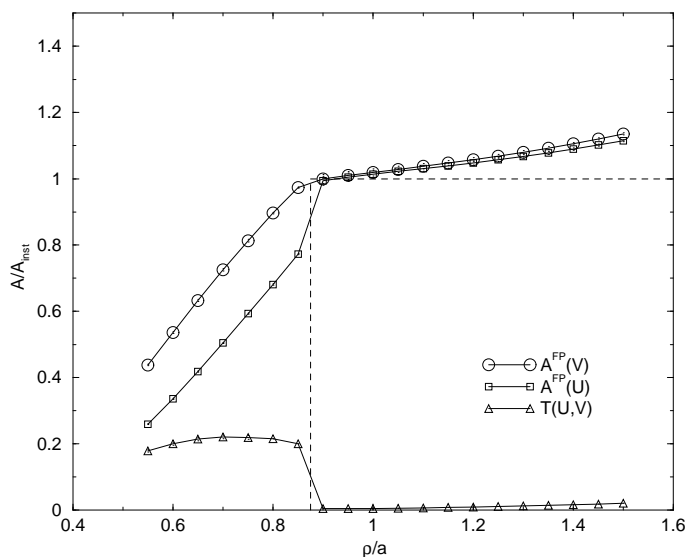


Figure 2.1: SU(2) single instanton solutions on a 6^4 lattice with center of the instanton at $x_c/a = (2\frac{3}{4}, 2\frac{3}{4}, 2\frac{3}{4}, 2\frac{3}{4})$, a being the lattice spacing on the coarse lattice. V is the coarse configuration and U denotes the minimized configuration on the fine lattice. Note, that $A^{\text{FP}}(V) = A^{\text{FP}}(U) + T(U, V)$ and that for an exact classical solution of the FP action one has $T(U, V) = 0$.

In figure 2.2 we show how the present parametrization works on the example of instanton solutions centered in a cube. The solid lines are extrapolations from finite lattices with $L = 4, 6, 8$ to an infinite lattice. The action values are expressed in units of the one instanton action value in the continuum, $A_{\text{inst}} = 4\pi^2$.

In the last step we first fitted the derivatives on ~ 50 thermal configurations corresponding to a Wilson critical coupling at $N_\tau = 3$, $\beta_c^W \approx 5.4$. In the following the non-linear parameters were kept fixed, while we included in addition the action values and the derivatives of ~ 75 thermal configurations at $\beta^{\text{FP}} = 2.8, 4.0, 7.0$ and the action values of the instanton configurations. Since

⁵For a detailed prescription of how the instanton configurations are generated we refer to appendix B, where we also add some remarks about the minimization of such solutions, i.e. the mechanism of the falling through the lattice.

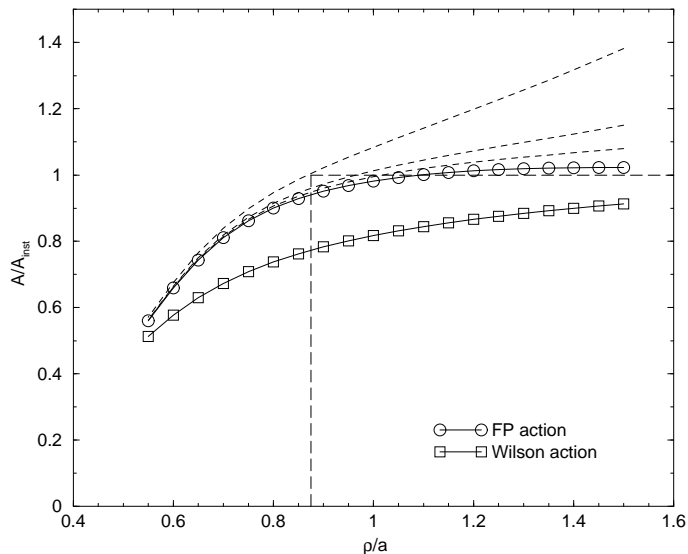


Figure 2.2: SU(2) single instanton solutions centered inside a spatial cube. The solid lines are extrapolations to infinite lattice. For the parametrized FP action we also plot the values of the action on lattices with size $L = 4, 6, 8$ as dashed lines.

the non-linear parameters are kept fixed we use this information only to optimize in this way the linear parameters.

To assure stability of the fit we employed different checks: first we checked that the χ^2 was stable on independent configurations, which were not included in the fit. Secondly, we successively excluded different parts of the fitted data to check the stability of the data sets and, thirdly, we checked stability under variation of the relative weights with which the different data sets were included in the fit. Using high order polynomials of the plaquette variables u and w there is always the danger of generating non-positive regions in the uw -plane. We found that this can usually be circumvented by choosing an appropriate set of linear parameters p_{kl} .

The smallest acceptable set of parameters we found consists of four non-linear parameters, $\eta^{(0)}, c_1^{(0)}, c_2^{(0)}, c_3^{(0)}$ and fourteen linear parameters p_{kl} with $0 < k + l \leq 4$. The values of these parameters are given in table 2.1 and fulfill the correct normalization. They form the final approximation of the FP action.

It is clear that by restricting ourselves to a small set of parameters we can not describe all the properties of the FP action accurately enough, but in contrast, through the truncation in the parameter space we introduce lattice artifacts of any order. Therefore the approximate FP action will be subjected to a number of scaling tests in order to ensure the successful and correct parametrization of the FP action and in order to size possible lattice artifacts. In the following, when we speak of the FP action in the context of practical applications, we really mean the parametrized and therefore approximate FP action described in this chapter.

	$\eta^{(0)}$	$c_1^{(0)}$	$c_2^{(0)}$	$c_3^{(0)}$	
	-0.038445	0.290643	-0.201505	0.084679	
p_{0i}		0.442827	0.628828	-0.677790	0.176159
p_{1i}	0.051944	-0.918625	1.064711	-0.275300	
p_{2i}	0.864881	-0.614357	0.165320		
p_{3i}	-0.094366	-0.020693			
p_{4i}	0.022283				

Table 2.1: Parameters of the approximate FP action.

2.6 Summary and conclusion

Before we can appreciate the value and usefulness of the new parametrization, some comments are in order concerning the computational overhead.

We have calculated the expense of the parametrized FP action and compared it to the expense of an optimized Wilson gauge code. The computational overhead amounts to a factor of 55-60 and comes mainly from computing the smeared links. Once these links are calculated one can generate (compact) loops up to arbitrary length just by including more and more powers of the smeared links. The present parametrization therefore allows to reach an almost arbitrarily rich parametrization of the FP action with no further complications whatsoever. In contrast, this was not the case for the older parametrizations, which were using powers of simple Wilson loops up to a given length, since going beyond loops of length eight turned out to be impossible in practice. Reflecting these facts the computational overhead is certainly justified.

Of course, the overhead is a severe drawback for the use of the action in actual simulations as will be clear in the next chapters. Although the action shows much reduced lattice artifacts as compared to the Wilson action, it is not clear if the extra work pays off in pure gauge theory at zero temperature. Indeed, a fair competition for different actions is to compare results which are obtained with the same computational effort. Allowing therefore the same amount of simulation time to the Wilson action one could simulate on lattices which are around 2.7 times finer than the ones accessible to the FP action at the moment. This corresponds to a lattice spacing of around $a \simeq 0.04$ fm or a Wilson coupling $\beta^W \simeq 6.6$, which is already far in the continuum. Of course, it is not clear how these considerations are modified when the continuum is approached: due to critical slowing down, missing overlap of simple loop operators with physical objects, like in the case of glueball operators, the simulation cost is likely to grow as a^{-6} , when the lattice spacing is reduced, and the above factor of 2.7 is by far exaggerating. In particular, it is known that for thermodynamic quantities the computational effort grows proportional to a^{-10} suggesting a factor in the lattice spacing of ~ 1.5 instead. Thus, thermodynamics of SU(3) lattice gauge theory is surely a field of practical applications for the FP action.

Another remark in favour of the FP action concerns the use of it in connection with a fermionic FP Dirac operator, i.e. the application of the FP gauge action in full QCD. In view of the expense for a Dirac operator in dynamical simulations the overhead coming from the FP gauge action is only a slight drawback and can easily be afforded. In addition, one knows that FP gauge actions prefer

gauge fields with smaller fluctuations compared to the Wilson gauge action at the same lattice spacing. Thus inversions of Dirac operators will converge faster on gauge configurations generated with the FP action thereby compensating the overhead coming from it.

Recapitulating it is fair to say, that the parametrized FP gauge action in combination with the FP Dirac operator in QCD simulations opens the interesting possibility to keep chiral symmetry and reduce the cut-off effects at the same time. In these applications the overhead comes almost entirely from the Dirac operator, while the overhead from the gauge action is negligible. For applications in pure gauge theory, however, the use of the parametrized FP gauge action has to be chosen thoughtfully.

Chapter 3

The deconfining phase transition in pure Yang-Mills theory

3.1 Introduction

One of the possible scenarios for the genesis of the universe suggests a Big-Bang, which created a seething soup of quarks and gluons, the quark-gluon plasma, just microseconds thereafter. As the universe expanded and energy density and temperature decreased, the soup cooled down and confined into nucleons, which in turn formed the nuclei only a few minutes later. To check whether this is true or not, one can try to free the quarks and gluons from their hadron habitat and in this way to recreate the early stage of the universe.

There are several strong indications that this quark-gluon plasma has been seen just recently in heavy ion beam experiments at CERN. By colliding, for example, nucleon lead beams on a solid lead target, one generates 'Little Bangs', small pockets of hot and dense nuclear matter, presumably forming to primordial quark-gluon plasma. One of the observed signature for the quark-gluon plasma is the sudden drop in the production of J/ψ particles. This is due to the fact that the charge of the constituting charm-quarks are Debye-screened by the surrounding gluons and quarks and the binding into the J/ψ is strongly suppressed. Another sign, suggesting that the quark-gluon plasma has been observed, is the excess of light weakly interacting particles like electron-positron pairs. Yet another indication is the increased production of strange particles. Theoretical considerations predict the deconfining transition temperature of QCD, where the quarks cease to stick together in hadrons, to be around 180 MeV, roughly what has been observed by the CERN experiments.

In pure Yang-Mills theory the gluon plasma is expected to form at temperatures above 270 MeV. This small number is rather surprising in view of the fact that the lowest gluonic excitations are high (around 1.6 GeV), however, it is for example predicted by non-perturbative calculations on the lattice. We can therefore use the critical temperature T_c of the deconfining phase transition to

determine the physical scale of the lattice computations performed in this work, and, in addition to its intrinsic importance as a fundamental non-perturbative prediction, it also provides an excellent quantity to test the accuracy of the improvement scheme and to study lattice artifacts.

The chapter is organized as follows. We will first spend some effort on how finite temperature is introduced in lattice gauge theory in a formal and clean way¹. We show that the Polyakov loop correlator figures as an order parameter for the phase transition and discuss the phase structure of the theory. Then we will explain the determination of the critical couplings of the parametrized FP action including details about the simulations, the analysis and the error estimation. For each N_τ we perform simulations on several lattices for a finite size scaling study. The critical temperatures determined here will be subject to scaling tests in chapter 4. Technical details on the Ferrenberg-Swendsen reweighting, which is used in the course of calculating the critical couplings, are relegated to appendix C, where the method is illustrated by means of the two-dimensional Ising and 10-state Potts model.

3.2 Finite temperature in lattice gauge theory

The Euclidean lattice action for $SU(N)$ Yang-Mills theories is given by

$$S = -\beta \sum_{\text{pl}} \text{ReTr} (U_{\text{pl}}), \quad (3.1)$$

where U_{pl} is the plaquette product of the gauge links:

$$U_{\text{pl}} = U_\mu(x) U_\nu(x + \hat{\mu}) U_\mu^\dagger(x + \hat{\mu} + \hat{\nu}) U_\nu^\dagger(x), \quad (3.2)$$

and the sum in eq. (3.1) is over all plaquettes on the lattice.

The action (3.1) is invariant under local gauge transformations

$$U_\mu(x) \rightarrow g(x) U_\mu(x) g^{-1}(x + \hat{\mu}). \quad (3.3)$$

To discuss the physical meaning of the gauge invariance it is convenient to consider a partial gauge fixing where

$$U_4(x) = 1. \quad (3.4)$$

The remaining degrees of freedom are then the links in spatial directions $U_k(\vec{x}, t)$, $k = 1, 2, 3$. Time independent gauge transformations $g(\vec{x})$ are still allowed by the condition (3.4). In this gauge one can define the transfer matrix

$$\mathcal{T}(U', U) = \exp \left\{ \beta \sum_{\vec{x}, k} \text{ReTr} \left(U'_k(\vec{x}) U_k^\dagger(\vec{x}) \right) + \frac{1}{2} \beta \sum_{\text{pl}} U_{\text{pl}} + \frac{1}{2} \beta \sum_{\text{pl}} U'_{\text{pl}} \right\}. \quad (3.5)$$

¹This section is based on notes which originated in several discussions on finite temperature gauge theory at the Institute for Theoretical Physics in Bern. I am grateful to Ferenc Niedermayer for leaving me these notes.

The symbols U, U' denote here the sets of links on two neighboring time slices, t and $t + 1$, respectively. The summation is over spatial plaquettes in the corresponding hyperplanes. The physical meaning of the transfer matrix is that it describes the evolution of the system in Euclidean time; it can be thought as $\exp(-a\hat{H})$ where \hat{H} is the Hamiltonian of the system. To see the analogy with a path integral in quantum mechanics, note that the first term in the exponent is analogous to the kinetic term $-\frac{1}{2c}(x-y)^2$ while the others to $-\frac{1}{2}\epsilon(V(x)+V(y))$. In our case they represent the electric and the magnetic energies.

The state of the system is given by a wave function depending on the gauge links $U = \{U_k(\vec{x})\}$ and the evolution by one time step is

$$\Psi(U) \rightarrow \Psi'(U') = \int dU \mathcal{T}(U', U) \Psi(U). \quad (3.6)$$

The transfer matrix is invariant under local gauge transformations,

$$\mathcal{T}(U', U) = \mathcal{T}({}^g U', {}^g U), \quad (3.7)$$

where $g = \{g(\vec{x})\}$ and

$${}^g U_k(\vec{x}) = g(\vec{x}) U_k(\vec{x}) g^{-1}(\vec{x} + \hat{k}). \quad (3.8)$$

Define the operator $G(g)$ which performs a gauge transformation as

$$(G(g)\Psi)(U) = \Psi({}^{g^{-1}}U). \quad (3.9)$$

The reason for having g^{-1} on the rhs. is that $G(g)$ satisfies then the relation

$$G(h)G(g) = G(hg). \quad (3.10)$$

Relation (3.7) means that the transfer matrix commutes with the operators of the gauge transformations. One has a set of independent gauge transformations, each acting only at a given site \vec{x} ,

$$G(g) = \prod_{\vec{x}} G(g(\vec{x})), \quad (3.11)$$

and

$$G(g(\vec{x}))\mathcal{T} = \mathcal{T}G(g(\vec{x})) \quad \text{for any } \vec{x}. \quad (3.12)$$

As a consequence, the Hilbert space of states falls into different subspaces. The states of a given subspace are characterized by some irreducible representation of $SU(N)$ (e.g. 1, 3, $\bar{3}$, 8, etc. for $SU(3)$), one for each site \vec{x} . We shall say that at a site where the wave function of a given subspace transforms non-trivially there is an external charge. Since acting by the transfer matrix on such a state does not change its transformation properties with respect to the gauge transformations, these charges are static – the gauge dynamics does not influence them (it does not even rotate them in colour space).

The simplest and most important subspace is that of the gauge invariant functions,

$$\Psi^{(0)}({}^g U) = \Psi^{(0)}(U), \quad (3.13)$$

that is

$$G(g(\vec{x}))\Psi^{(0)} = \Psi^{(0)}, \quad \text{for any } \vec{x}. \quad (3.14)$$

This is the sector with no external charges.

Define the projector \mathcal{P}_0 defined by

$$\mathcal{P}_0 = \int dg G(g), \quad (3.15)$$

or equivalently

$$(\mathcal{P}_0 \Psi)(U) = \int dg \Psi(g^{-1}U) = \int dg \Psi(gU), \quad (3.16)$$

where $dg = \prod_{\vec{x}} dg(\vec{x})$. It projects an arbitrary function $\Psi(U)$ onto the gauge invariant subspace.

Consider now the partition function $Z^{(0)}$ of the system with no external charges, at some finite temperature. This is given by the trace of \mathcal{T}^{N_τ} taken in the subspace of gauge invariant functions. (Here N_τ is the number of time slices to which the inverse temperature is divided.) Instead of taking the trace in this subspace one can calculate the trace of $\mathcal{T}^{N_\tau} \mathcal{P}_0$ in the whole Hilbert space:

$$Z^{(0)} = \text{Tr}^{(0)}(\mathcal{T}^{N_\tau}) = \text{Tr}(\mathcal{T}^{N_\tau} \mathcal{P}_0) = \sum_{\{U\}} \langle U | \mathcal{T}^{N_\tau} \mathcal{P}_0 | U \rangle, \quad (3.17)$$

where $U = \{U_k(\vec{x})\}$ is an arbitrary gauge configuration. The state $|U\rangle$ is described by a sharp wave function $\Psi(U') = \delta_{U'U}$, analogously to the states $|x\rangle$ in quantum mechanics. Using eq. (3.15) we have

$$Z^{(0)} = \sum_{\{U_k(\vec{x})\}} \int \prod_{\vec{x}} dg(\vec{x}) \langle U | \mathcal{T}^{N_t} | gU \rangle. \quad (3.18)$$

In other words, the gauge configuration on the time slice $t = 0$ coincides with that on the time slice $t = N_t$ only up to an arbitrary gauge transformation $g = \{g(\vec{x})\}$. This is the consequence of projecting onto the subspace with no external charges. Without the integration over $g(\vec{x})$ one would obtain an expression which is the sum of partition functions for all possible choices of the external charges. However, this would not be a useful quantity.

Due to the fact that $\mathcal{P}_0 \mathcal{T} = \mathcal{T} \mathcal{P}_0$ and $\mathcal{P}_0^2 = \mathcal{P}_0$, one can rewrite $Z^{(0)}$ by introducing an extra (superficial) \mathcal{P}_0 between any two time slices,

$$Z^{(0)} = \text{Tr}(\mathcal{T} \mathcal{P}_0 \mathcal{T} \mathcal{P}_0 \dots \mathcal{T} \mathcal{P}_0) = \int dU_0 \dots dU_{N_t-1} dg_0 \dots dg_{N_t-1} \mathcal{T}(U_0, {}^{g_0}U_1) \mathcal{T}(U_1, {}^{g_1}U_2) \dots \mathcal{T}(U_{N_t-1}, {}^{g_{N_t-1}}U_0). \quad (3.19)$$

Here U_t for $t = 0, \dots, N_t - 1$ denote the set of spatial links $\{U_k(\vec{x}, t), k = 1, 2, 3\}$. Observe that $g_t = \{g(\vec{x}, t)\}$ play the role of the temporal gauge links $U_4(\vec{x}, t)$ between the time slices t and $t + 1$ since $\text{ReTr}(U_k(\vec{x}, t) U_k^\dagger(\vec{x}, t + 1))$ goes into

$$\text{ReTr}(U_k(\vec{x}, t) ({}^g U_k(\vec{x}, t + 1))^\dagger) = \text{ReTr}(U_k(\vec{x}, t) g(\vec{x} + \hat{k}, t) U_k^\dagger(\vec{x}, t + 1) g^{-1}(\vec{x}, t)). \quad (3.20)$$

This is equivalent to the contribution to the action (3.1) from a plaquette in the $k4$ plane if we set $g(\vec{x}, t) = U_4(\vec{x}, t)$.

Consequently, the partition function in the sector with no external charges is given by the original Wilson action via $\sum_U \exp(-S(U))$ (without any gauge fixing) and with periodic b.c. on the gauge links in the time direction, $U_k(\vec{x}, N_t) = U_k(\vec{x}, 0)$. The projection onto the gauge invariant subspace is achieved by the integration over the time components $U_4(\vec{x}, t)$.

It is important to know how the system responds when external charges are introduced at a given temperature. Introducing a static $Q\bar{Q}$ pair at some points \vec{x} and \vec{y} means that we restrict the sum defining the partition function to the subspace of functions which at every point $\vec{z} \neq \vec{x}, \vec{y}$ transform as a singlet, while at points \vec{x} and \vec{y} as $\mathbf{3}, \bar{\mathbf{3}}$. The partition function in this sector gives the free energy of the $Q\bar{Q}$ pair at the relative distance $\vec{r} = \vec{x} - \vec{y}$,

$$\frac{Z^{Q\bar{Q}}}{Z^{(0)}} = e^{-F_{Q\bar{Q}}(\vec{r}, T)/T}. \quad (3.21)$$

The behaviour of the free energy $F_{Q\bar{Q}}(\vec{r}, T)$ for large separations \vec{r} distinguishes between confinement and deconfinement at the given temperature T . For $T < T_c$, in the confining phase, for $r \rightarrow \infty$ one has $F_{Q\bar{Q}} \rightarrow \infty$, while for $T > T_c$, in the deconfined phase, $F_{Q\bar{Q}} \rightarrow \text{const.}$ For the practical definition of this ratio we need the projection operator onto the fundamental representation at a given point.

Obviously, a gauge invariant product of links along a closed loop in a given time slice (e.g. $\text{Tr}(U_{\text{pl}})$ of eq. (3.2) as the simplest case) represents an admissible wave function in the sector with no external charges. It can be shown that it represents a closed loop of (colour)electric flux. An open string built by links is expected to describe a state where at the two ends two external charges are sitting. To see this consider a product of gauge links starting from site \vec{x} and ending at \vec{y} ,

$$\Psi_{ab}(U) = \left(U_k(\vec{x}) U_l(\vec{x} + \hat{k}) \dots \right)_{ab}. \quad (3.22)$$

The transformation property of this wave function is

$$(G(h)) \Psi_{ab}(U) = \Psi_{ab}(h^{-1}U) = h_{a'a'}^{-1}(\vec{x}) \Psi_{a'b'}(U) h(\vec{y})_{b'b}. \quad (3.23)$$

Define the operators

$$\mathcal{P}_{ab}(\vec{x}) = \int dg(\vec{x}) g_{ab}(\vec{x}) G(g(\vec{x})). \quad (3.24)$$

Using the relation

$$\int dg g_{ab} g_{cd}^{-1} = \frac{1}{N} \delta_{ad} \delta_{bc} \quad (3.25)$$

and eq. (3.10) one obtains

$$\mathcal{P}_{ab}(\vec{x}) \mathcal{P}_{cd}(\vec{x}) = \frac{1}{N} \delta_{bc} \mathcal{P}_{ad}(\vec{x}). \quad (3.26)$$

The relation

$$G(h(\vec{x})) \mathcal{P}_{ab}(\vec{x}) = h_{ac}^{-1}(\vec{x}) \mathcal{P}_{cb}(\vec{x}) \quad (3.27)$$

shows that $\mathcal{P}_{ab}(\vec{x})$ acting on any function picks up the part which transforms at point \vec{x} according to the fundamental representation, with index a (for any given b). Moreover, acting on the wave function in eq. (3.22) one has

$$\mathcal{P}_{cd}(\vec{x}) \Psi_{ab} = \frac{1}{N} \delta_{ad} \Psi_{cb}, \quad (3.28)$$

that is $\mathcal{P}_{cd}(\vec{x})$ picks up only those functions whose index a at point \vec{x} coincides with its second index d , and transforms it into a function with index c , its first index. Obviously, its trace (apart from the factor $1/N$) is the desired projector

$$\mathcal{P}^Q(\vec{x}) = N\mathcal{P}_{cc}(\vec{x}). \quad (3.29)$$

It satisfies the relations

$$\mathcal{P}^Q(\vec{x})\mathcal{P}^Q(\vec{x}) = \mathcal{P}^Q(\vec{x}) \quad (3.30)$$

and

$$\mathcal{P}^Q(\vec{x})\Psi_{ab} = \Psi_{ab}. \quad (3.31)$$

For completeness, define an operator which projects onto the appropriate subspace at point \vec{y} . For this let

$$\mathcal{P}_{ab}^*(\vec{y}) = \int dg(\vec{y})g^{-1}(\vec{y})_{ab}G(g(\vec{y})). \quad (3.32)$$

It satisfies similar relations, in particular

$$\mathcal{P}_{cd}^*(\vec{y})\Psi_{ab} = \frac{1}{N}\delta_{bc}\Psi_{ad}. \quad (3.33)$$

The corresponding projector at point \vec{y} is then

$$\mathcal{P}^{\bar{Q}}(\vec{y}) = N\mathcal{P}_{cc}^*(\vec{y}). \quad (3.34)$$

The projection to the desired subspace where the only external charges are at sites \vec{x} and \vec{y} is achieved by multiplying the appropriate projectors for each site,

$$\mathcal{P}^{Q\bar{Q}} = \mathcal{P}^Q(\vec{x})\mathcal{P}^{\bar{Q}}(\vec{y}) \prod_{\vec{z} \neq \vec{x}, \vec{y}} \mathcal{P}_0(\vec{z}). \quad (3.35)$$

The partition function in this subspace is then given by

$$Z^{Q\bar{Q}} = \frac{1}{N^2} \text{Tr} \left(\mathcal{T}^{N_t} \mathcal{P}^{Q\bar{Q}} \right) = \frac{1}{N^2} \sum_{\{U\}} \langle U | \mathcal{T}^{N_t} \mathcal{P}^{Q\bar{Q}} | U \rangle. \quad (3.36)$$

The $1/N^2$ factor (which is anyhow an unimportant constant factor) is introduced here because the trace is in fact a sum over $N \times N$ different possible orientations of the external fundamental source in the colour space. We identify again the integration variables $g(\vec{z})$ in the projectors with the links $U_4(\vec{z}, t_0)$ where $t_0 = N_t - 1$ (or any fixed value). The partition function $Z^{Q\bar{Q}}$ is given by integration over the fields $U_k(\vec{z}, t)$, $U_4(\vec{z}, t_0)$, keeping $U_4(\vec{z}, t) = 1$ for $t \neq t_0$ with the integrand $\text{tr}(U_4(\vec{x}, t_0))\text{tr}(U_4^\dagger(\vec{y}, t_0))\exp(-S(U))$. Introducing an arbitrary time dependent gauge transformation on this configuration one restores all time like links $U_4(\vec{z}, t)$. By this procedure the original $\text{Tr}U_4(\vec{x}, t_0)$ term goes over to the Polyakov loop at \vec{x} , that is, the ratio in eq. (3.21) is obtained by the correlation function of Polyakov loops $L(\vec{x})$,

$$\frac{Z^{Q\bar{Q}}}{Z^{(0)}} = \langle L(\vec{x})L^*(\vec{y}) \rangle, \quad (3.37)$$

where

$$L(\vec{x}) = \text{tr} (U_4(\vec{x}, 0)U_4(\vec{x}, 1) \dots U_4(\vec{x}, N_t - 1)). \quad (3.38)$$

It is interesting to observe that using $\mathcal{P}^{Q\bar{Q}}\mathcal{P}^{Q\bar{Q}} = \mathcal{P}^{Q\bar{Q}}$ and $\mathcal{T}\mathcal{P}^{Q\bar{Q}} = \mathcal{P}^{Q\bar{Q}}\mathcal{T}$ one can introduce $U_4(\vec{z}, t)$ on all time slices in an alternative way. In this way one obtains the product of traces,

$$\text{Tr} (U_4(\vec{x}, 0)) \text{Tr} (U_4(\vec{x}, 1)) \dots \text{Tr} (U_4(\vec{x}, N_t - 1)). \quad (3.39)$$

It is easy to see that after integrating over all gauge equivalent configurations this reproduces the previous answer. Indeed, according to eq. (3.25), one has

$$N \int dg \text{Tr} (Vg^{-1}) \text{Tr} (gW) = \text{Tr} (VW). \quad (3.40)$$

This form is, however, not convenient for the use in simulations since it is noisier than the Polyakov loop, eq. (3.38).

3.3 The phase structure of lattice gauge theory

In this section we will briefly expose the main features of the deconfining phase transition in pure Yang-Mills theory at finite temperature. Based on the presentation in the previous section, we will first dwell on the correlation of the Polyakov loop as the order parameter of the transition, then recall the phase structure of the theory and at the end discuss the connection with the spontaneous breakdown of the center symmetry of lattice gauge theory.

3.3.1 Polyakov loop correlator as the order parameter of the phase transition

That pure Yang-Mills theory undergoes a phase transition at some temperature T_c was expected already some time ago [22, 23] and the first non-perturbative lattice determinations of the transition followed shortly after [24]. As is already clear from the previous section, the phase transition is accompanied by a radical change in the behaviour of the correlator

$$\langle L(\vec{x})L^\dagger(0) \rangle, \quad (3.41)$$

where $L(\vec{x})$ is the Polyakov loop or Wilson line

$$L(\vec{x}) = \text{Tr} \text{P exp} \left\{ ig \oint_0^\beta dt A_4(\vec{x}, t) \right\}, \quad \beta = \frac{1}{T}, \quad (3.42)$$

and the gluon fields satisfy periodic boundary conditions. The simplest lattice realization of this object may be written as

$$L(\vec{x}) = \text{Tr} \prod_{t=0}^{N_\tau-1} U_4(\vec{x}, t). \quad (3.43)$$

Physically, $L(\vec{x})$ can be interpreted as the world line of a static quark (or a color source) representing the self-energy of an infinitely heavy quark as explained

in the previous section. One can conclude that the excess free energy of a single static quark relative to the absence of the quark is given by the thermal expectation value of the Polyakov loop,

$$e^{-(F_Q(T)-F_0(T))} = \langle L(\vec{x}) \rangle = \langle L \rangle. \quad (3.44)$$

In the last step we have used translational invariance of the vacuum which allows one to consider the spatially averaged operator only,

$$L \equiv \frac{1}{N_\sigma^3} \sum_{\vec{x}} \text{Tr} \prod_{t=0}^{N_\tau-1} U_4(\vec{x}, t). \quad (3.45)$$

Analogously the correlator of a Polyakov loop and its adjoint one having opposite orientation, contains information about the free energy of a static quark-antiquark pair,

$$\langle L(\vec{x})L^\dagger(0) \rangle = \exp\{-(F_{Q\bar{Q}}(\vec{x}, T) - F_0(T))\}. \quad (3.46)$$

Assuming cluster decomposition at large distances one has

$$\langle L(\vec{x})L^\dagger(0) \rangle \xrightarrow{|\vec{x}| \rightarrow \infty} |\langle L \rangle|^2. \quad (3.47)$$

In the pure gauge theory a single colour-triplet charge can not be screened by dynamical sea quarks in the confined phase and its free energy F_Q becomes infinite causing a vanishing expectation value of $L(\vec{x})$. At large distances the correlation function decays exponentially,

$$\langle L(\vec{x})L^\dagger(0) \rangle \sim \exp\{-\sigma(T)|\vec{x}|/T\}, \quad (3.48)$$

hence the free energy increases linearly with the string tension $\sigma(T)$ for large separations signaling confinement.

On the other hand, in the deconfined phase the free energy of a static quark-antiquark pair remains finite even at large separations and the Polyakov loop may acquire a non-vanishing expectation value $\langle L(\vec{x}) \rangle \neq 0$. Thence we interpret the Polyakov loop as an order parameter for the deconfining phase transition in the pure gauge theory².

Below the critical temperature we have a confining vacuum with thermal fluctuations exciting a dilute gas of glueballs, while the high temperature region is characterized as a gluon plasma phase with freely moving but still interacting gluons. In this phase static colour charges would be Debye-screened but not confined. For a deeper understanding in terms of forming flux tubes see for instance [27, 28].

To complete the physical picture let us shortly touch the full theory including dynamical quarks. In full QCD the low temperature phase corresponds to the usual hadronic QCD vacuum producing a rarefied pion gas, which can adequately be described by chiral perturbation theory. The high temperature phase describes a quark-gluon plasma created for example in high energy nuclei

²This is not quite true: strictly speaking only the correlator (3.41) has a physical meaning and may serve as an order parameter. The phase of the expectation value of $\langle L \rangle$ is not a physically measurable quantity [25]. Nevertheless, we will adopt here the traditional viewpoint [26].

or heavy ion collisions and presumably realized at an early stage of the universe. For small quark masses the order parameter associated with the phase transition is the quark condensate $\langle \bar{q}q \rangle$ and the transition is related to the restoration of chiral symmetry.

For a nice and thorough review on all these topics we refer to [29].

3.3.2 Center symmetry

Usually phase transitions are associated with the spontaneous breakdown of a global symmetry of the system. This is also the case for lattice gauge theory at finite temperature.

In addition to local periodic gauge symmetry associated with the colour gauge group $SU(N_c)$, lattice gauge theory also enjoys invariance under a global unitary transformation of all temporal link matrices $U_4(\vec{x}, t)$ of a given temporal hyperplane with fixed t by an element z of the center³ $\mathcal{Z}(N_c)$ of $SU(N_c)$,

$$U_4(\vec{x}, t) \rightarrow zU_4(\vec{x}, t) \quad \forall \vec{x} \text{ with } t \text{ fixed.} \quad (3.49)$$

The invariance under this global $\mathcal{Z}(N_c)$ symmetry is evident from the explicit form of Wilson's lattice action,

$$\begin{aligned} S_{\text{Wilson}} = & \\ & \beta \sum_{1 \leq i \leq j \leq 3} \left(1 - \frac{1}{N_c} \text{Re Tr } U_i(x) U_j(x + \hat{i}) U_i^\dagger(x + \hat{j}) U_j^\dagger(x) \right) \\ & + \beta \sum_{1 \leq i \leq 3} \left(1 - \frac{1}{N_c} \text{Re Tr } U_i(x) U_4(x + \hat{i}) U_i^\dagger(x + \hat{4}) U_4^\dagger(x) \right), \quad (3.50) \end{aligned}$$

but of course also applies for the FP action parametrized using smeared links. The argument is simple and applies to any local action. This can easily be seen by considering that any local closed loop must pass a given spatial hypersurface between t and $t + a$ an even number of times, equally in both possible directions, and thereby cancelling the extra factors. Although the action and local observables are invariant under these center transformations, the Polyakov loop (3.43) is not,

$$L(\vec{x}) \rightarrow zL(\vec{x}). \quad (3.51)$$

As a consequence of this fact, lattice configurations related by the center symmetry will occur with equal probability if the ground state of the theory respects the center symmetry. Thus the same number of configurations will contribute to the expectation value of the Polyakov loop the values L with phases $e^{2\pi ik/N_c}$, $k = 0, \dots, N_c - 1$, finally causing the expectation value to vanish due to $\sum_k \exp(2\pi ik/N_c) = 0$. As we have seen in the previous section this corresponds to the low temperature, confining phase of the pure gauge theory with $\langle L \rangle = 0$. Per contra, in the high temperature, deconfining phase with $\langle L \rangle \neq 0$ the center symmetry is necessarily broken⁴.

³The center of a group \mathcal{G} consists of the subgroup of elements z commuting with all group elements, i.e. $zgz^{-1} = g$ for all $g \in \mathcal{G}$. In the case of $SU(N_c)$ being the gauge group, the center $\mathcal{Z}(N_c)$ contains the N_c matrices $\exp\{2\pi ik/N_c\}$, $k = 0, \dots, N_c - 1$.

⁴It goes without saying that for finite volumes the ground state will tunnel between the N_c degenerate vacua and hence force $\langle L \rangle$ still to be zero. This can be regarded as a consequence

It can be argued on grounds of the $\mathcal{Z}(N_c)$ symmetry that the critical behaviour of the $SU(N_c)$ pure gauge theory is that of a three dimensional $\mathcal{Z}(N_c)$ symmetric spin model with ferromagnetic short range interactions [30, 31, 32, 33, 34]⁵. This expectation has been confirmed in [37].

As for illustration figure 3.1 shows the restoration of the center symmetry as the inverse temperature β of the system is decreased below the critical coupling β_c . Note the tunneling of the system between the degenerate vacua in the deconfined phase. The phase changes and the coexistence of the two phases are illustrated in figure 3.2 where we show a typical Monte Carlo time history on a 4×12^3 lattice near the critical coupling of the FP action. At the critical coupling the system flips between the ordered and the disordered phase giving rise to the clearly visible double peak structure in the probability distributions of the energy and the order parameter, typical for a first order phase transition. Figure 3.3 shows the probability distributions of the Polyakov loop order parameter, $|L|$, and the energy at the critical coupling of the FP action on a 2×10^3 lattice.

Despite this impressive evidence for a first order phase transition one has to be careful: the characteristic first order phase transition discontinuities in physical quantities like the Polyakov loop susceptibility χ_L or the order parameter are washed away on finite lattices. Nevertheless one may invoke a finite size scaling analysis of thermodynamic quantities in order to determine the order of the phase transition. Such an analysis is clearly beyond the scope of the present work, however, it has been done for example in [38, 39, 26, 40, 37] with clear evidence for the first order nature of the $SU(3)$ deconfinement phase transition.

3.4 Determination of the temporal scale

Consider the statistical partition function of a quantum mechanical system at temperature T ,

$$\mathcal{Z}(T) = \text{Tr} e^{-H/T}. \quad (3.52)$$

Here, H is the Hamiltonian of the statistical system and Tr denotes the thermal trace, i.e. the sum over all states $\sum_n \langle n | e^{-H/T} | n \rangle$. Using the transfer matrix approach as outlined in section 3.2 one can obtain a path integral representation for the partition function. For pure Yang-Mills theory this amounts to

$$\mathcal{Z} = \mathcal{N} \int \mathcal{D}A e^{-S^{(\beta)}[A]}, \quad (3.53)$$

where A denotes the gauge fields and \mathcal{N} is a normalization constant. The path integral is carried out over all field configurations satisfying the periodic boundary conditions $A_\mu(\vec{x}, 0) = A_\mu(\vec{x}, \beta)$ and $S^{(\beta)}[A]$ is the finite temperature

of Gauss' law which forbids a net charge in a finite volume with periodic boundary conditions. Of course, these changes of phases extending over the entire volume can not be accomplished in an infinite volume, simply reflecting the fact that in this limit a single charge is no longer inconsistent with Gauss' law. It is therefore convenient, for any practical purposes, to replace L by $|L|$.

⁵In the case of $SU(2)$ one would expect the same critical behaviour as for the three dimensional Ising model, which shows a second order phase transition, and indeed excellent agreement between the critical exponents of the $SU(2)$ Yang-Mills theory and the 3- d Ising model has been found [35, 36].

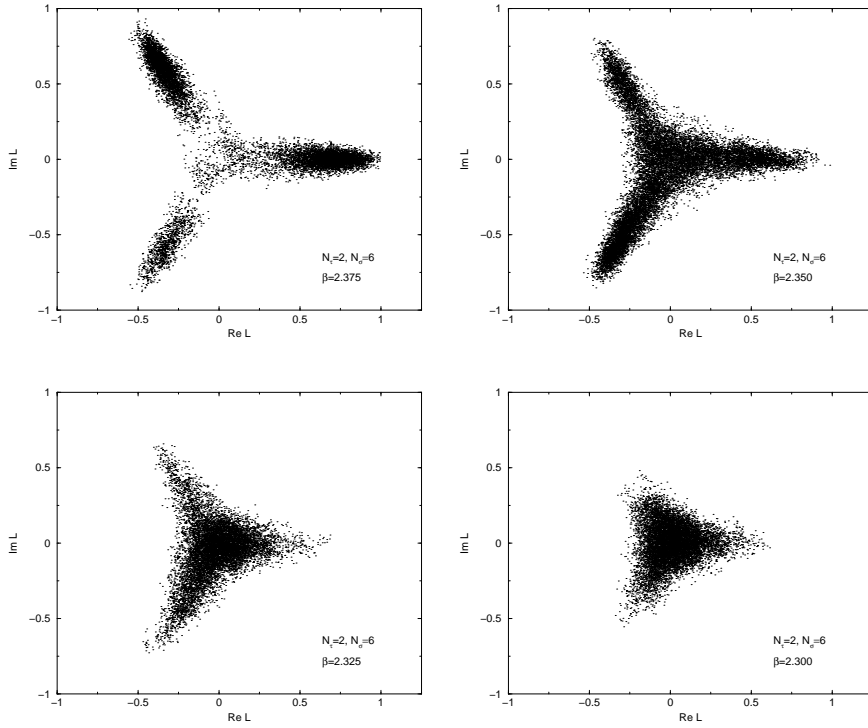


Figure 3.1: Restoration of the center symmetry as the inverse temperature β of the system is decreased below the finite volume critical coupling $\beta_c(N_t = 2) \sim 2.359$. The plots show Monte Carlo calculations of the Polyakov loop order parameter L in the complex plane on a 2×6^3 lattice. Note the tunneling of the system between the degenerate vacua in the deconfined phase and the coexistence of the phases near the critical β -value.

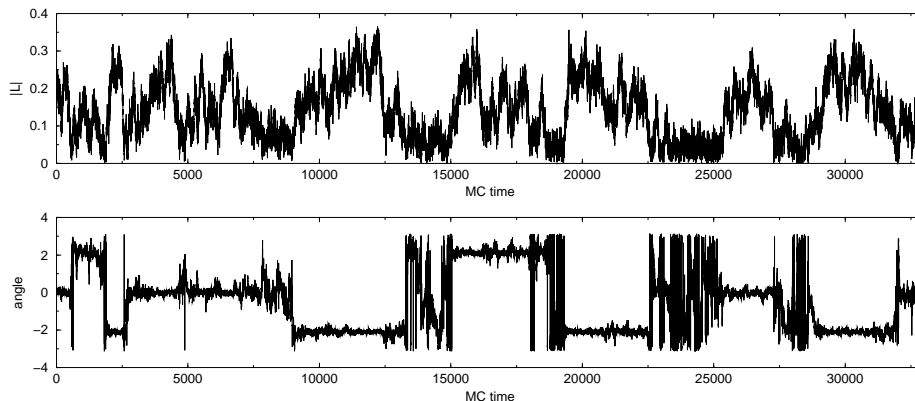


Figure 3.2: Monte Carlo time history of the modulus $|L|$ and the phase $\theta = \arg(L)$ of the Polyakov loop order parameter $L = |L|e^{i\theta}$ on a 4×12^3 lattice at $\beta = 2.91$ near the critical value of the FP gauge action. The noisy regions in the angle plot indicate time intervals during which the system is in the symmetric phase where the angle is not well defined. The remaining time is spent in one of the three broken degenerate phases where the angle takes the values $\theta \approx 0, \pm 2\pi/3$.

action

$$S^{(\beta)}[A] = \frac{1}{2} \int_0^\beta d\tau \int_{-\infty}^{\infty} d^3x \text{Tr}(F_{\mu\nu}(\vec{x}, \tau) F_{\mu\nu}(\vec{x}, \tau)), \quad \beta = \frac{1}{T}. \quad (3.54)$$

Introducing a lattice regularization for (3.53) with lattice spacing a in coordinate space the correspondence with a classical statistical system is even more evident. Thus we conclude that the quantum field theory at finite temperature T is equivalent to a Euclidean field theory on a space-time with compactified time direction of extension $1/T$.

The lattice regularized version of (3.53) can be written down as

$$\mathcal{Z} = \mathcal{N} \int \mathcal{D}U e^{-S^{(\beta)}[U]}, \quad (3.55)$$

where the integration is over the gauge link variables U subject to periodic boundary conditions in time direction, $U(\vec{x}, 0) = U(\vec{x}, \beta)$. The action $S^{(\beta)}[U]$ is the sum of some lattice version of $F_{\mu\nu}(x)F_{\mu\nu}(x)$ over all lattice sites. In time direction the lattice extends over a finite number of lattice sites, N_τ , while in space direction the number of lattice sites, N_σ , is infinite in the thermodynamic limit. According to the analogy described above the inverse temperature $1/T$ is related to the temporal extension of the lattice by $1/T = N_\tau a$ thereby fixing the lattice spacing in physical units. Since N_τ can only take discrete values it is convenient to hold this relation fixed while varying the gauge coupling β and therefore implicitly the lattice spacing a . In this way we move the lattice system through the phase transition obtaining finally

$$\frac{1}{T_c} = N_\tau a(\beta_c). \quad (3.56)$$

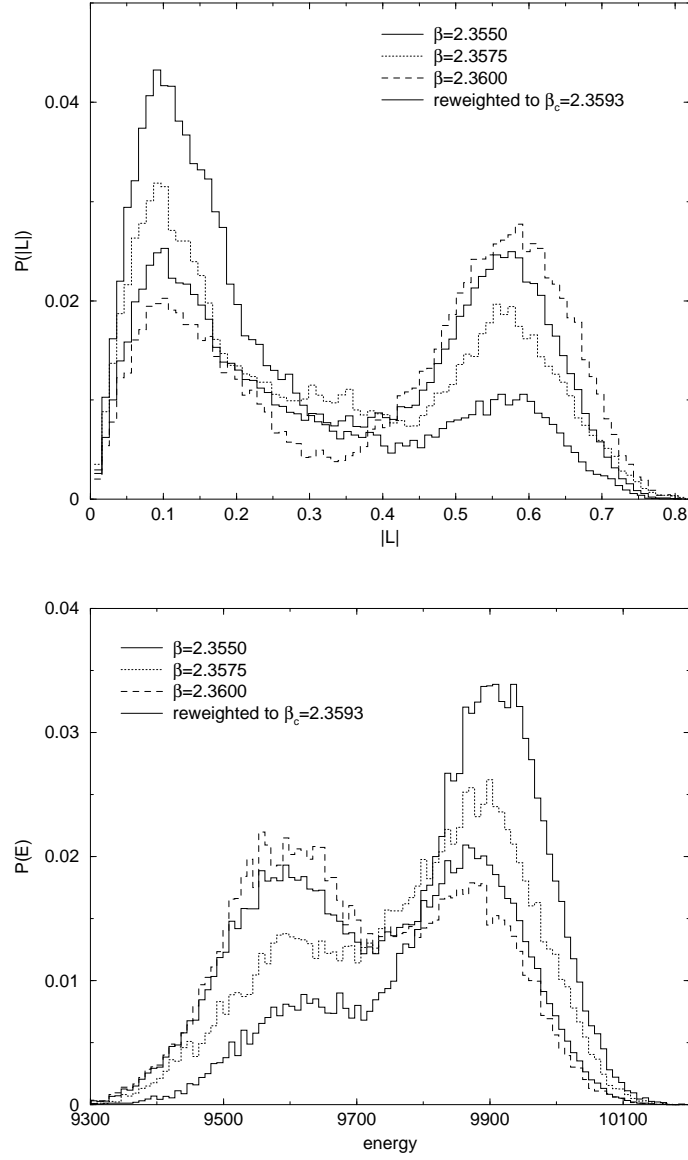


Figure 3.3: Probability distributions of the Polyakov loop order parameter, $|L|$, and the energy on a 2×10^3 lattice. The highlighted distributions show the results at the finite volume critical coupling $\beta_c(N_t = 2) = 2.3593$ obtained by reweighting results at nearby β -values.

In order to get a first impression and some feeling about the lattice spacings we are dealing with let us calculate the temporal scale a in physical units. For convenience we adopt the value from [41] for the critical temperature, $T_c \simeq 276(2)\text{MeV}$, and take it as a definition for the moment. The resulting quantities are collected in table 3.1 and based on the results obtained in section 3.5 with the FP action. The error in the scale comes entirely from the uncertainty in the

N_τ	β_c	a_τ [fm]
2	2.361(1)	0.3575(7)
3	2.680(2)	0.2383(6)
4	2.927(4)	0.1787(3)

Table 3.1: Temporal scale of the FP action at the critical couplings of $N_\tau = 2, 3$ and 4.

determination of the critical coupling and thence in the critical temperature.

3.5 Determination of the critical couplings

There are several alternative methods for determining the critical couplings. They all give the same critical couplings β_c as the spatial volume is increased to infinity. At finite volume, however, the deviation of the estimate from β_c at infinite volume depends on the method applied. One possible method employed in the early days of finite temperature simulations on the lattice is to measure the deconfinement fraction [26],

$$f_d(\beta) = \frac{3}{2}f_{20}(\beta) - \frac{1}{2}, \quad (3.57)$$

where $f_{20}(\beta)$ is the fraction of measurements at a given β -value for which the phase of the Polyakov loop, $\theta = \arg(L)$, lies within the range of $\pm 20^\circ$ around the $\mathcal{Z}(3)$ roots $e^{2\pi ik/3}$, $k = 0, 1, 2$. The critical coupling β_c is then defined as the point where $f_d(\beta)$ takes a given value. Originally [26], the value $f_d = \frac{1}{2}$ was exploited and it was shown that the results are consistent with using f_{30} instead of f_{20} . This method provides a definite value of β_c by linearly interpolating from $f_d(\beta)$ -values bracketing $\frac{1}{2}$ and also allows reasonable error estimates. Choosing a different criterion $f_d(\beta_c) = \frac{3}{4}$, as for example in [38, 41, 42], leads to different critical coupling values at finite volumes which, in any case, should coincide in the limit of infinite spatial volume. However, our findings are completely opposite: we determined the critical values with both the $f_d(\beta) = \frac{1}{2}$ and $f_d(\beta) = \frac{3}{4}$ definition on small volumes and performed the finite size scaling. The obtained infinite volume critical couplings differ from each other significantly. This is an indication that the finite scaling regime on the small lattices has not been reached for these quantities. Our observation is in complete agreement with [42] and relies on the fact that there is no rigorous finite size scaling for β_c determined from the deconfinement fraction⁶.

Since we are working on relatively small spatial volumes it is thus certainly necessary to refer to a definition of the critical coupling which relies on a quantity

⁶See also the discussion in [37] and [42].

with definite finite size scaling. Such physically better motivated quantities are for example response functions like the specific heat or the susceptibility of the finite temperature system. For instance the susceptibility of the order parameter in the pure gauge theory, the Polyakov loop susceptibility, is defined as

$$\chi_L \equiv V (\langle |L|^2 \rangle - \langle |L| \rangle^2), \quad V = N_\sigma^3, \quad (3.58)$$

and is expected to have a rigorous finite size scaling behaviour. In the thermodynamic limit, the susceptibility develops a delta-function singularity at a first order phase transition. On a finite lattice the singularity is rounded off and the quantity reaches a peak value, χ_L^{peak} , at $\beta_c(V)$. In the infinite volume limit, the singularity emerges from the scaling of the height of the peak and its width (determining the finite volume shifts $\delta\beta_c$ in the critical coupling) according to⁷

$$\chi_L^{\text{peak}} \sim V, \quad \delta\beta_c \sim \frac{1}{V}. \quad (3.59)$$

Using this definition, the determination of β_c at finite volumes is plagued by considerable uncertainties for small volumes due to the broad width of the peak of χ_L as demonstrated in figure 3.4.

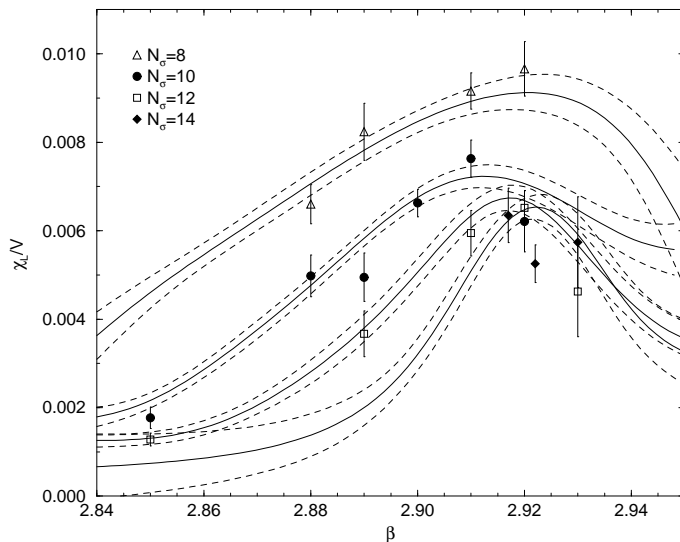


Figure 3.4: Polyakov loop susceptibility at $N_\tau = 4$ normalized by the volume, χ_L/V , as a function of β for various spatial volumes with $N_\sigma = 8, 10, 12, 14$. The solid curve represent the results of reweighting with the spectral density method and the dashed lines denote the error bars.

Nevertheless, pronounced peaks are visible for the spatial volumes with $N_\sigma/N_\tau \geq 2.5$ which we finally considered (see section 3.5.2) in the analysis. At last, the exact critical coupling has been determined by extensively using the spectral density reweighting method which enables the calculation of observables away from the values of β at which the simulations are performed.

⁷For a second order phase transition one expects $\chi_L^{\text{peak}} \sim V^{\gamma/d\nu}$ and $\delta\beta_c \sim V^{-1/d\nu}$ with γ, ν being the conventional critical exponents and d the dimension of the system.

This method has been first proposed by [43, 44] and was later emphasized by Ferrenberg and Swendsen [45, 46]. In appendix C we give a detailed description of the method and illustrate its application by means of simple models like the Ising model and the q -state Potts model in two dimensions.

The strategy as outlined above has already been successfully applied to SU(3) pure gauge theory [37, 47, 42] as well as full QCD [48].

3.5.1 Simulation details

We performed a large number of simulations on lattices with temporal extension $N_\tau = 2, 3$ and 4 at three to six different β -values near the estimated critical β_c . Various spatial extensions $N_\sigma/N_\tau = 2.5 \dots 5$ were exploited with the intention of examining the finite size scaling of the critical couplings. Configurations were generated using a Metropolis step followed by an overrelaxation step acting on SU(2) subgroups.

At each β -value we first let the system run for thermalization. Usually we spend 500 to 1000 sweeps depending on whether the starting configuration was randomly generated or a configuration thermalized at a nearby β -value. For some remarks related to incomplete thermalization we refer to section 3.5.3 about error estimation.

In the equilibrated system we measured the real and imaginary parts of all Polyakov loop operators averaged over the whole lattice as well as the energy of the configuration after each sweep. Both the action values and the modulus of the Polyakov loop operator were stored for later use in the reweighting procedure.

The simulation details and run parameters are collected in tables 3.2, 3.3 and 3.4, where we list the lattice size together with the β -values and the number of sweeps. The number of sweeps as a measure of the collected statistics is inadequate for phase transitions (see the discussion in section 3.5.3), because it is rather biased by the persistence time and the critical slowing down. The persistence time of one phase is defined as the number of sweeps divided by the observed number of flip-flops between the two phases [37]. This quantity is sensitive only for β -values nearest to the critical coupling β_c and has to be taken with a large grain of salt: for the small volumes which we exploited the fluctuations within one phase can be as large as the separation between the two phases, and the transition time from one state to the other is sometimes as large as the persistence time itself.

In the last two columns we list the estimated persistence time τ_p and the integrated autocorrelation time τ_{int} of the Polyakov loop operator. Note that the integrated autocorrelation time grows significantly near the phase transition⁸ and can therefore serve as a first crude estimate of the critical couplings.

3.5.2 Analysis details

For the determination of the critical couplings in the thermodynamic limit we resort to a two step procedure. First, we determine the critical coupling with its

⁸In fact the integrated autocorrelation time is expected to diverge near second order critical points according to the dynamical scaling law $\tau_{\text{int}} \sim \xi^z$ where ξ is the correlation length and z is the dynamical critical exponent. At a first order transition the correlation length remains finite, however, it may appear divergent due to the presence of tunnelings.

lattice size	β	sweeps	τ_p	τ_{int}
2×10^3	2.3550	30000		260.5
	2.3575	30000	4300	283.0
	2.3560	30000	4600	280.0
2×8^3	2.3300	14240		29.6
	2.3500	10144		93.5
	2.3550	5120		127.9
	2.3575	12288	1400	202.4
	2.3700	10144		114.7
2×6^3	2.3250	8096		35.6
	2.3500	14144	650	105.4
	2.3600	10000	700	96.8
	2.3750	10144		39.2

Table 3.2: Run parameters of the finite temperature simulations at $N_\tau = 2$.

lattice size	β	sweeps	τ_p	τ_{int}
3×12^3	2.675	25000		114.8
	2.680	45000	3200	188.9
	2.685	24000		96.3
	2.690	20000		53.4
3×10^3	2.670	18000		67.0
	2.680	42000	2300	89.2
	2.685	48000	2400	104.4
	2.690	27000		85.3
3×8^3	2.650	10096		43.1
	2.660	10000		48.3
	2.670	26000		41.2
	2.680	30000	1400	64.3
	2.690	19000		53.5
	2.710	10000		35.5

Table 3.3: Run parameters of the finite temperature simulations at $N_\tau = 3$.

lattice size	β	sweeps	τ_p	τ_{int}
4×14^3	2.917	50405	4300	62.8
	2.922	51812	4700	67.1
	2.930	44607		64.4
4×12^3	2.850	15000		19.7
	2.890	15000		30.4
	2.910	33000		34.9
	2.920	33000	3700	66.4
	2.930	15000		38.2
4×10^3	2.850	10000		22.4
	2.880	16000		37.9
	2.890	21124		18.9
	2.900	35000		34.2
	2.910	35000	2100	36.0
	2.920	20000		39.9

Table 3.4: Run parameters of finite temperature simulations at $N_\tau = 4$.

error on every lattice size by means of locating the peak of the Polyakov loop susceptibility as described in section 3.5 and in appendix C. In a second step we extrapolate the critical couplings for each value of N_τ to infinite volume using the finite size scaling law for a first order phase transition⁹,

$$\beta_c(N_\tau, N_\sigma) = \beta_c(N_\tau, \infty) - h \left(\frac{N_\tau}{N_\sigma} \right)^3, \quad (3.60)$$

where h is considered to be an universal quantity independent of N_τ [49]. In fact, one often assumes the value $h \geq 0.1$ determined on small N_τ lattices also for the extrapolation at larger N_τ [47, 41, 49]. In our simulations of the FP action the universality of the finite size scaling law seems to be applicable to $N_\tau = 2$ and $N_\tau = 4$ while the behaviour at $N_\tau = 3$ is not clear to us.

In figure 3.5 we show the pronounced peaks of the Polyakov loop susceptibility for some of the simulated lattice sizes. The figures from the other volumes look very similar. The solid lines are the interpolation obtained from the Ferrenberg-Swendsen reweighting and the dashed lines represent the bootstrap error band estimation. All the interpolations are based on the collective data of the simulations listed in tables 3.2-3.4 for a given lattice size, although the runs at β -values far away from the critical coupling do not influence the final result¹⁰. By virtue of the reweighted curve we determine the critical coupling as the location of the peak of the Polyakov loop susceptibility. The numerical results of this analysis are listed in table 3.5, where we display the finite size critical couplings together with the corresponding infinite volume limit and the scaling constant h . The finite size scaling behaviour for each N_τ is shown in figure 3.6.

⁹See remarks and discussion in the introduction of section 3.5.

¹⁰This is due to the fact that the distribution of configurations at a β -value far away from the critical coupling has a vanishing overlap with the distribution obtained at the critical coupling β_c .

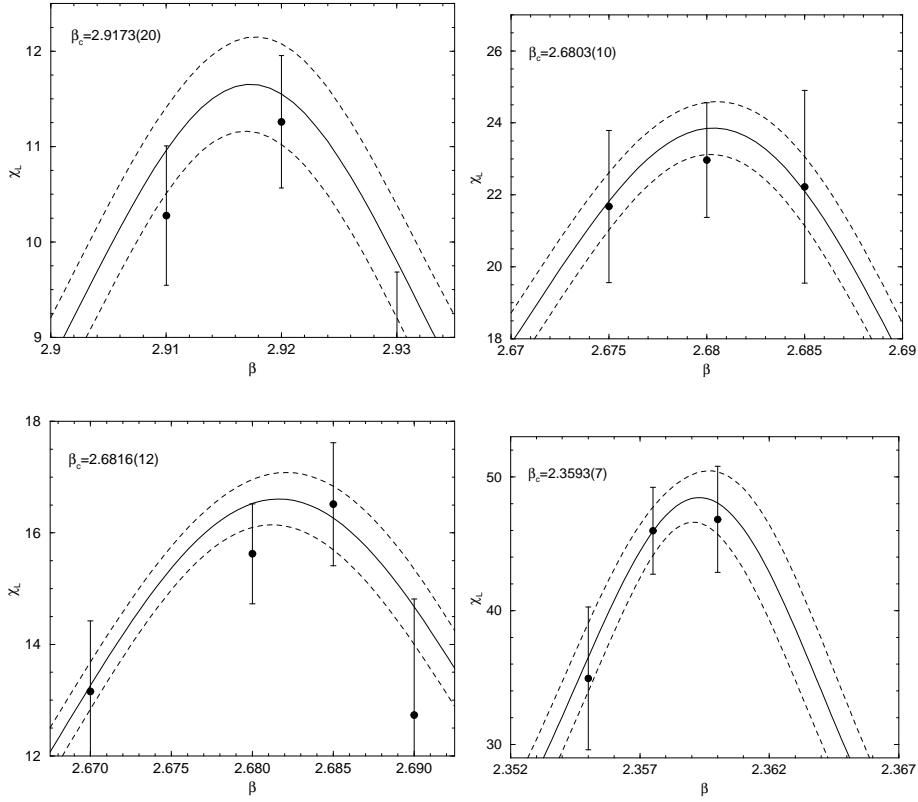


Figure 3.5: The Polyakov loop susceptibility on lattices of size 4×12^3 , 3×12^3 , 3×10^3 and 2×10^3 . The solid curves are the interpolations using the spectral density method, the dashed lines show the bootstrap error bands. The interpolations are based on the data of the simulations as displayed in table 3.2, 3.3 and 3.4.

N_σ	$\beta_c(N_\tau = 2)$	$\beta_c(N_\tau = 3)$	$\beta_c(N_\tau = 4)$
6	2.3552(24)		
8	2.3585(12)	2.6826(23)	
10	2.3593(7)	2.6816(12)	2.9119(31)
12		2.6803(10)	2.9173(20)
14			2.9222(20)
∞	2.3606(13)	2.6796(18)	2.9273(35)
h	0.14(9)	-0.05(7)	0.25(9)

Table 3.5: Results of the critical couplings β_c from the peak location of the Polyakov loop susceptibility and the corresponding infinite volume limit obtained according to relation (3.60). The finite size scaling constant h is also given.

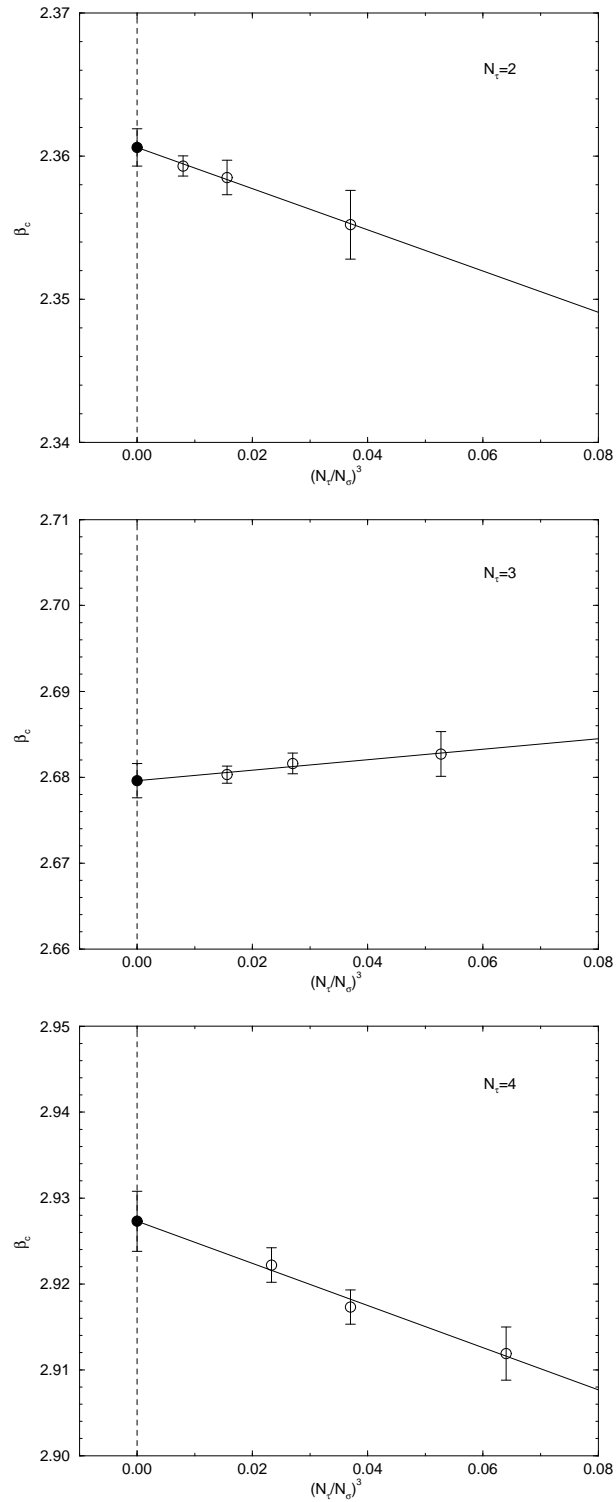


Figure 3.6: Finite size scaling of the critical couplings as a function of the inverse volume for $N_\tau = 2, 3$ and 4. The solid line represents a linear fit to the data and the filled circles are the corresponding infinite volume extrapolation.

It is also interesting to check the finite size scaling behaviour of the Polyakov loop susceptibility peak, χ_L^{peak} , as a function of the volume according to (3.59). These results are shown in figure 3.7, where we compare the ratio χ_L^{peak}/V with the value expected from the discontinuity of the Polyakov loop expectation value,

$$\frac{\chi_L^{\text{peak}}}{V} = \left(\frac{1}{2}\Delta L\right)^2. \quad (3.61)$$

For $N_\tau = 2$ and 4 the observed scaling looks convincing while it is not at all conclusive for $N_\tau = 3$. However, we have to admit that the volumes which we could exploit are too small to make any rigorous statements. Nevertheless, in all three cases we observe good agreement with the value from formula (3.61). As is evident from figure 3.7 and eq. (3.61), the expectation value of the Polyakov loop order parameter L gets smaller for larger values of N_τ . Indeed, it is expected to vanish exponentially in N_τ .

One last remark concerns the double peak structure in the distribution of observables expected at a first order phase transition. The gap between the peaks in the corresponding histograms experiences large volume dependence and is smeared out for small volumes. This effect is even more pronounced for the energy distribution and we could observe the double peak structure only at $N_\tau = 2$ where a volume ratio as large as $N_\sigma/N_\tau = 5$ could be reached. The corresponding energy histogram is shown in figure 3.3. The fact that this feature of the phase transition needs large spatial volumes, i.e. $N_\sigma/N_\tau \geq 5$, is in compliance with the observation made in simulations of the Wilson action on large volumes [37] where the double peak structure emerged clearly only on lattices as large as 4×24^3 .

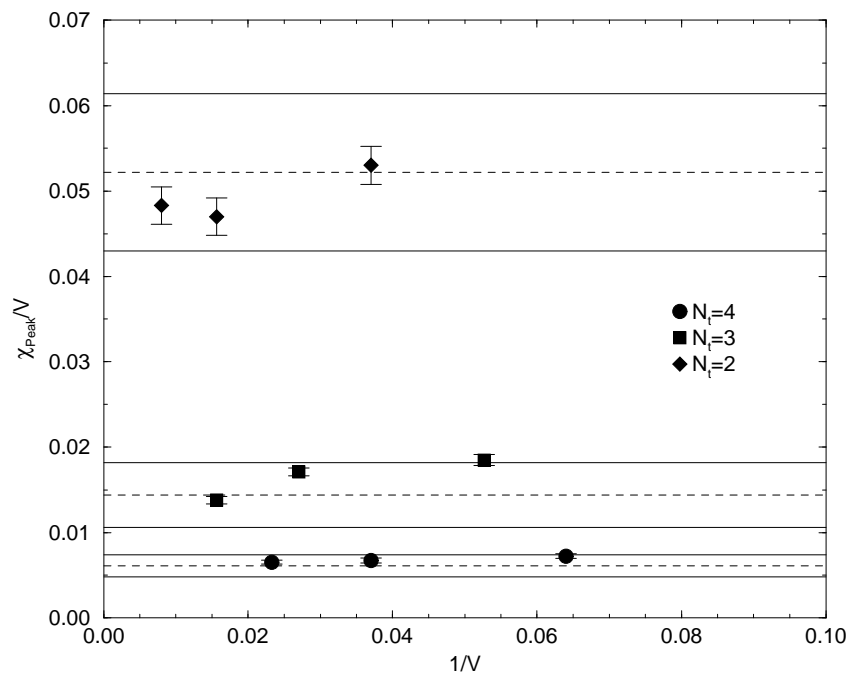


Figure 3.7: Finite size scaling of the Polyakov loop susceptibility peak normalized by the volume, χ_L^{peak}/V , for $N_\tau = 2, 3$ and 4. The dashed line represents the estimated value expected from equation (3.61) and the solid lines denote a crude error band estimation.

3.5.3 Error estimation

In this section we will discuss how we determine the errors on the measured quantities like the Polyakov loop susceptibility χ_L and the critical coupling β_c . We will first dwell on the different methods employed, discussing some of the properties like stability and reliability in general, and the application to the critical coupling in particular. At the end we discuss possible sources of systematic errors.

General considerations

There are many methods in business for estimating the standard error of a measurement. Widely used are the jackknife and bootstrap estimate of error. For an introduction see [50, 51].

The non-parametric bootstrap is conceptually the simplest of all techniques and reveals the basic idea of resampling most clearly. It extends the naive estimate of standard deviation of a measured quantity in an obvious way, so that it can be used to estimate the error on any arbitrary secondary quantity, no matter how complicated it may be.

The bootstrap can be cast into the following formal algorithm. Suppose a data set consisting of an independent and identically distributed (iid) sample of size N from an unknown probability distribution F ,

$$x_1, x_2, \dots, x_N \stackrel{iid}{\sim} F. \quad (3.62)$$

Let \hat{F} be the empirical probability distribution of the observed MC data $X_1 = x_1, X_2 = x_2, \dots, X_n = x_n$, giving probability mass $1/n$ on each X_i ,

$$X_1, X_2, \dots, X_n \stackrel{iid}{\sim} \hat{F}, \quad (3.63)$$

and $\hat{\theta} = \hat{\theta}(X_1, X_2, \dots, X_n)$ the estimator of an arbitrarily complicated secondary quantity.

1. Draw a random sample X_i^* with replacement from \hat{F} and calculate any secondary quantity $\hat{\theta}^* = \hat{\theta}(X_1^*, X_2^*, \dots, X_n^*)$.
2. Independently repeat step 1 a large number B of times to obtain bootstrap replications $\hat{\theta}^{*1}, \hat{\theta}^{*2}, \dots, \hat{\theta}^{*B}$.
3. Estimate the error $\delta\hat{\theta}$ on the estimator $\hat{\theta}$ by calculating the bootstrap error $\delta\hat{\theta}_{\text{Boot}}$,

$$\delta\hat{\theta}_{\text{Boot}} = \left(\frac{1}{B-1} \sum_{b=1}^B (\hat{\theta}^{*b} - \hat{\theta}^{*\cdot})^2 \right)^{1/2}, \quad (3.64)$$

where $\hat{\theta}^{*\cdot} = \sum_{b=1}^B \hat{\theta}^{*b} / B$.

Formally, $\delta\hat{\theta}_{\text{Boot}}$ is really defined as the limit of (3.64) as $B \rightarrow \infty$, however, in practice one is limited to some finite value of B .

For the reweighted Polyakov loop susceptibility we always used $B = 50$ and we checked in some cases that increasing this number did not have any significant effect on the error estimation.

The above algorithm applies to independent measurements only. Since we measure the Polyakov loop after every sweep, this premise is clearly violated. To circumvent this drawback one considers blocks of data and treats them as independent. The resampling is then done by choosing randomly the blocks and calculating the secondary quantity on the union of the chosen blocks. As a consequence of this procedure the error strongly depends on the size of the block. To avoid severe under- or overestimation of the error we calculated the bootstrap error as a function of the block size for each run at a given β -value. We observed that the bootstrap error always reached a stable plateau for block sizes around 500 to 1000 sweeps.

As a check for the reliability of the bootstrap we treated every sweep as independent and corrected for the residual autocorrelation by multiplying the error estimate by the factor $\sqrt{2\tau_{\text{int}}}$, where τ_{int} is the integrated autocorrelation time. The error estimates obtained in this way yielded values comparable to the bootstrap estimates, while showing weak instability with regard to β -runs having similar statistics. Nevertheless it supported our confidence in the bootstrap procedure of estimating the error.

Error estimate for β_c

The bootstrap error estimation described above extends to the multi-histogram reweighting technique in a straightforward manner. In sampling theory it is natural to consider stratified situations where the sample space \mathcal{H} is a union of disjoint strata \mathcal{H}_k ,

$$\mathcal{H} = \bigcup_{k=1}^K \mathcal{H}_k. \quad (3.65)$$

In the case of the deconfinement transition the \mathcal{H}_k 's denote the sample spaces of the k simulated β -values β_k . The data consist of separate iid samples of size N_k from each stratum,

$$x_{k1}, x_{k2}, \dots, x_{kN_k} \stackrel{iid}{\sim} F_k, \quad k = 1, \dots, K, \quad (3.66)$$

where F_k is an unknown probability distribution on \mathcal{H}_k . Observing $X_{ki} = x_{ki}$, $i = 1, \dots, n_k$, $k = 1, \dots, K$ in a MC simulation, define

$$X_{k1}, X_{k2}, \dots, X_{kn_k} \stackrel{iid}{\sim} \hat{F}_k, \quad k = 1, \dots, K, \quad (3.67)$$

as the empirical probability distribution for each stratum giving probability mass $1/n_k$ on the X_{ki} 's and yielding an arbitrary functional statistic

$$\hat{\theta} = \hat{\theta}(\hat{F}_1, \hat{F}_2, \dots, \hat{F}_K) \quad (3.68)$$

of an arbitrary secondary quantity. The bootstrap estimate of standard deviation is now obtained by the following algorithm:

1. Construct the \hat{F}_k 's.
2. Draw independent bootstrap samples X_{ki}^* , $i = 1, \dots, n_k$ from \hat{F}_k , $k = 1, \dots, K$ and calculate any secondary quantity $\hat{\theta}^* = \hat{\theta}(\hat{F}_1^*, \hat{F}_2^*, \dots, \hat{F}_K^*)$.
3. Independently repeat step 2, B times, obtaining bootstrap replications $\hat{\theta}^{*1}, \hat{\theta}^{*2}, \dots, \hat{\theta}^{*B}$.

4. Estimate the error $\delta\hat{\theta}$ on the estimator $\hat{\theta}$ by calculating the bootstrap error $\delta\hat{\theta}_{\text{Boot}}$,

$$\delta\hat{\theta}_{\text{Boot}} = \left(\frac{1}{B-1} \sum_{b=1}^B (\hat{\theta}^{*b} - \hat{\theta}^{*\cdot})^2 \right)^{1/2}, \quad (3.69)$$

where $\hat{\theta}^{*\cdot} = \sum_{b=1}^B \hat{\theta}^{*b} / B$.

As before, $\delta\hat{\theta}_{\text{Boot}}$ is formally defined as the limit of (3.69) as $B \rightarrow \infty$. Again, the algorithm applies to independent measurements only, thence we resample blocks of definite block size determined as mentioned above.

In the case of multi-histogram reweighting we can determine error estimates for any quantity involved like the spectral density function $W(S)$ as well as the Polyakov loop susceptibilities reweighted at some given β -value. This is how we determined the error bands in the figures showing the Polyakov loop susceptibility peaks. We go even a step further and determine the critical coupling β_c by locating the peak of the Polyakov loop susceptibility for every bootstrap sample, $\hat{\theta}^{*b} = \hat{\beta}_c^b$ and estimate the error on β_c from (3.69). Since the calculation of the $\hat{\beta}_c^b$'s involves many non-trivial steps, the estimated error has to be taken with caution. However, we checked for the stability and reliability of the estimate by employing several tests. For example we estimated the error on β_c using a block size of one measurement only and correcting with the usual factor $\sqrt{2\tau_{\text{int}}^{\text{max}}}$, where $\tau_{\text{int}}^{\text{max}} = \max(\tau_{\text{int}}^k, k = 1, \dots, K)$. This procedure usually yielded a slightly larger error estimate than with the standard bootstrap method.

As another more serious check we discarded one or several runs at given β -values in order to check for the stability of the peak location and to test consistency among different β -runs. In almost all cases the critical coupling β_c varied only within the usual 90% confidence interval ($\simeq \pm 1.6\delta\beta_c$), again supporting our reliance on the error estimation procedure employed.

Possible sources of systematic errors

While the previous sections deal with the error of statistical kind only, we are also facing the problem of undetected systematic errors. There are two possible main sources of systematic errors involved, firstly, incomplete thermalization, and secondly, elusive and thus insufficient statistics as explained below. While the first source is rather easy to detect and straightforward to circumvent, we do not know any cheap remedy for the cure of the latter except increasing the statistics so as to obtain enough phase flips.

As we already mentioned in section 3.5.1 we discarded a number of sweeps at the beginning of each run to eliminate effects due to incomplete thermalization. Usually leaving out the first 500 to 1000 sweeps were enough, depending on if one starts from a random configuration or from a configuration thermalized at a nearby β -value. In each case we checked that an increase in the number of discarded sweeps had no systematic effect on the mean value or the fluctuations of the quantity under consideration. In this way one can also rule out possible effects from hysteresis.

In one case ($N_t = 4, N_s = 14, \beta = 2.930$) we could observe such a systematic shift of the Polyakov loop susceptibility. Presumably this is a hint at having insufficient statistics at this β -value, however, it had no effect on the critical β -value obtained by reweighting.

As for the second source, the situation is more problematic. Near the phase transition the number of flips between one and the other phase is the crucial quantity as a measure of the quality of the collected data, rather than the number of sweeps. However, for larger lattices the system remains in one of the phases for longer periods of MC time, making it hard to decide if one is near the phase transition. For the largest lattice considered ($N_t = 4, N_s = 14$) we observed periods as large as 5000 sweeps in between the phase changes, thus yielding in this 'worst' case only of order 10 flips despite the large number of sweeps. Sometimes we observed that increasing the statistics only slightly yielded values for the susceptibility leaving the 95% confidence interval unexpectedly often, while not improving on the statistical error. This may be an indication that the statistical error runs into the trouble of easily underestimating the effective error near the phase transition, even when calculated with elaborated methods like the bootstrap. Thence having of order 10 to 20 flips near the phase transition is the lowest possible edge of statistics to have. However, the reweighting technique again seems to smooth over this fact in the manner that it combines the data from different β -values and thus enlarging the accessible information on the system by a considerable amount. In most cases the reweighting technique yielded a stable β_c -value already when considering only half of the statistics, and the increased statistics was effectively used only for consolidating and stabilizing this value.

Nevertheless, the danger of having elusive data can not be ruled out and only collecting larger statistics will turn this source of systematic error negligible.

3.6 Conclusions and outlook

In this chapter we have discussed in some detail the finite temperature deconfining phase transition in pure gauge theory and the determination of the corresponding critical couplings of the parametrized FP action at $N_\tau = 2, 3$ and 4. The small statistics and small lattice sizes accessible to us due to the computational overhead of the parametrized FP action present the main obstacles in our calculations. As is pointed out in the last section it would be desirable to have at least of the order of 20 flips or more between the two phases so as to exclude possible systematic effects. In addition, it would be useful to simulate on larger lattices like 4×16^3 and 3×14^3 in order to check if the finite size scaling region is really reached. Such studies on larger lattices are surely needed to clarify the situation at $N_\tau = 3$, where the strange finite size scaling behaviour is not yet understood. In this sense, the quoted errors are to be taken with great care, as discussed in section 3.5.3.

Another possible direction of future work is the determination of the critical couplings at $N_\tau = 5$ or 6 in order to check the scaling behaviour of the parametrized FP action at lattice spacings smaller than $a \simeq 0.15$.

It is clear that such projects are very demanding with respect to computer resources, however, there is no fundamental problem to it. Due to the sophisticated analysis methods which we have developed and which allow one to dig out the needed physical information on the system, it is enough to perform long enough simulations near a phase transition at three or four coupling values only. This, of course, simplifies enormously the task of determining the phase transitions.

Chapter 4

Scaling properties of the FP action

4.1 Introduction

In this chapter we aim at a systematic quantization of the improvements achieved with the present parametrization of the FP action. It is of crucial importance for any improvement procedure to size the remaining lattice artifacts and to check the extent to which lattice artifacts are removed at the physically interesting lattice spacings. Another issue is to define the range of validity of the FP program, i.e. to check for a possible breakdown of the approach, if present, at very coarse lattice spacings.

Both these matters can be tackled by investigating the scaling behaviour of renormalization group (RG) invariant quantities on a large range of (coarse) lattice spacings. Any physical quantity measured on the lattice is renormalized by appropriately tuning the lattice spacing when the continuum limit $\beta \rightarrow \infty$ is taken and thence any given quantity measured in units of the lattice spacing scales according to its dimension. Scaling can best be seen in dimensionless ratios or products of physical quantities which are RG invariant and thus should be constant for all values of the gauge coupling and, correspondingly, for all lattice spacings. Any deviation from this scaling behaviour is due to the presence of lattice artifacts.

There is an infinitely large set of quantities on which the scaling behaviour of different actions, and in particular the FP action, can be tested. Among them are the static quark-antiquark potential and quantities derived from it like the string tension σ or the hadronic scale r_0 , the charmonium, the torelon and the glueball spectrum, the deconfining phase transition temperature as well as other thermodynamic quantities like the free energy, the latent heat and the surface tension in finite temperature lattice gauge theory and the topological susceptibility to mention only a few. Some of these quantities have already been investigated in the context of FP actions. For example in [6, 12] the scaling of the torelon mass and the related string tension has been exploited as well as the static potential at finite temperature. Scaling of the topological susceptibility

has been successfully tested in [12] and excellent scaling of the free energy density has been observed in [52, 53].

The quantities which we have chosen in this work in order to test the scaling behaviour of the FP action are the deconfining phase transition temperature T_c , the static quark-antiquark potential at zero temperature, the hadronic scale r_0 and the effective string tension σ .

Another tempting and physically very interesting possibility to size lattice artifacts and to compare scaling of different actions is provided by the glueball spectrum. However, this is a heavyset field and therefore deserves a chapter by its own, cf. chapter 5.

The scaling checks will be pushed to the extreme by exploring the behaviour of the FP action on coarse configurations with very large fluctuations corresponding to $N_\tau = 2$. This situation is presumably not relevant for practical applications, and indeed, it becomes more and more difficult to measure physical quantities due to the very small correlation length and the rapidly vanishing signals. Nevertheless, it is still interesting to investigate this situation in order to check the region in which the classical approximation to the renormalization group trajectory is still valid and, in addition, it might give the possibility of connecting to strong coupling expansions of the gauge theory [54].

Another matter concerns asymptotic scaling. As opposed to scaling, asymptotic scaling tests the behaviour of dimensionful quantities near the continuum limit. In particular, it predicts the dependence of a given quantity on the bare coupling g . How far a specific lattice gauge action deviates from asymptotic scaling is a legitimate and important question. However, it is addressed here only at the very edge for the case of r_0 .

The chapter is organized as follows. In the first section we will investigate the scaling behaviour of the heavy quark-antiquark potential, thereby describing procedures and techniques for measuring the potential on the lattice. The second section deals with the scaling of the critical temperature of the deconfining temperature, T_c , and quantities related to the static potential like r_0 and σ , and reports on the details of the extraction of these quantities. Finally, in the last section we summarize the results and give a first, preliminary conclusion on the scaling behaviour of the FP action.

4.2 Scaling of the static quark-antiquark potential

One of the rather easily accessible quantities mentioned in the introduction is the static quark-antiquark potential. It provides an immediate and effective test of scaling: the combinations r/r_0 and $r_0V(r)$ are dimensionless and thus RG invariant. The potential data measured at different values of the gauge coupling β should overlap with each other when the scaling region of this observable is reached. In addition, one can calculate the quantities r_0 and σ from the potential

as explained below and they can be used in turn for testing the scaling of the dimensionless combinations $r_0 T_c$, $T_c/\sqrt{\sigma}$ and $r_0\sqrt{\sigma}$.

Violations of rotational invariance have been found to be strong for the standard plaquette gauge action at coarse lattice spacings [55, 56, 6] and therefore it is desirable to improve the gauge action also on large fluctuations. In [8] it was pointed out that for an appropriately chosen renormalization group transformation one finds a FP action with short interaction range and small violations of rotational symmetry in the static quark-antiquark potential even at shortest distances. This was shown by means of the static potential at finite temperature using FP Polyakov loops in the linear approximation. The remaining rotational symmetry violations in the potential were suspected to originate from the missing direct interaction between diagonally separated links in that former parametrization of the FP action given in [8]. The new parametrization presented in this work includes such interaction terms, which are certainly present in the true FP action, and thus is expected to show even less violations of rotational invariance in the potential as observed before. Our intention for measuring the static quark-antiquark potential is however not to test the rotational invariance, but rather aims at the determination of r_0 and σ .

4.2.1 The static potential

It is well known that the static quark-antiquark potential in lattice gauge theory is related to the expectation value of the rectangular Wilson loop $\mathcal{W}(R, T)$ via

$$\langle \mathcal{W}(R, T) \rangle \sim e^{-V(R)T} \quad (4.1)$$

for large T . Here, R and T denotes the spatial and temporal extent of the Wilson loop, respectively. One can interpret the expectation value of a Wilson loop pictorially as the creation of a quark-antiquark pair at time $t = 0$ at point $x = R/2$, separating instantaneously to $x = R$ and $x = 0$ and then evolving for time T until it annihilates. Thus the potential can be determined in principle by calculating the limit

$$V(R) = \lim_{T \rightarrow \infty} -\frac{1}{T} \ln \langle \mathcal{W}(R, T) \rangle. \quad (4.2)$$

In (pure) lattice gauge theory the potential is expected to confine quarks and, more precisely, to grow linearly for large separations,

$$\lim_{R \rightarrow \infty} V(R) \sim \sigma R, \quad (4.3)$$

where σ is the so called string tension. This area law behaviour of the Wilson loop is confirmed in every order of a systematic strong coupling expansion for σ [57, 58]. Per contra, from asymptotic freedom one expects a Coulomb-like interaction $V(R) \sim \alpha/R$ of the quark-antiquark pair at short distances. Therefore, a simple ansatz describing (phenomenologically) a static quark-antiquark potential, simultaneously exhibiting confinement and asymptotic freedom is the Cornell potential [59],

$$V(R) = V_0 + \frac{\alpha}{R} + \sigma R. \quad (4.4)$$

For the understanding of confinement the ability to calculate the potential non-perturbatively is crucial. At present the only non-perturbative calculation

of the quark-antiquark potential is by determining the expectation value of the Wilson loop numerically in Monte Carlo simulations. For all practical purposes, one is restricted to finite R and T and the relative errors of the Wilson loop expectation values increase exponentially with temporal extension T . To reduce these statistical fluctuations one can use thermally averaged temporal links [60], but it is even more vital to enhance the overlap with the physical ground state of the system. This can be achieved by invoking for instance iterative spatial smearing techniques (see e.g. [61]). The techniques which we use are described in detail in section 4.2.3.

4.2.2 Determination of the spatial scale

An important part of any lattice simulation is the determination of a physical scale in order to convert quantities measured on the lattice into physical units. This can be accomplished by choosing one physical quantity as a reference scale. Any quantity which can be easily and accurately determined numerically on the lattice as well as experimentally will do. A typical reference quantity in lattice gauge theories is the mass of a low-lying hadron, however, in pure gluon-dynamics we have to resort to a purely gluonic quantity (which, nevertheless, should be defined in full QCD as well). As outlined in section 3.4 the critical temperature T_c of the deconfinement phase transition is such a reference scale. More easily accessible is the determination of the scale through the static quark-antiquark potential, where one refers to the string tension σ to set the scale. Nevertheless, this method is plagued by two major difficulties: firstly and most importantly, the noise/signal ratio becomes large in the region where one needs an accurate determination of the potential, cf. eq. (4.1) and (4.3). In addition, due to the fact that the excited string has a small energy gap at large distances R , the ground state becomes difficult to resolve with standard methods. Secondly, and less importantly, the string tension is not well defined in full QCD due to string breaking.

To circumvent these problems a hadronic scale r_c was introduced [62] through the force $F(r)$ between static quarks in the fundamental representation at intermediate distances $0.2 \text{ fm} \leq r \leq 1.0 \text{ fm}$, where we have best information available from phenomenological potential models [59, 63]. The advantages of this choice are manifold: the scale is defined precisely both in pure gauge theory and in full QCD and it can be determined well numerically with good statistical precision. This quantity is therefore regarded to be technically more appropriate than the string tension to fix the scale. We have

$$r_c^2 V'(r_c) = r_c^2 F(r_c) \equiv c, \quad (4.5)$$

where originally [62] $c = 1.65$ was chosen yielding a value $r_c \equiv r_0 \simeq 0.49 \text{ fm} = (395 \text{ MeV})^{-1}$ from the potential models.

However, also this alternative way of setting the scale is hampered by some drawbacks as will be pointed out in section 4.3.2. Firstly, there is no 'unique' method for calculating the derivative in eq. (4.5). For example, one can use the ansatz in eq. (4.4) for interpolating the potential either locally around r_c only, or globally by including as many potential values as possible. In addition, the possibility of choosing different points r_c for determining the force in (4.5) introduces ambiguities which are beyond the statistical uncertainties, particularly

on coarse lattices, and indeed, measurements of r_0 from several groups differ significantly from each other¹. It is therefore fair to say, that, since the ambiguities become negligible on fine lattices, r_0 is an appropriate scale for performing continuum limit extrapolations from fine lattices, however, its use on coarse lattices with $a \geq 0.1$ fm is questionable, especially when an accuracy level of less than 2% is required.

In order to estimate the systematic ambiguities we have determined r_0 from global fits to the potential as well as from local fits using different values of r_c and c . Referring to precision measurements of the low-energy reference scale in quenched lattice QCD with the Wilson action [64, 65, 66] we have collected values for c and r_c in table 4.1. These are the values which we use for the

r_c/r_0	c
0.662(1)	0.89
1.00	1.65
1.65(1)	4.00
2.04(2)	6.00

Table 4.1: Parameter values for the determination of the hadronic scale through eq. (4.5). The numbers in the first line and in the two last lines are from high-statistics measurements of the static $q\bar{q}$ -potential using the Wilson action [66, 65].

determination of the spatial scale, but unfortunately they already incorporate some of the systematic ambiguities discussed above.

4.2.3 Simulation details

We performed simulations with the FP action at six different β -values, of which three correspond to the critical couplings determined in chapter 3. Configurations were updated by combining a Metropolis sweep with an overrelaxation sweep acting on SU(2) subgroups. The spatial extent of the lattices were chosen to be at least ~ 1.5 fm, based on observations in [66, 67]². We measured the correlation matrix of Wilson loops after every second or fifth updating sweep, cf. the run parameters in table 4.2 where we list the values of the couplings, the lattice volumes and sizes together with numbers relevant for the obtained statistics.

In order to enhance the overlap with the physical ground state of the potential we exploited smearing techniques. The operators which we measured in the simulations are constructed using the spatial smearing of [61]. The smoothing of the spatial links has the effect of reducing excited-state contaminations in the correlation functions of the Wilson loops in the potential measurements. The smoothing procedure we use consists of replacing every spatial

¹See for example the collection of data from measurements with the Wilson action in [64].

²Within their statistical errors ($\simeq 1\%$) the authors of [66, 67] do not observe any finite size effects affecting the potential values on varying the spatial lattice extent between $L = 0.9$ fm and $L = 3.3$ fm. On the other hand, the authors of [65] observe significant finite volume effects on the 1 - 1.5 % level for the string tension σ on lattices as large as $L = 1.7$ fm, while r_0 is much less affected.

β	lattice volume	lattice size [fm]	# bins	bin size	# meas./bin
3.400	14^4	1.45	43	180	90
3.150	12^4	1.61	42	500	50
2.927	14^4	2.39	40	200	40
2.860	10^4	1.84	43	180	90
2.680	12^4	2.72	51	200	40
2.361	12^4	4.02	57	200	40

Table 4.2: Run parameters for the simulations of the static quark-antiquark potential. Values for the coupling, the lattice volumes and sizes are listed together with characteristic numbers for the obtained statistics.

link $U_j(n)$, $j = 1, 2, 3$ by itself plus a sum of its neighboring spatial staples and then projecting back to the nearest element in the SU(3) group³:

$$\begin{aligned} \mathcal{S}_1 U_j(x) \equiv \mathcal{P}_{\text{SU}(3)} \left\{ U_j(x) + \lambda_s \sum_{k \neq j} (U_k(x) U_j(x + \hat{k}) U_k^\dagger(x + \hat{j}) \right. \\ \left. + U_k^\dagger(x - \hat{k}) U_j(x - \hat{k}) U_k(x - \hat{k} + \hat{j})) \right\}. \end{aligned} \quad (4.6)$$

Here, $\mathcal{P}_{\text{SU}(3)} Q$ denotes the unique projection onto the SU(3) group element W , which maximizes $\text{ReTr}(WQ^\dagger)$ for any 3×3 matrix Q . The smeared and SU(3) projected link $\mathcal{S}_1 U_j(x)$ retains all the symmetry properties of the original link $U_j(x)$ under gauge transformations, charge conjugation, reflections and permutations of the coordinate axes. The whole set of spatially smeared links, $\{\mathcal{S}_1 U_j(x), x \in L^4\}$, forms the spatially smeared gauge field configuration. An operator \mathcal{O} which is measured on a n -times iteratively smeared gauge field configuration is called an operator on smearing level \mathcal{S}_n , or simply $\mathcal{S}_n \mathcal{O}$. In the simulation of the static $\bar{q}q$ -potential we used smearing levels \mathcal{S}_n with $n = 0, 1, 2, 3, 4$. The smearing parameter was chosen to be $\lambda_s = 0.2$ in all cases.

The correlation matrix of spatially smeared Wilson loops are constructed in the following way⁴. At fixed t we first form smeared string operators along the three spatial axes, connecting \vec{x} with $\vec{x} + R\hat{i}$,

$$\begin{aligned} \mathcal{S}_n V_i(\vec{x}, \vec{x} + R\hat{i}; t) = \\ \mathcal{S}_n U_i(\vec{x}, t) \mathcal{S}_n U_i(\vec{x} + \hat{i}, t) \dots \mathcal{S}_n U_i(\vec{x} + (R-1)\hat{i}, t), \quad i = 1, 2, 3, \end{aligned} \quad (4.7)$$

and unsmeared temporal links at fixed \vec{x} , connecting t with $t + T$,

$$V_4(t, t + T; \vec{x}) = U_4(\vec{x}, t) U_4(\vec{x}, t + 1) \dots U_4(\vec{x}, t + (T - 1)). \quad (4.8)$$

³The SU(3) projection is done by applying SU(2) subgroup projections.

⁴Note that we are concerned with a 5×5 correlation matrix in the case where we use smearing levels \mathcal{S}_n with $n = 0, 1, 2, 3, 4$.

The smeared Wilson loop⁵ is then obtained by calculating

$$\mathcal{W}_{lm}(R, T) = \sum_{\vec{x}, t} \sum_{i=1}^3 \text{Tr} \mathcal{S}_l V_i(\vec{x}, \vec{x} + R\hat{i}; t) V_4(t, t + T; \vec{x} + R\hat{i}) \\ \mathcal{S}_m V_i^\dagger(\vec{x}, \vec{x} + R\hat{i}; t + T) V_4^\dagger(t, t + T; \vec{x}), \quad (4.9)$$

and finally we define the correlation matrix according to

$$C_{lm}(R, T) = \langle \mathcal{W}_{lm}(R, T) \rangle = C_{ml}(R, T), \quad (4.10)$$

where the average is estimated by means of the Monte Carlo simulation. In the following the correlation matrices are analyzed using variational techniques as described in the subsequent section.

4.2.4 Analysis details and results

In order to extract the physical scale through equation (4.5) we need an interpolation of the potential and correspondingly the force between the quarks for arbitrary distances r not restricted to integers corresponding to the lattice sites. This interpolation of $V(r)$ is achieved by fitting a potential of the form (4.4) to the measured potential values. We use this simple ansatz in order to calculate the force (derivative of V) in eq. (4.5). The potential can be very well described with this ansatz, but of course we do not claim that it has exactly this form.

We employ a two step procedure for the fitting: First we extract the potential values $V(r)$ for each r separately using the variational techniques described in section D.1. This method also gives a linear combination of the string operators $\mathcal{S}_n V$, $n = 0, \dots, 4$, which projects sufficiently well to the ground state of the string, i.e. eliminates the closest excited string states. Based on effective masses and on a χ^2 -test taking all temporal correlations into account as described in section D.2 we choose a plateau region from t_{\min} to t_{\max} where we fit the exponential form $Z(r) \exp(-tV(r))$ to the ground state correlator, carefully checking the stability of the fit under variation of the fit parameters. The results of these fits are collected in table F.2 in appendix F, where we list the plateau regions (fit range), the extracted potential values $V(r)$ and the χ^2 per degree of freedom, χ^2/N_{DF} . The uncertainties in the extracted values for $V(r)$ are calculated using a non-parametric bootstrap method.

Once we have determined a suitable plateau region for each r we perform the second step by fitting the expression $Z(r) \exp(-t(V_0 + \alpha/r + \sigma r))$ directly to the correlation matrices $\mathcal{W}_{lm}(r, t)$ projected to the ground state of the string, simultaneously for all r and the previously chosen t -values. This step allows to take into account all correlations among the correlation matrix elements for both different r and t by using a χ^2 -function with the corresponding covariance matrix. The fit range in r is chosen by carefully examining the χ^2 -function and the stability of the fitted parameters aV_0 , α and σa^2 , while keeping the fit ranges in the t -values fixed for each r separately. Again, the quoted errors are estimated through the fluctuations of the fit parameters and all other indirectly calculated quantities like r_0/a determined from the c -values in table 4.1, on

⁵Let us remark that we measure the on-axis potential only, i.e. Wilson loops having spatial extent in the direction of the lattice axes $i, i = 1, 2, 3$ only.

500 bootstrap samples. The results of the global fits are tabulated in table 4.3, where we quote the fit range in r , the parameters $aV_0, \alpha, \sigma a^2$ together with their errors for all β -values. The non-monotonic variation of $\alpha = \alpha(\beta)$ shows clearly, that α and σa^2 are effective fit parameters. The last column quotes the χ^2 per degree of freedom, χ^2/N_{DF} .

β	fit range	aV_0	α	σa^2	χ^2/N_{DF}
3.400	2 - 6	0.7805(7)	-0.251(9)	0.0629(13)	1.02
3.150	2 - 5	0.820(15)	-0.285(20)	0.0992(27)	0.75
2.927	2 - 6	0.812(16)	-0.272(20)	0.1606(33)	1.35
2.860	1 - 4	0.8007(48)	-0.2623(33)	0.1885(17)	1.17
2.680	1 - 4	0.7766(52)	-0.2547(37)	0.2871(15)	0.43
2.361	1 - 4	0.615(11)	-0.1791(78)	0.6286(37)	0.99

Table 4.3: Results from global correlated fits of the form (4.4) to the static quark potentials. The second column indicates the fit range in r and the last column χ^2 per degree of freedom, χ^2/N_{DF} .

Having at hand an interpolation of the static potential for each β -value, we are able to determine the hadronic scale r_0 in units of the lattice spacing through eq. (4.5). The value of c is chosen appropriate to the coarseness of the lattice and the fit range in r . In table 4.4 we list the final results and the errors together with the value of c from which r_0/a is calculated.

β	N_τ	r_0/a	c
3.400		4.81(3)	0.89
3.150		3.71(3)	1.65
2.927	4	2.93(1)	1.65
2.860		2.713(9)	1.65
2.680	3	2.205(3)	1.65
2.361	2	1.494(3)	4.00

Table 4.4: Results for the hadronic scale r_0/a from correlated fits of the form (4.4) to the static quark-antiquark potentials. The last column indicates the value of c (cf. table 4.1) from which r_0/a is determined through eq. (4.5).

As mentioned in the introduction to this section, the static $\bar{q}q$ -potential is an immediate, non-trivial and effective test of scaling. Since both the ratios r/r_0 and r_0V are RG invariant, one expects the potentials expressed in terms of the hadronic scale as a function of r/r_0 to lie on top of each other after subtracting an unphysical constant. This constant in the potential is fixed through the convention that $V(r_0) = 0$ for each potential. The resulting potential values are displayed in figure 4.1. If we also plot the fits to the potential values we observe that the curves can scarcely be distinguished from each other. Therefore we only draw one single curve (dashed line) obtained by a simultaneous fit to all the data respecting the previously chosen fit ranges in r . The curve serves to guide the eye and shows the function (4.4) appropriately rescaled and normalized.

It is also useful to know how r_0/a scales with β . Thence we parametrize the

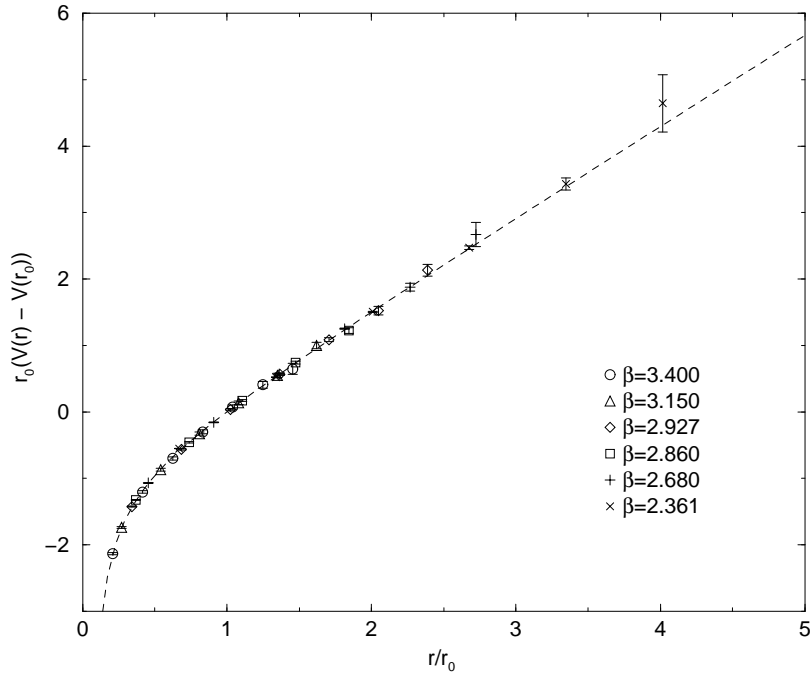


Figure 4.1: Scaling of the static $\bar{q}q$ -potential $V(r)$ expressed in terms of the hadronic scale r_0 . The unphysical constant $r_0V(r_0)$ has been subtracted for each lattice spacing so that the curves all have the same value at $r/r_0 = 1$. The dashed line is drawn to guide the eye and shows a fit of the data to the function (4.4) appropriately rescaled and normalized.

results in terms of a smooth function of β in order to provide an interpolating formula for r_0/a at arbitrary values of β in the interval $2.361 \leq \beta \leq 3.4$, thereby checking for the onset of asymptotic scaling. The leading universal behaviour of the solution of the renormalization group equation for the bare coupling yields

$$a/r_0 = A e^{-1/(2b_0 g_0^2)} (b_0 g_0^2)^{-b_1/(2b_0^2)} (1 + \mathcal{O}(g_0^2)), \quad (4.11)$$

where $b_0 = 11/(4\pi)^2$ and $b_1 = 102/(4\pi)^4$ are the universal one- and two-loop coefficients in the perturbation expansion of the β -function and A is related to the Λ -parameter. $\mathcal{O}(g_0^2)$ indicates non-universal contributions from higher order terms. Therefore, from the leading behaviour $(a/r_0) \sim \exp(-\beta/(12b_0))$ with $\beta = 6/g_0^2$, we infer a phenomenological description of $\ln(a/r_0)$ in terms of a polynomial,

$$\ln(a/r_0) = \sum_{k=0}^p a_k (\beta - 3)^k. \quad (4.12)$$

We obtain a good description of the data already with $p = 2$ for which we plot the resulting curve together with the data points in figure 4.2. The deviations of the curve from the data is at least one order of magnitude smaller than the statistical error. The parameters of the $p = 2$ and $p = 3$ polynomial are given in table 4.5 and can directly be compared to analogous formulas for the Wilson action [65, 64]. Note the smallness of the higher order coefficients in our fits.

	$p = 2$	$p = 3$
a_0	-1.1539(18)	-1.1536(31)
a_1	-1.0932(68)	-1.0925(97)
a_2	0.132(11)	0.129(29)
a_3		-0.005(51)
χ^2/N_{DF}	0.20	0.29

Table 4.5: Parameters of the phenomenological description of $\ln(a/r_0)$ in terms of a polynomial of order $p = 2$ and $p = 3$, r_0/a from table 4.4 as determined from global fits.

	$p = 2$	$p = 3$
a_0	-1.1622(24)	-1.1615(34)
a_1	-1.0848(95)	-1.082(13)
a_2	0.156(17)	0.146(39)
a_3		0.020(70)
χ^2/N_{DF}	1.31	1.92

Table 4.6: Parameters of the phenomenological description of $\ln(a/r_0)$ in terms of a polynomial of order $p = 2$ and $p = 3$ for the values of r_0/a obtained from local fits, table 4.9.

When using the interpolating formula one should include a relative uncertainty of 0.2% at $\beta = 2.361$ growing linearly to 0.6% at $\beta = 3.40$ and corresponding roughly to the statistical accuracy of the data⁶.

⁶Note, that we did not take into account the uncertainty in the determinations of r_0/a

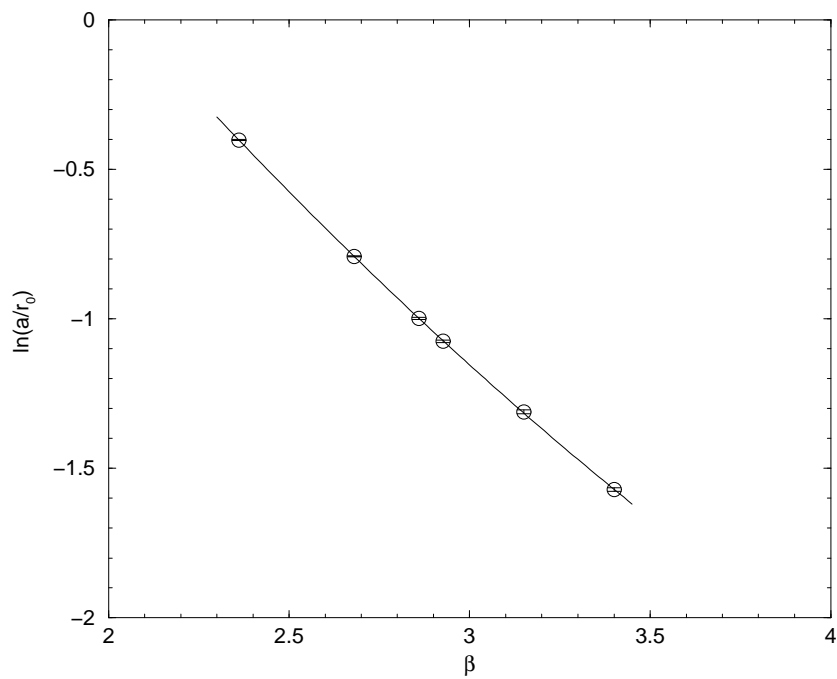


Figure 4.2: The measured data points of $\ln(a/r_0)$ (circles) and their phenomenological description in terms of a polynomial quadratic in β (solid line). The plotted points are the values of r_0/a from the local fits.

Let us finally draw the conclusion that the potential data measured with the FP action shows excellent scaling behaviour over the whole region of r/r_0 and for all values of β investigated. We also observe a smooth and nearly exponential change of the hadronic scale under variation of the gauge coupling. Of course, these statements are moderated by the fact that the potential itself does not possess a lot of structure and, indeed, a nice scaling of the potential is also observed for the Wilson gauge action, at least above $\beta_W \sim 6.0$. Already a crude and non-elaborated determination of r_0/a is enough to observe nice scaling behaviour. Although the scaling of the potential provides a first non-trivial test and a consistency check for the FP action, further tests are necessary.

4.3 Scaling of the critical temperature and $r_0\sqrt{\sigma}$

To further study the scaling properties of the FP action we examine renormalization group invariant combinations of physical quantities like r_0T_c , $T_c/\sqrt{\sigma}$ and $r_0\sqrt{\sigma}$. The first two are combinations of two completely independently determined quantities and therefore provide a highly non-trivial scaling test of the FP action and allow in principle to quantify lattice artifacts. In particular r_0T_c provides a high precision scaling test where the Wilson action shows scaling violations of the order of 4% at $N_\tau = 4$, but already less than 1.5% at $N_\tau = 6$. Therefore it requires a very precise determination of the reference scale r_0 . The third combination, $r_0\sqrt{\sigma}$, is made of two quantities which are both calculated from the static quark-antiquark potential and therefore are expected to be strongly correlated. Nevertheless, since the quantities are determined rather independently as we will see below, it still provides a non-trivial scaling test.

In this section we present and discuss the results for the FP action and compare them to results obtained from the Wilson action and different improved actions whenever it is possible. A complete and detailed collection of the data obtained with the FP action is given in appendix F.

4.3.1 $T_c/\sqrt{\sigma}$

Let us first look at the ratio $T_c/\sqrt{\sigma}$, the deconfining temperature in terms of the string tension⁷. In figure 4.3 we compare the results from the FP action with data obtained from simulations with different other actions.

The range of N_τ -values for the calculations with the standard plaquette action and the accuracy, with which the string tension is determined, is impressive and gives clear evidence for the continuum value of the deconfining temperature in units of the string tension. In table 4.7 we collect all available continuum extrapolations together with the results for the FP action. The data obtained with the Wilson action is taken from [49] where they use the T_c values at $N_\tau = 4$ and 6 from [47] and extrapolate finite volume data for T_c at $N_\tau = 8$ and 12 from [47] to infinite volume. For the value of $\sqrt{\sigma}$ they use the string tension parametrization given in [65]. The data for the 1×2 tree level improved action

stemming from different values of c in formula (4.5). This will be discussed in detail in section 4.3.2.

⁷We do not claim that the quantity σ is the string tension, but rather follow the attitude commonly adopted in the literature which denotes the quantity σ obtained from 3 or 4 parameter fits to the static potential as the string tension.

action	β	$T_c/\sqrt{\sigma}$
FP action	2.927	0.624(7)
	2.680	0.622(8)
	2.361	0.628(11)
Wilson [49]	∞	0.630(5)
1×2 [49]	∞	0.634(8)
DBW2 [68]	∞	0.627(12)
Iwasaki [42]	∞	0.651(12)
Bliss [69]	∞	0.659(8)

Table 4.7: Results of the deconfining temperature in units of the string tension obtained with the FP action and continuum values from different other actions. For completeness we also include the value by Bliss et al. [69] from a tree level and tadpole improved action. All continuum extrapolations are from a reanalysis by Teper [70].

is again taken from [49]. The data denoted by RG improved action is obtained with the Iwasaki action [71] and is taken from [42]. Finally we also quote the results from the QCD-TARO collaboration [68] obtained with the DBW2 action⁸. The extrapolation of the Wilson, the DBW2 and the Iwasaki data to the continuum is from [70] where a careful reanalysis is done.

Let us make the following remarks in order to judge the results. Since for the determination of the string tension one is interested in the long distance behaviour of the potential one usually follows the strategy to fix the Coulomb-like term in the fit-ansatz⁹, i.e. to perform two-parameter fits in aV_0 and σa^2 only. In addition one includes the off-axis potential values and corrects for distortion effects at short distances due to missing rotational invariance either by including the effects of the tree level one-gluon exchange in the force when working with the Wilson action [62, 64] and by systematically increasing the lower bound of the fitting range.

In contrast to this elaborated procedure we followed a much simpler approach. As described above we simply perform fits to the on-axis potential values only and therefore we are limited to small variations of the fitting range. Nevertheless, the values of σ obtained in this way and quoted in table 4.3 are stable and vary only within their statistical errors over the whole set of sensibly considered fit ranges. However, the error on σ changes considerably, i.e. up to a factor of 5, depending on whether distance $r = 1$ is taken into account or not. Just to play safe we neglect distance $r = 1$ in the fits, even if the χ^2 would allow it, to obtain the following conservative values¹⁰:

These are the values which are displayed in figure 4.3 together with the data as mentioned above. Our data is compatible within one standard deviation with the continuum extrapolation of the Wilson data and we observe scaling of the FP action within the statistical errors over the whole range of coarse lattices considered corresponding to values of $N_\tau = 2, 3$ and 4. Nevertheless, to make

⁸DBW2 means "doubly blocked from Wilson in two coupling space".

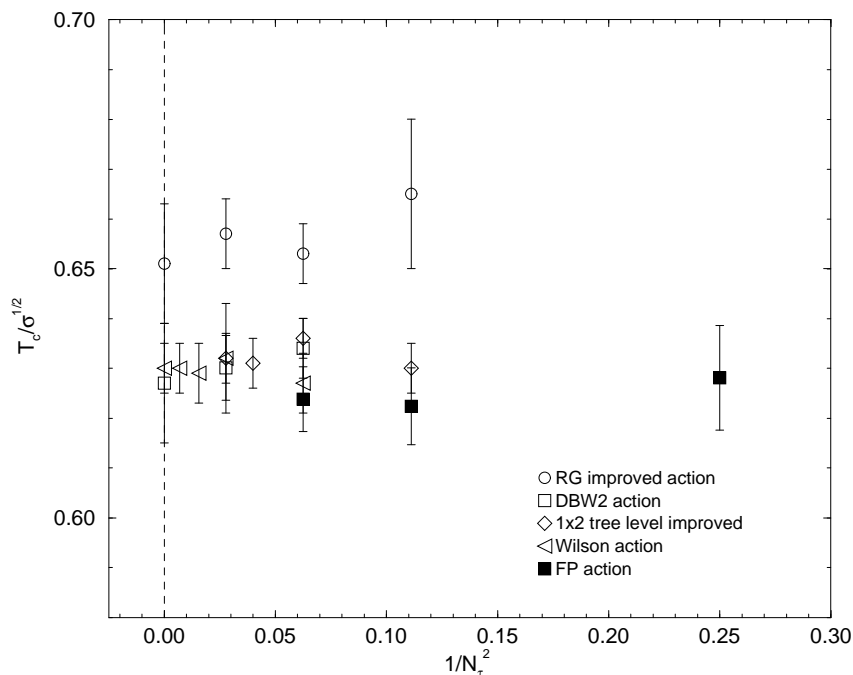
⁹For large distances the coefficient of this term is expected to be determined by string fluctuations, $\alpha = -\pi/12$.

¹⁰The details of the corresponding fits can be found in the appendix.

N_τ	4	3	2
β	2.927	2.680	2.361
σa^2	0.161(3)	0.286(7)	0.634(22)
$T_c/\sqrt{\sigma}$	0.624(7)	0.622(8)	0.628(11)

Table 4.8: Values for σ and $T_c/\sqrt{\sigma}$.

a more rigorous statement and a more stringent check of the scaling of the FP action it is certainly necessary to include off-axis potential values in order to check more reliably the stability of σ under variation of the fit range.

Figure 4.3: $T_c/\sqrt{\sigma}$ vs. $1/N_\tau^2$ for different actions. See text for details.

4.3.2 $r_0 T_c$

As was already pointed out by several authors [62, 65] there are clearly drawbacks to using the string tension to set the scale. This is first of all due to the fact that, since the string tension is a long-distance quantity, one needs the potential in a regime where the relative errors usually are getting large, and secondly, however less important for our purposes, the string tension is not well defined in full QCD. To avoid these problems a new way to set the scale via the force between a heavy quark and antiquark was introduced [62] in order to define an intermediate distance scale r_0 . This section will therefore deal with the RG invariant quantity $r_0 T_c$, so as to provide a high precision scaling test of the FP action and to size the remaining lattice artifacts.

Unfortunately, precise determination of r_0/a is missing in the literature except for the Wilson action [65, 64] and, unlike to $T_c/\sqrt{\sigma}$, we are not able to compare our data to other actions such as the Iwasaki, DBW2 or the 1×2 tree level improved action. Indeed, the determination of r_0/a is a delicate issue and systematic effects due to different methods of calculating the force can be sizeable. Due to the fact that extracting the derivative of the potential from a discrete set of points is not unique, the intrinsic systematic uncertainty is not negligible at intermediate and coarse lattice spacings $a \geq 0.15$ fm. For example, in an accurate scale determination of the Wilson gauge action in [65] the authors quote a value of $r_0/a = 2.990(24)$ at $\beta_W = 5.7$. This is to be compared with the precision computation of the scale with the same action in [64] where the authors obtain $r_0/a = 2.922(9)$ at the same β -value. In view of the claim in [65] to have included all systematic errors and the high relative accuracy ($\sim 0.3\%$) of the data in [64], this systematic difference on the $2 - 3\%$ level is a serious matter. Even on fine lattices there are large discrepancies: at $\beta_W = 6.2$ the authors of [64] obtain $r_0/a = 7.38(3)$, while in [72] a value of $r_0/a = 7.29(4)$ is quoted.

In that sense our results concerning r_0T_c have to be taken with great care. Although our determination of r_0/a as described in section 4.2.4 yields nice scaling behaviour of the potential and excellent asymptotic scaling behaviour of r_0/a itself, this is rather a proof of our ability to consistently and systematically extract the scale for all simulations performed. For the use of r_0/a as a quantity to test and compare scaling violations in r_0T_c we need a more accurate determination of r_0/a as is accessible to us at the moment.

Nevertheless, we try to follow the procedure proposed in [62, 64] as close as possible. First we perform correlated fits of the correlation matrix elements to the form $Z(r) \exp\{-(V_0 + \alpha/r + \sigma r)t\}$ as described in section 4.2.4, but only locally, i.e. using data between some r_{\min} and r_{\max} close to r_c . Then the force is interpolated to arbitrary values of r from these local fits and finally r_c/a (and accordingly r_0/a) is determined from the relation (4.5). In order to estimate the systematic errors we calculate r_0/a from different small fit ranges and, correspondingly, different values of c from table 4.1. Then the results are combined with a weight depending on the error of the quantity¹¹. The final results for r_0/a are listed in table 4.9 where the first error denotes the statistical error. The second is the estimate of the systematic error and marks the minimal and maximal value of r_0/a obtained with different fit ranges and different reasonably chosen values of c . The systematic error stemming from different determinations of the potential values is not taken into account. For later reference we also determined r_0/a for $\beta = 3.40, 3.15$ and $\beta = 2.86$. In table 4.10 we collect the data for r_0T_c from our measurements with the FP action together with the data from measurements with the Wilson action for comparison. The critical couplings corresponding to $N_\tau = 4, 6, 8$ and 12 are taken from [49] while the values for r_0/a are from the interpolating formula in [64]. The quoted errors are purely statistical. The continuum value is our own extrapolation obtained by performing a fit linear in the leading correction term $1/N_\tau^2$. The data point at $N_\tau = 4$ was discarded from the fit. Finally, the values are plotted in figure 4.4 for comparison.

¹¹In addition one could also take into account the χ^2 -value of the corresponding fit as is done in [65].

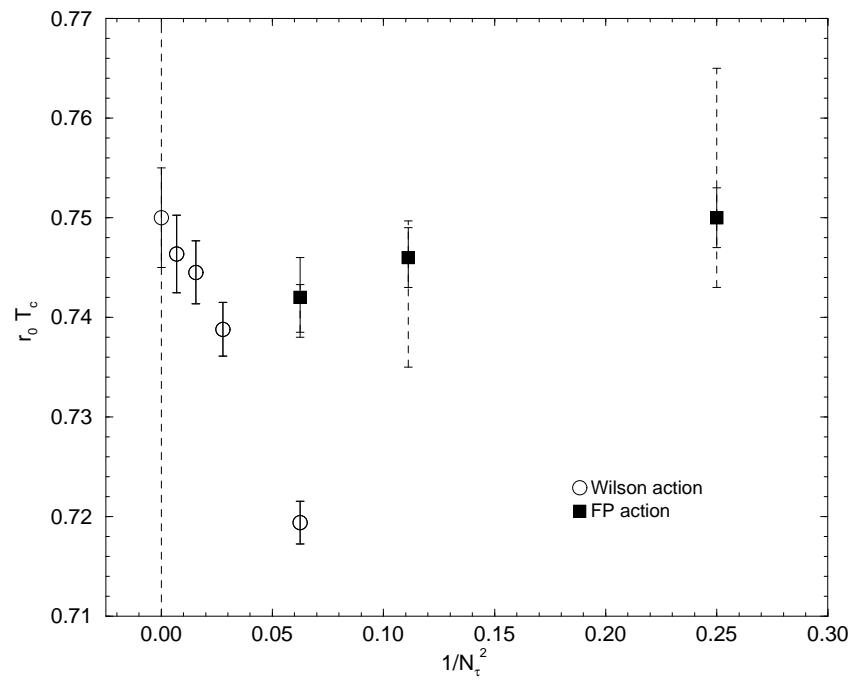


Figure 4.4: $r_0 T_c$ vs. $1/N_\tau^2$ for the Wilson and the FP action. The empty circles represent data from measurements with the Wilson action and the filled squares denote the results obtained with the FP action.

β	r_0/a
3.400	4.833(39) $^{(+18)}_{(-22)}$
3.150	3.717(23) $^{(+19)}_{(-50)}$
2.927	2.969(14) $^{(+5)}_{(-14)}$
2.860	2.740(10) $^{(+17)}_{(-31)}$
2.680	2.237(7) $^{(+11)}_{(-33)}$
2.361	1.500(5) $^{(+29)}_{(-14)}$

Table 4.9: The hadronic scale r_0/a determined from local fits to the potential. The first error denotes the statistical error and the second is the estimate of the systematic error. The results for $\beta = 3.40, 3.15$ and $\beta = 2.86$ are quoted for later reference.

N_τ	Wilson action	FP action
2		0.750(3)
3		0.746(3)
4	0.719(2)	0.742(4)
6	0.739(3)	
8	0.745(3)	
12	0.746(4)	
∞	0.750(5)	

Table 4.10: Results for the critical temperature in terms of the hadronic scale, r_0T_c , from measurements with the Wilson action and the FP action.

The Wilson action shows scaling violation for r_0T_c of about 4% at $N_\tau = 4$, while at $N_\tau = 6$ it is already smaller than about 1.5%. In that sense this quantity provides a high precision scaling test and thus a very accurate computation of the low-energy reference scale r_0/a on the 0.5% level is of crucial importance. The lack of data for different actions is an indication that this is indeed a difficult task. Although the required statistics is in principle accessible to us, we do not have full control over the systematic ambiguities in the calculation of r_0/a on the required accuracy level. Nevertheless we observe in principle excellent scaling within 1% or two standard deviations for the FP action even on coarse lattices corresponding to $N_\tau = 3$ and 2, however, this statement is moderated in view of the large systematic uncertainties. The systematic effects are generated by different methods of extracting the potential values, different procedures of interpolating and calculating the force, different choices of fit ranges etc.

One way around the caveat is to repeat the same measurements and exactly the same analysis independently for measurements with the Wilson action in order to rule out these systematic effects and to reliably detect and to compare scaling violations for both actions. In any case further studies on the determination of r_0/a are clearly necessary in order to fully gain control over all possible sources of systematic errors. Unfortunately this is beyond the scope of the present work.

4.3.3 $r_0\sqrt{\sigma}$

As a byproduct of the analysis in the previous two sections we can now look at another RG invariant product, namely $r_0\sqrt{\sigma}$. This quantity is not accessible from the global fits to the potential performed in section 4.2.4 since then $\sqrt{\sigma}a$ and r_0/a are determined from the same description or parametrization of the potential data and thus are strongly correlated. This is no longer the case after the previous analysis, where σ is determined from the long range properties of the potential while r_0 is calculated from local fits only where the precise form of the fitting ansatz is irrelevant.

In table 4.11 we have collected the resulting values of $r_0\sqrt{\sigma}$ when r_0/a is taken from table 4.9 and σa^2 from table 4.8. We also list the results from the potential measurements at the three additional β -values $\beta = 2.86, 3.15$ and 3.40 . We can extrapolate to the continuum either by performing a fit linear in $(a/r_0)^2$ or by fitting a constant in order to obtain $r_0\sqrt{\sigma} = 1.193(10)$ and $r_0\sqrt{\sigma} = 1.193(6)$, respectively. For comparison we calculated the data for the Wilson action from the interpolating formula for r_0/a in [64] and the string tension parametrization in [65]. The continuum extrapolation for the Wilson data is from the analysis of Teper in [70].

β	$r_0\sqrt{\sigma}$
FP action	
2.361	1.194(21)
2.680	1.196(15)
2.860	1.190(23)
2.927	1.191(12)
3.150	1.185(16)
3.400	1.198(12)
∞	1.193(10)
Wilson action	
5.6925	1.148(12)
5.8941	1.170(19)
6.0624	1.183(13)
6.3380	1.185(11)
∞	1.197(11)

Table 4.11: $r_0\sqrt{\sigma}$ for the Wilson and the FP action.

Figure 4.5 shows the scaling behaviour of $r_0\sqrt{\sigma}$ for the Wilson action (empty circles) and the FP action (filled squares) as a function of $(a/r_0)^2$. The error bars are purely statistical and are dominated by the uncertainty from the string tension. Therefore the systematic ambiguities possibly present in r_0/a are not visible within the shown error bars.

The Wilson action shows a scaling violation of about 4% at $\beta = 5.6925(N_\tau = 4)$, while no scaling violation is seen for the FP action even on lattices as coarse as $\beta = 2.361(N_\tau = 2)$. We would like to emphasize again that this is a non-trivial result, since r_0/a and $\sqrt{\sigma}a$ are determined completely independent of each other. However, with the data presently available to us it is difficult to extract the string tension with the accuracy needed to see a striking difference

to the Wilson action for β -values corresponding to $N_\tau \geq 4$. This is mainly due to the lack of measurements of the off-diagonal potential values.

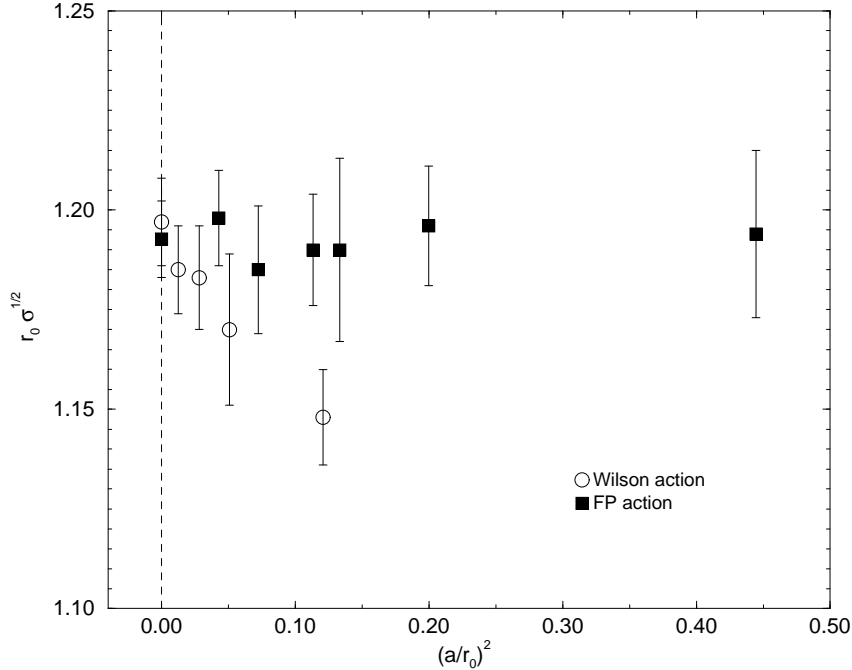


Figure 4.5: Scaling behaviour of $r_0\sqrt{\sigma}$ for the Wilson action (empty circles) and the FP action (filled squares). The scale on the x-axis is chosen for convenience.

4.4 Conclusions and outlook

In this chapter the parametrized FP action was subjected to several scaling tests. By means of the static quark-antiquark potential and the scaling of $r_0 T_c$, $T_c/\sqrt{\sigma}$ and $r_0\sqrt{\sigma}$ we have assured that the action behaves well and shows no irregularities over the whole range of studied lattice spacings. In all quantities under investigation we observe excellent scaling within the standard errors or 2 % even on lattices as coarse as $a \simeq 0.2 - 0.3$ fm.

One important outcome of the studies in this chapter is, that the hadronic scale r_0/a introduced by Sommer [62] and pursued by [64] is not appropriate for lattice spacings larger than around $a \simeq 0.1$ fm. The intention of the authors to have a new way of setting the scale in a consistent way without introducing additional lattice artifacts is certainly appreciable. However, the scale incorporates large systematic ambiguities depending heavily on the techniques used for extracting it. This makes it nearly impossible to compare the results of different groups reliably using r_0/a at lattices spacings around $a \simeq 0.1$ fm. In this regime it seems more preferable to use the effective string tension σ to set the scale.

Regarding our calculations it would be desirable to measure the effective string tension using off-axis potentials in the future. As was already pointed out,

this would allow a more reliable determination of the physical scale, especially on coarse lattices. In addition, one could determine the potential gap Δ along the lines in [64] and check the scaling behaviour of $r_0\Delta|_{r_0}$. This quantity shows lattice artifacts as large as 20% at $\beta_W = 5.8$ and 12% at $\beta_W = 5.95$.

Chapter 5

Glueballs

5.1 Introduction

The rich structure in the hadron spectrum of QCD is expected to reveal bound states consisting of (mainly) gluons, so called glueballs. Unfortunately, calculating the properties of such states directly from first principles using the QCD lagrangian proves to be a difficult task and standard perturbative methods fail. One possibility is provided by numerical computations using lattice QCD and, indeed, glueball masses were among the first quantities to be calculated on the lattice. Most of these calculations have been done in the quenched approximation¹, mainly because glueballs are the actual excitations in the pure gauge sector. There also exist studies of effects from dynamical sea quarks and glueball-meson mixing on the glueball spectrum from the SESAM and T χ L collaborations [72, 74, 75] and from the UKQCD collaboration [76], however, the results are not yet conclusive [75].

On the experimental side there is some evidence found in several experiments for the existence of exotic glueballs or hybrid particles consisting of quarks with gluonic excitations. The exotic glueballs, sometimes called "oddballs", have exotic quantum numbers, e.g. $0^{+-}, 1^{-+}$, and are particularly interesting in lattice gauge theory because they can not mix with conventional meson states. Per contra, the glueballs with the lowest masses have conventional quantum numbers. They are sitting in a dense background of conventional meson states and it is thence difficult to distinguish them in an experiment. For further details on the experimental aspect of the glueball spectrum and possible glueball candidates we refer to a recent article [77] reviewing the light meson spectrum.

The main obstacle in the computations of glueball masses on the lattice is the fast decay of the signal in the correlation functions of the gluonic excitations, due to the fact that the glueball masses are relatively large ($m_G \geq 1.6$ GeV). It turns out to be notoriously difficult to extract the glueball masses before the signal disappears in the relatively large noise of the measured correlation functions and thus a small lattice spacing a is required to follow the signal long enough. On the other hand, the physical lattice volume should be larger than $L \geq 1.2$

¹For comprehensive reviews of such calculations see [70] and [73].

fm to avoid finite size effects. This finally results in a large L/a making it hard to obtain the statistics which is usually required. One possible way around the caveat is the use of anisotropic lattice actions which have a finer resolution in time direction, $a_\tau \ll a_\sigma$, and thence allow to follow the signal over a larger range of time slices. Although this idea is not new [78], it has been revived only recently by Morningstar and Peardon [79, 80]. Using an anisotropic improved lattice action they investigated the glueball spectrum below 4 GeV in the pure SU(3) gauge theory and improved the determinations of the glueball masses considerably compared to previous Wilson action calculations. Recent Wilson action calculations comprehend works by the UKQCD collaboration [81] and the GF11 group [82, 83]. It can be said that all three calculations are in reasonable agreement on the masses of the two lowest lying 0^{++} and 2^{++} glueballs.

Despite this agreement Wilson action calculations of the 0^{++} glueball mass, however, show huge lattice artifacts of around 40 % at coarse lattice spacings $a \simeq 0.15$ fm and still 20 % even at modest lattice spacings $a \simeq 0.10$ fm. From this point of view the 0^{++} glueball mass is particularly interesting, besides its physical relevance, since it provides an excellent test object on which the scaling behavior of different actions can be checked and the achieved reduction of discretization errors can be sized. In this sense let us emphasize that our intention here is twofold: firstly, our calculation provides a new and independent determination of glueball masses using FP actions, and secondly, we aim at using the glueball spectrum, in particular the mass of the 0^{++} glueball, as another scaling test of the FP action. Although we observe that the FP action scales well in quantities like $r_0 T_c$, $T_c/\sqrt{\sigma}$ or $r_0\sqrt{\sigma}$, lattice artifacts could be, in principle, quite different in other physical quantities, in particular $r_0 m_G$ or $m_G/\sqrt{\sigma}$.

A systematic determination of the glueball spectrum is of course much more involved. For example it requires a careful differentiation of the single glueball state from two-gluon and torelon-pair states having zero total momentum. The latter can rather easily be identified through a finite size scaling study, since the torelon mass is strongly dependent on the lattice volume. In addition, such a study is needed to measure the systematic effects inherited in the results from finite volume. Finally, after performing the continuum extrapolation one has to reliably identify the continuum spin content of each energy level. Such a systematic study is of course beyond the scope of the present work.

This chapter is organized as follows. In section 5.2 we first describe the construction of glueball operators from Wilson loops. This involves some group theory and provides a nice and pedagogical application of representation theory. In section 5.3 we describe the details of the simulations including the generation of the gauge field configurations and the measurements of the operators. The extraction of masses from the Monte Carlo estimates of glueball correlation functions are presented in section 5.4 together with a discussion of the scaling. Finally, the main results are summarized in section 5.5.

5.2 Glueball operators from Wilson loops

In this section we describe the construction of the operators measured in the glueball simulations. We first review the characterization of glueball states ac-

cording to their transformation properties under irreducible representations of the rotation group following closely [84] and [85]. Then we present the construction of basis functions of irreducible representations in general and later specify to operators transforming under the cubic group O_h . Some properties of the cubic point group are summarized in appendix E.

5.2.1 Glueball states

Physical states in the Hilbert space of lattice gauge theory are gauge invariant and they can be obtained by applying gauge invariant operators to the pure gauge vacuum. Of particular interest in our simulations are space-like Wilson loops in the fundamental representation of $SU(3)$. Since we are aiming for the determination of masses of glueball states, we are only considering zero-momentum states, i.e. translationally-invariant operators.

In the continuum limit the Hamiltonian is rotationally invariant and its eigenstates can be characterized according to the unitary representations of the group $SU(2)$ in general, and to those of the three-dimensional rotation group $SO(3)$ for bosonic states in particular. In addition the Hamiltonian is invariant under parity and charge conjugation, and therefore the states can further be classified according to having eigenvalues $P = \pm 1$ under parity and $C = \pm 1$ under charge-conjugation parity, respectively. Thus we may label the eigenstates of the Hamiltonian corresponding to glueball states with definite mass by $|\psi\rangle = |J^{PC}\rangle$, where J denotes the spin of the corresponding irreducible representation D_J of the rotation group.

For finite values of β we work on a hypercubic lattice and continuous rotation symmetry is broken down to exact cubic symmetry. On the lattice the role of the Hamiltonian is adopted by the transfer matrix. Thence we are now considering eigenstates of the transfer matrix, which belong to an irreducible representation of the cubic group O . Since the cubic group is a subgroup of $SO(3)$, any representation D_J induces a representation on the group O , the so-called subduced representation D_J^O . In general, the subduced representation is no longer irreducible and can thus be decomposed into the irreducible representations Γ^p of the cubic group O ,

$$D_J^O = \Gamma^1 \oplus \Gamma^2 \oplus \dots \quad (5.1)$$

In table 5.1 we list for convenience the subduced representations of the rotation group up to $J = 6$. The labeling of the irreducible representations of the cubic group follows the standard notation, where one-dimensional representations are denoted by A , two-dimensional irreducible representations by E and three-dimensional irreducible representations by T .

As a consequence of this decomposition the quintuplet of degenerate states of a spin $J = 2$ particle in the continuum for example will be split up by the lattice regularization into a doublet and a triplet transforming under E and T_2 , respectively. The mass splitting between the two representations will disappear as we approach the continuum limit and full rotation symmetry is restored. On the other hand, every state in the lattice theory transforming according to an irreducible representation Γ^p of the cubic group can be expanded in the continuum limit into eigenstates of spin J ,

$$|\Gamma^p\rangle = \sum_J c_J^{\Gamma^p} |J\rangle. \quad (5.2)$$

Γ^p	$J = 0$	1	2	3	4	5	6
A_1	1	0	0	0	1	0	1
A_2	0	0	0	1	0	0	1
E	0	0	1	0	1	1	1
T_1	0	1	0	1	1	2	1
T_2	0	0	1	1	1	1	2

Table 5.1: Subduced representations of the rotation group up to $J = 6$. Given are the multiplicities with which the representation Γ^p can be found in the subduced representation D_J^O . The labeling of the irreducible representations is explained in the text.

However, spin J can contribute to this superposition only if Γ^p is contained in D_J^O . Usually, the lowest spin contained in Γ^p belongs to the lowest mass. Nevertheless, a unique identification of glueball states on the lattice with continuum spin states is possible only sufficiently close to the continuum limit when different representations in a given column of table 5.1 become (nearly) degenerate.

5.2.2 Construction of basis functions of irreducible representations

In this section we describe the general procedure for constructing basis functions of irreducible representations. This involves the character projection operator defined by

$$\mathcal{P}^p = \frac{d_p}{g} \sum_{T \in \mathcal{G}} \chi^p(T)^* P(T), \quad (5.3)$$

where p labels the irreducible representations Γ^p of dimension d_p of a finite group of coordinate transformations \mathcal{G} of order g , $\chi^p(T)$ being the character of $T \in \mathcal{G}$ in Γ^p and $P(T)$ the unitary operator in the Hilbert space L^2 of the coordinate transformation $T \in \mathcal{G}$.

\mathcal{P}^p has the property of projecting out of a function $\phi \in L^2$ the sum of all the parts transforming under Γ^p . Having chosen a (normalizable) ϕ such that $\mathcal{P}^p \phi$ is not identically zero, we construct $P(T)(\mathcal{P}^p \phi)$ for each $T \in \mathcal{G}$. Each of these are linear combinations of the d_p basis functions of Γ_p . From these functions we abstract d_p linearly independent functions and apply the Gram-Schmidt orthogonalization to obtain a set of orthonormal basis functions of the irreducible representation.

In practice, given a non-zero $\mathcal{P}^p \phi$, we construct $\sum_i P(T_i)(\mathcal{P}^p \phi)$, where $\sum_i P(T_i)$ is an appropriately chosen linear combination of the unitary coordinate transformation operators. Then from this first basis function all others are generated by applying appropriate rotation operators². This procedure ensures that each set of basis functions obtained from different functions $\phi_i \in L^2$ transform exactly in the same way under a given irreducible representation Γ^p .

²For details see section E.3 in the appendix.

5.2.3 Irreducible representations of the cubic group on Wilson loops

In this section we construct the irreducible representations of the cubic group O_h on space-like Wilson loops up to length eight. To make the connection to the construction presented before, let us note that the Wilson loops acting on the vacuum state take over the role of the function ϕ in the Hilbert space L^2 as introduced in the previous section³.

All prototypes of Wilson loop shapes up to length eight are displayed in figure 5.1. Each of these shapes is characterized by an L -tuple describing the path of the corresponding loop,

$$(\hat{f}_1, \dots, \hat{f}_L) \quad \text{with} \quad \sum_{i=1}^L \hat{f}_i = 0, \quad (5.4)$$

where the \hat{f}_i are unit vectors corresponding to the space-like coordinates. By $[\hat{f}_1, \dots, \hat{f}_L]$ we denote the equivalence class of L -tuples which are identical up to cyclic permutations. Under C -parity we simply have

$$C[\hat{f}_1, \dots, \hat{f}_L] = [-\hat{f}_L, -\hat{f}_{L-1}, \dots, -\hat{f}_1], \quad (5.5)$$

and the combinations

$$[\hat{f}_1, \dots, \hat{f}_L]_{\pm} = [\hat{f}_1, \dots, \hat{f}_L] \pm [-\hat{f}_L, \dots, -\hat{f}_1] \quad (5.6)$$

are even and odd under the C -parity transformation, respectively. This corresponds to taking the real or the imaginary part of the Wilson loop under consideration.

A (reducible) representation \mathcal{M} of O_h on operators of a given fixed shape is now defined through

$$\mathcal{M}_g[\hat{f}_1, \dots, \hat{f}_L]_{\pm} \doteq [M_g \hat{f}_1, \dots, M_g \hat{f}_L]_{\pm}, \quad \forall g \in O_h, \quad (5.7)$$

where M_g is the matrix corresponding to the group element g in the fundamental representation. The representation \mathcal{M} has dimension d , where d is the number of different spatial orientations of the given shape. In table 5.2 we have listed the dimensions of the generated representations including C -parity on every loop shape.

loop shape #	1	2	3	4	5	6	7	8	9	10	11
dimension d	6	12	24	8	6	24	24	96	48	12	48
loop shape #	12	13	14	15	16	17	18	19	20	21	22
dimension d	24	12	24	6	12	12	48	12	48	24	96

Table 5.2: Dimension d of the representation of $O_h \times C$ on the loop shapes, i.e. the number of different orientations.

³In particular we have $\phi[U] = W[U]\phi_{\text{vac}}[U]$, where $W[U]$ is a Wilson loop built from gauge links U and $\phi_{\text{vac}}[U]$ is the vacuum state invariant under applications of the transfer matrix. The symmetry properties of $\phi[U]$ are then characterized by those of the Wilson loops $W[U]$.

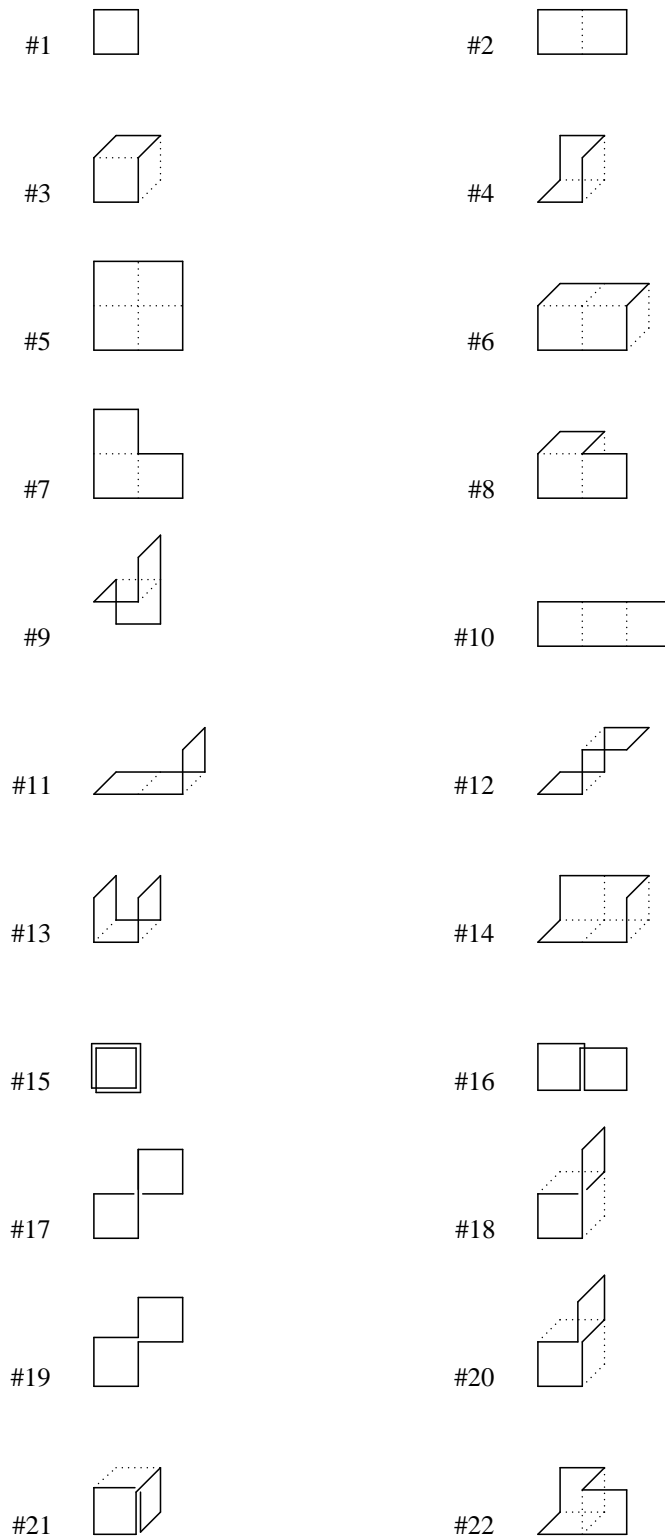


Figure 5.1: Prototypes of space-like Wilson loop shapes up to length 8.

The irreducible contents of the representation \mathcal{M} are determined by means of the character relation (E.5). In practice we first construct a matrix representative in each conjugacy class \mathcal{C} for every representation \mathcal{M} with fixed C -parity and from this its character $\chi(\mathcal{C})$ in this representation by taking the trace. The multiplicity n_P of the irreducible representation Γ^p in $\Gamma = \mathcal{M}$ are then calculated by

$$n_p = \frac{1}{48} \sum_{\mathcal{C}} n_{\mathcal{C}} \chi(\mathcal{C}) \chi^p(\mathcal{C}), \quad (5.8)$$

where $\chi^p(\mathcal{C})$ can be read from table E.2 and $n_{\mathcal{C}}$ is the number of elements in the conjugacy class \mathcal{C} . The results are listed in table 5.3 and 5.4.

shape	A_1^{++}	A_2^{++}	E^{++}	T_1^{++}	T_2^{++}	A_1^{-+}	A_2^{-+}	E^{-+}	T_1^{-+}	T_2^{-+}
#1	1	0	1	0	0	0	0	0	0	0
#2	1	1	2	0	0	0	0	0	0	0
#3	1	0	1	0	1	0	0	0	1	1
#4	1	0	0	0	1	0	0	0	0	0
#5	1	0	1	0	0	0	0	0	0	0
#6	1	0	1	0	1	0	0	0	1	1
#7	1	0	1	0	1	0	0	0	1	1
#8	1	1	2	3	3	1	1	2	3	3
#9	1	0	1	1	2	1	0	1	1	2
#10	1	1	2	0	0	0	0	0	0	0
#11	1	1	2	1	1	0	0	0	2	2
#12	1	1	2	1	1	0	0	0	0	0
#13	1	0	1	0	0	0	0	0	0	1
#14	1	0	1	1	2	0	0	0	0	0
#15	1	0	1	0	0	0	0	0	0	0
#16	1	1	2	0	0	0	0	0	0	0
#17	1	0	1	0	1	0	0	0	0	0
#18	1	0	1	1	2	1	0	1	1	2
#19	1	0	1	0	1	0	0	0	0	0
#20	1	0	1	1	2	1	0	1	1	2
#21	1	0	1	0	1	0	0	0	1	1
#22	1	1	2	3	3	1	1	2	3	3

Table 5.3: Irreducible contents of the C -parity plus representations of the symmetry group of the cube on Wilson loops up to length eight.

The orthogonal wave functions of the irreducible operators which can be built from Wilson loops up to length eight are listed in appendix E.3 in the tables on page 107 – 113. Note that the expressions for loop shape #8, 9, 11, 18, 20 and 22 are too lengthy and can thus not be displayed.

shape	A_1^{+-}	A_2^{+-}	E^{+-}	T_1^{+-}	T_2^{+-}	A_1^{--}	A_2^{--}	E^{--}	T_1^{--}	T_2^{--}
#1	0	0	0	1	0	0	0	0	0	0
#2	0	0	0	1	1	0	0	0	0	0
#3	0	0	0	1	1	1	0	1	0	1
#4	0	1	0	1	0	0	0	0	0	0
#5	0	0	0	1	0	0	0	0	0	0
#6	0	0	0	1	1	1	0	1	0	1
#7	0	1	1	1	0	0	0	0	1	1
#8	1	1	2	3	3	1	1	2	3	3
#9	0	1	1	2	1	0	1	1	2	1
#10	0	0	0	1	1	0	0	0	0	0
#11	0	0	0	2	2	1	1	2	1	1
#12	0	0	0	2	2	0	0	0	0	0
#13	0	0	0	1	0	0	1	1	0	0
#14	0	1	1	2	1	0	0	0	0	0
#15	0	0	0	1	0	0	0	0	0	0
#16	0	0	0	0	0	0	0	0	1	1
#17	0	0	0	0	0	0	0	0	1	1
#18	0	1	1	2	1	0	1	1	2	1
#19	0	1	1	1	0	0	0	0	0	0
#20	1	0	1	1	2	1	0	1	1	2
#21	0	0	0	1	1	0	1	1	1	0
#22	1	1	2	3	3	1	1	2	3	3

Table 5.4: Irreducible contents of the C -parity minus representations of the symmetry group of the cube on Wilson loops up to length eight.

5.3 Simulation details

We performed simulations at three different lattice spacings in the range $0.1 \text{ fm} \leq a \leq 0.18 \text{ fm}$ and volumes between 1.4 fm and 1.8 fm. The simulation parameters for the different runs are given in table 5.5, where we list the values of the couplings, the lattice sizes and the relevant numbers for the obtained statistics. We also give our estimates of the hadronic scale r_0/a and the corresponding approximate lattice spacings in units of fermi for convenience.

β	lattice	$a[\text{fm}]$	r_0/a	# bins	bin size	meas./bin
3.40	14^4	0.10	4.833(39)	206	420	70
3.40	14^4	0.10	4.833(39)	152	200	50
3.15	12^4	0.13	3.717(23)	202	500	50
2.86	10^4	0.18	2.740(10)	160	200	50

Table 5.5: Run parameters of the glueball simulations. Values for the coupling β , the lattice size and the obtained statistics are listed. The estimate of the hadronic scale r_0 in terms of the lattice spacing a is given as well as the approximate lattice spacing in units of Fermi.

The gauge field configurations were updated by performing a compound sweep consisting of one over-relaxation sweep and one standard Metropolis sweep.

We first performed two "small" preliminary simulations at $\beta = 3.40$ and $\beta = 2.86$. After each compound sweep we measured five different loop shapes, #6, 8, 11, 14, 22, on five smearing levels $\mathcal{S}_n, n = 2, 4, \dots, 10$ with smearing parameter⁴ $\lambda_s = 0.2$ and subsequently projected into the A_1^{++} -channel.

In the two large simulations we measured all 22 Wilson loop shapes on the same smearing levels as before ($\mathcal{S}_n, n = 2, 4, \dots, 10; \lambda_s = 0.2$) and projected them into all 20 irreducible glueball channels. Measurements were taken after three and five compound sweeps at $\beta = 3.40$ and $\beta = 3.15$, respectively.

The projections of the loop shapes into the different channels were done according to the description in section 5.2. Then the correlator matrix elements were constructed from the projected operators and Monte Carlo estimates were obtained by averaging the measurements in each bin. During a simulation run we measure all possible 'polarizations' in a given channel and collect them together on the level of the correlation matrix. This will eventually suppress the statistical noise by a factor of the dimension of the representation, if the different polarizations are anti-correlated. Finally, the resulting large correlation matrices from each bin were stored for later analysis. Of course the smearing and in particular the measurements of the loops takes a considerable part of the simulation time and can in principle be reduced by considering only a small number of shapes. On the other hand one is interested in having as large as possible the set of operators for constructing the wave function of the ground state. In addition, having measured all loop shapes up to length eight in the two larger simulations allows us to identify the important loop shapes for future simulations. However, only a moderate amount of work has been devoted to this kind of analysis up to now, cf. section 5.4.2.

⁴For details of the smearing we refer to section 4.2.3.

For the extraction of the glueball masses one has to consider vacuum-subtracted operators. For this purpose we also measured and stored the expectation values of all the operators in each bin. Vacuum subtraction is required only in the A_1^{++} -channel since it has the same quantum numbers as the vacuum. All other channels have a vanishing vacuum expectation value, thereby yielding a check for the correct construction of operators in each of the channels. We investigated different methods of removing the vacuum expectation value and, finally, followed a strategy which is outlined in the next section amongst other details of the analysis.

5.4 Analysis details

In the final analysis phase for extracting the glueball masses we resort to the variational techniques described in section D.1 and D.2. Although the procedure is straightforward in general, let us put some remarks which are related to the analysis of the glueball masses in particular.

In a given symmetry channel we have to find a linear combination of the basic operators which overlaps best with the wave function of the ground state and, if necessary, of the next few excited states. This can be achieved by choosing the linear combination which minimizes the effective mass on a given time slice at t_0 and amounts to solving the generalized eigenvalue equation

$$C(t_1)v = e^{-E(t_1-t_0)}C(t_0)v. \quad (5.9)$$

This, however, requires a positive definite $C(t_0)$, which in general is not fulfilled for $t_0 \geq 1$ due to statistical errors. In particular the large number of operators measured in the glueball simulations yield a few very small or even slightly negative eigenvalues of $C(t_0)$ with large relative errors. This is due to the fact that some of the operators are strongly correlated and therefore not linearly independent on the given MC sample, but can be avoided by first diagonalizing and then projecting and truncating $C(t_0)$ to an appropriate subspace of operators as described in section D.1. However, the large statistical noise in some of the operators can even spoil the diagonalization of $C(t_0)$ in such a way that remnants of the unphysical modes are still present even after the truncation to a smaller operator basis.

Therefore we choose right from the beginning a set of operators which we consider to be well measured (cf. section 5.4.2). On this set the whole procedure is numerically stable and well defined. Nevertheless, the choice of operators is arbitrary to some extent and an optimized choice will presumably improve the stability of the analysis. It would be most interesting and rather easy to investigate for example the overlap of each of the operators with the ground state. First steps in this direction are already undertaken, but it requires further work.

Another remark concerns the vacuum subtraction necessary in the A_1^{++} -channel. To obtain vacuum-subtracted operators one usually considers $\phi^{\text{sub}}(\tau) = \phi(\tau) - \langle 0|\phi(\tau)|0\rangle$. However, we follow a different strategy and treat the vacuum as an additional state carrying zero energy. As it turns out the vacuum state can be determined with very high accuracy and it is safe to consider only the operator basis orthogonal to the vacuum in the fitting procedure. For

this purpose we cut out the vacuum state obtained from solving the generalized eigenvalue equation (5.9), i.e. we only consider the correlation matrix⁵

$$C_{ij}^K(t) = (v_i, C^M(t)v_j), \quad (5.10)$$

with i, j running from $i, j = 2, \dots, K \leq M$ in the further analysis. In our experience this strategy yields the most stable subtraction of the vacuum contribution with respect to the statistical fluctuations of the subtracted operators.

In the last step for extracting the glueball masses the large correlation matrices are truncated down to a 1×1 or 2×2 matrix which is subsequently fitted in the fit range $t_{\min} \dots t_{\max}$ taking both temporal correlations and correlations among the operators into account. The choice of t_{\max} is not crucial and is usually taken according to the relative error of the matrix elements under consideration and the χ^2 -function. More important is the correct choice of t_{\min} . Since excited glueball masses are rather high we do not expect large contamination of the ground state correlators from excited states even on time slice $t = 1$ and therefore $t_{\min} = 1$ was usually chosen. In particular this choice is safe if we fix $t_0 = 1$ and $t_1 = 2$ rather than $t_0 = 0$ and $t_1 = 1$. Indeed, in the former case the χ^2 -function remains more stable when we increase $t_{\min} = 1$ to $t_{\min} = 2$ as a check for the consistency in the extracted values for the masses. As an example take the results in table F.6 for the A_1^{++} -channel at $\beta = 2.86$, where we observe a large shift in the fitted mass for the choice $t_0 = 0$ and $t_1 = 1$ while no change is seen for the choice $t_0 = 1$ and $t_1 = 2$ when t_{\min} is increased from 1 to 2.

One remark is in order concerning the mass estimate in the A_1^{++} -channel of the $\beta = 3.15$ simulation. There we observe a systematic difference of the mass estimate depending on whether $t_{\min} = 1$ or 2 and lying significantly outside the statistical error of the usually chosen $t_{\min} = 1$ value. In order to take this systematic shift into account we calculate an average of the two highlighted values in table F.5 taking their errors as a measure of the weight. To be on the safe side the final error is just the simple average of the two errors and covers both significantly different values within one standard deviation.

5.4.1 Results

The results of the fits to the glueball correlators are collected in the appendix in tables F.3 – F.6 where we list the values of t_0 and t_1 , the number of operators, N_{op} , kept after the truncation in $C(t_0)$, the fit range $t_{\min} \dots t_{\max}$, the χ^2 per degree of freedom, χ^2/N_{DF} , and the mass estimate. All temporal correlations and correlations among the operators are taken into account by performing correlated fits as described in section D.2. The covariance matrix is calculated from Jackknife samples and the error is estimated using a Jackknife procedure. We include the results of different fits in the tables in order to give an impression on the stability of the fits. In each channel the result highlighted in boldface is our final choice and represents a most reasonable mass estimate for the given channel. These final mass estimates are collected in table 5.6 for convenience.

To compare these values it is convenient to use r_0 to set the scale. In table 5.7 we list our estimates of the glueball masses expressed in terms of r_0 , while figure 5.2 and 5.3 show our values for the A_1^{+-} - and the E^{++}, T_2^{++} -channel, respectively, together with results from different calculations with the Wilson

⁵See section D.1 for notations.

	$\beta = 2.86$	$\beta = 3.15$	$\beta = 3.40$	$\beta = 3.40$
A_1^{++}	1.411(96)	1.054(56)	0.831(33)	0.836(23)
E^{++}		1.534(62)		1.233(48)
T_2^{++}		1.609(55)		1.234(28)
A_1^{-+}		1.65(18)		1.395(86)
E^{-+}		1.97(20)		1.681(72)
T_2^{-+}		1.92(11)		1.631(72)
T_1^{+-}		2.10(18)		1.64(16)

Table 5.6: Final glueball mass estimates in terms of the lattice spacing, $a m_G$.

action (crosses) and the calculation of Morningstar and Peardon with a tree level/tadpole improved anisotropic action (empty circles).

	J	$\beta = 2.86$	$\beta = 3.15$	$\beta = 3.40$	$\beta = 3.40$
A_1^{++}	0	3.87(27)	3.92(23)	4.02(16)	4.04(12)
E^{++}	2		5.70(23)		5.96(24)
T_2^{++}	2		5.98(21)		5.96(14)
A_1^{-+}	0		6.13(67)		6.74(42)
E^{-+}	2		7.32(74)		8.12(35)
T_2^{-+}	2		7.14(41)		7.88(35)
T_1^{+-}	1		7.81(67)		7.93(78)

Table 5.7: Final glueball mass estimates in terms of r_0 , $r_0 m_G$. The continuum spin interpretation of each channel is given for convenience.

It is interesting to compare our results with the continuum values from various collaborations. For this purpose we resort to [86] where the results of refs. [70, 81, 83] have been expressed or converted in units of r_0 using the interpolating formula for the Wilson action [64] and, whenever necessary, the continuum extrapolation has been redone. The final results are listed in table 5.8. Our continuum result is an extrapolation to the continuum using a fit function linear in $(a/r_0)^2$, which amounts to

$$r_0 m_{0^{++}} = 4.12(21) - (2.1 \pm 3.1) \left(\frac{a}{r_0} \right)^2. \quad (5.11)$$

The χ^2 per degree of freedom of the fit is $\chi^2/N_{\text{DF}} = 0.07$. The data in the other channels is too little to be extrapolated to the continuum and we simply quote the masses obtained on the finest lattice ($a = 0.10$ fm) in brackets. It is interesting to compare our results with the continuum values from the other groups listed in table 5.9. Note in particular our values for the degenerate 2^{++} state, E^{++} and T_2^{++} , which agree very well with the continuum values of other groups. We observe restoration of the degeneracy in the 2^{++} and 2^{-+} channel within the statistical errors.

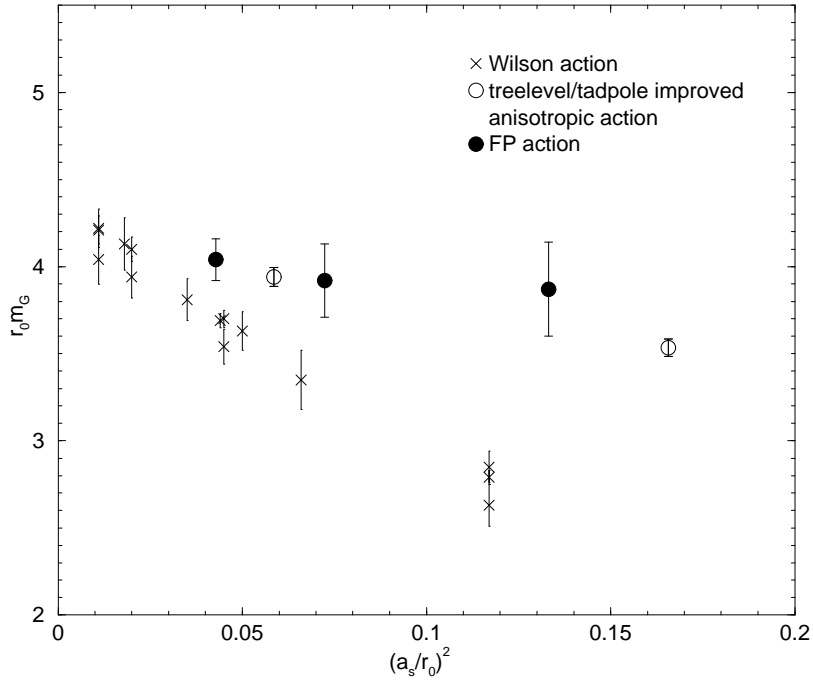


Figure 5.2: Glueball mass estimates for the A_1^{++} channel. Results from simulations of the Wilson action (crosses) and a tree level/tadpole improved anisotropic action (empty circles) are shown together with the results obtained with the FP action (filled circles).

Collab.	$r_0 m_{0^{++}}$	$r_0 m_{2^{++}}$	year
M&P [80]	4.21(11) (4)	5.85(2) (6)	1999
GF11 [83]	4.33(10)	6.04(18)	1999
Teper [70]	4.35(11)	6.18(21)	1998
UKQCD [81]	4.05(16)	5.84(18)	1993
FP action	4.12(21)	[5.96(24)]	2000

Table 5.8: Comparison of the two lowest glueball masses in units of r_0 . The 2^{++} value is not extrapolated to the continuum but denotes the mass obtained at a lattice spacing $a = 0.10$ fm.

Collab.	$r_0 m_{0^{-+}}$	$r_0 m_{2^{-+}}$	$r_0 m_{1^{-+}}$	year
M&P [80]	6.33(7) (6)	7.55(3) (8)	7.18(4) (7)	1999
Teper [70]	5.94(68)	8.42(78)	7.84(62)	1998
FP action	[6.74(42)]	[8.00(35)]	[7.93(78)]	2000

Table 5.9: Comparison of glueball masses in units of r_0 . Values in brackets denote masses obtained at a lattice spacing $a = 0.10$ fm and are not extrapolated to the continuum.

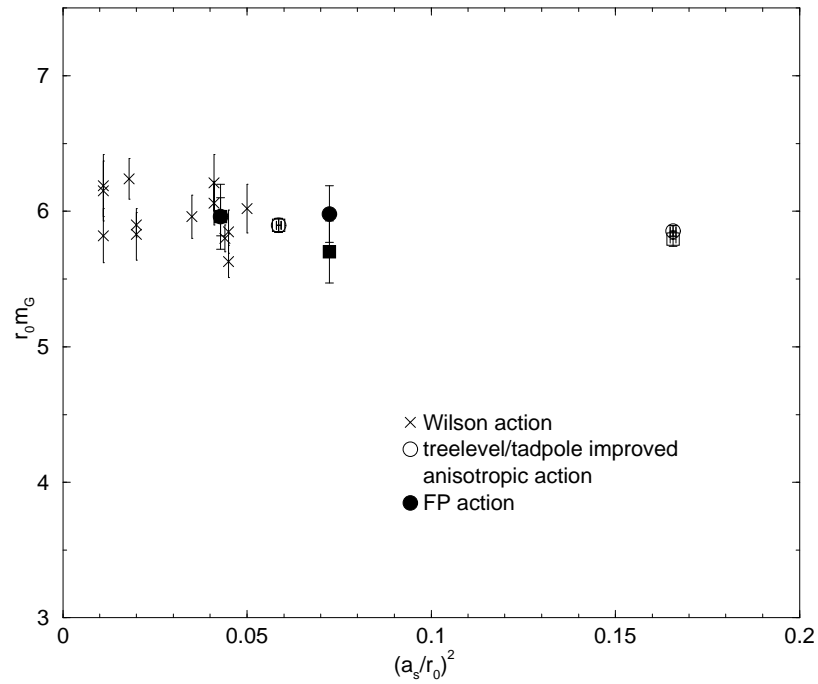


Figure 5.3: Glueball mass estimates for the 2^{++} channel. Results from simulations of the Wilson action (crosses) and a tadpole and tree level improved anisotropic action (empty symbols) are shown together with the results obtained with the FP action (filled symbols). Squares and circles denote the E^{++} and T_2^{++} mass estimates, respectively.

5.4.2 Signal/noise ratio of the operators

As already mentioned before it is interesting and even necessary to analyze which operators are well measured in a simulation and which operators have a large contribution to a given glueball state and thus have a large overlap with the corresponding wave function. This can give some hints about the size of the glueballs and might be helpful for the choice of operators and smearing schemes in future simulations. It is for this reason that we make statements even if we can only give a tendency for the preference of some smearing schemes.

Here we only report on our findings of what the signal/noise ratio of the operators concerns. The analysis of the overlap of each operator with the ground state has not yet systematically been done.

In each channel we analyzed the signal of the operators at $\beta = 3.40$ by looking at the decay in time of the diagonal correlators. As a measure of the quality of an operator we take the relative error of the corresponding signal. "Good" operators have a signal which can be followed over three time slices with an accuracy of around ten percent or even four time slices when accepting an error less than 50 percent. "Bad" operators can be measured accurately enough (on the ten percent level) only on time slice $\tau = 0$ and 1, while already $\tau = 2$ is lost in the noise completely. Including such operators in the analysis can be dangerous, because they may spoil the solution of the generalized eigenvalue problem when solved on $t_0 = 1, t_1 = 2$, yielding an unphysical guess for the wave functions, or they may even introduce errors already when truncating the correlation matrices down to a stable subspace of $C(t_0 = 1)$.

Of course the above classification is not clearcut but rather depends on how the operators behave compared to others in the same channel, simply meaning that we sometimes accept operators on an accuracy level which would be reason enough for rejecting them in other channels.

In this sense the following results of the analysis should only be understood as a rough guide, and one has to keep in mind that the preferred operators and smearing schemes may depend on the considered lattice spacing.

In the A_1^{++} -channel we could well measure all 22 loop shapes on smearing schemes 3, 4 and 5 except loop shape #16 and 17, which could not be measured with comparable accuracy.

The A_2^{++} -channel could not be measured at this lattice spacings, however, operators on low smearing levels seem to have a larger signal and smaller relative error. Nevertheless, the results indicate that shape #16, 1, 12 and 11 are the most problematic to measure (in the given order).

The E^{++} -channel seems to prefer smearing schemes 3, 4 and 5 at the considered lattice spacings, however the shapes #1, 9, 16, 17 and the second projection of #2, 10 and 22 could not be well measured even there.

In the T_1^{++} -channel the signal was again too weak to yield any reliable result, but clearly the first projection of shape #8 and 22 are much more difficult to measure than all the others.

Analyzing the signal of the operators in the T_2^{++} -channel we found that the shape #7, the first and third projection of #8, as well as shape #17, 19, the first projections of #18 and 20 could not be well measured on all the smearing schemes.

In the A_1^{-+} -channel all operators could be well measured, nevertheless we

excluded smearing scheme 1, 2 and 3 in our analysis improving the result considerably.

While none of the ten measured operators in the A_2^{-+} -channel gave any useful signal, we could still make out a tendency for the preference of lower smearing schemes.

For analyzing the E^{-+} -channel we excluded the first two smearing schemes and the first projection of shape #8 and 22, however the lattice spacing is already too coarse to get a reliable signal.

The T_1^{-+} -channel shows a clear preference for the lowest two smearing schemes and shape #9, 11 and 22.

In the T_2^{-+} -channel we excluded the first two smearing schemes and in smearing scheme 3, 4 and 5 the operators #7 and the second projections of #8, 18 and 20.

While in the channels $A_1^{+-}, T_2^{+-}, A_1^{--}, A_2^{--}, E^{--}$ we did not find any acceptable signal, A_2^{+-} seems to prefer #9, 14 and 22, E^{+-} #7, 9, 14 and 22 on the lowest smearing scheme, T_1^{+-} #5, 6, 7, projection two and three of #8, projection two of 9, and shapes #10, 11, 14 and 22,

The T_1^{--} -channel shows a tendency for the lowest smearing scheme and the shapes #8, 9, 18, 20, 21 and 22.

Finally, the T_2^{--} -channel prefers shape #6, 8, 9, 11 and 22 on the lower smearing schemes.

5.5 Conclusions and outlook

The main result of this chapter is the determination of the 0^{++} and 2^{++} glueball masses using the parametrized FP action. We obtain 1627(83) MeV for the 0^{++} and 2354(95) MeV for the 2^{++} glueball mass⁶, respectively. We observe scaling within one standard deviation and restoration of the degeneracy in the 2^{++} and 2^{-+} channel. Mass estimates of the $0^{-+}, 2^{-+}$ and the 1^{+-} glueball are also obtained and they agree with the best earlier results within our albeit large statistical errors. Besides being interesting physical results by themselves, this calculation provides a determination of glueball masses with a very different formulation of lattice gauge theory and, in that sense, confirms universality.

In addition, we observe scaling of the results within one standard deviation and the perfect properties of the parametrized FP action as seen in chapter 4 are confirmed.

As mentioned in the introduction, it is well known, that glueball masses are difficult to measure on the lattice. Indeed, we can barely resolve higher lying glueball states and measuring excited states becomes impossible at the lattice spacings currently available to us. In this sense we can not really take advantage of the parametrized FP action, which is intended to be used on coarse lattices.

One way around this difficulty is to use anisotropic lattices, where the lattice spacing in temporal direction is much smaller than in spatial direction, $a_t \ll a_s$. The construction of an anisotropic parametrized FP action is currently under investigation and we refer to the last chapter for an outlook.

⁶Only the 0^{++} value represents a continuum value, while the 2^{++} value corresponds to the one measured at a lattice spacing of $a = 0.10$ fm.

Chapter 6

Conclusions and outlook

In this work we have presented a new parametrization of the FP action of a specific RGT. The new parametrization reproduces the classical properties of the action excellently. This action was tested extensively on the static quark–antiquark potential, the finite temperature phase transition and on the glueball spectrum.

The approach we use is building simple loops (plaquettes) from single gauge links as well as smeared links. We analytically calculated the couplings of the FP action in the quadratic approximation and care was taken not to violate the $\mathcal{O}(a^2)$ (“on–shell”) Symanzik conditions. It is interesting to note that within this new ansatz the second Symanzik condition is automatically fulfilled. We also checked that the parametrization respects approximate scale invariance of instanton solutions.

We parametrized the FP action at lattice spacings suitable for performing simulations on coarse lattices in physically interesting regions. Since we are not only parametrizing the action values but also the derivatives with respect to the gauge fields as well, the action is especially suited for the use in Monte Carlo simulations.

For testing the action we measured the critical temperature and the static quark–antiquark potential at various values of the gauge coupling. We produced physically interesting results by measuring the glueball spectrum in all symmetry channels. The problematic A_1^{++} –channel is an excellent candidate for testing the improvements and it indeed shows much reduced lattice artifacts at moderate lattice spacing $a \simeq 0.1$ fm as compared to the Wilson gauge action. We have determined glueball masses of 1627(83) MeV for the 0^{++} glueball in the continuum and 2354(95) MeV for the 2^{++} glueball at a lattice spacing of $a = 0.1$ fm.

The results of this work are now being processed for publication.

Another project currently under study is the construction of a parametrized FP gauge action on anisotropic lattices. This generalization has not been done until now but it is needed especially to tackle the full glueball spectrum including excited states and finds its application in a wide range of problems like the determination of the string tension or finite temperature physics.

We have new ideas for the construction of such anisotropic FP actions and for more physical ways of extracting the effective renormalized anisotropy a_τ/a_σ ,

which is a particular problem in anisotropic lattice studies. We analytically calculated the couplings and the spectrum in the quadratic approximation as well as the tree level perturbative static potential. As expected the spectrum is exact and has the correct anisotropy, while the static potential shows excellent rotational symmetry and has very little lattice artifacts even at distance $r = 1$. The main idea for the construction of an anisotropic FP action on coarse lattices is to use the parametrized FP action presented in this work as a starting point and to perform one or several RGT steps in the spatial directions only. In this way one obtains an action on an anisotropic lattice, which shares all the classical properties of the isotropic counterpart.

Different possibilities for the parametrization of the action at coarse lattice spacings are currently under investigation.

Appendix A

The $\mathcal{O}(a^2)$ and $\mathcal{O}(a^4)$ Symanzik conditions

A.1 The $\mathcal{O}(a^2)$ Symanzik conditions

In this appendix we derive the $\mathcal{O}(a^2)$ Symanzik conditions [87, 88, 89, 90, 91, 92] by considering constant non-abelian gauge potentials. The formulas apply to both SU(2) and SU(3).

It is useful to first define for a general gauge field in the continuum a dimension-4 operator

$$R_0 = -\frac{1}{2} \sum_{\mu\nu} \text{Tr} (\mathcal{F}_{\mu\nu}^2), \quad (\text{A.1})$$

and three dimension-6 operators:

$$R_1 = \frac{1}{2} \sum_{\mu\nu} \text{Tr} \left((D_\mu \mathcal{F}_{\mu\nu})^2 \right), \quad (\text{A.2})$$

$$R_2 = \frac{1}{2} \sum_{\mu\nu\lambda} \text{Tr} \left((D_\mu \mathcal{F}_{\nu\lambda})^2 \right), \quad (\text{A.3})$$

$$R_3 = \frac{1}{2} \sum_{\mu\nu\lambda} \text{Tr} (D_\mu \mathcal{F}_{\mu\lambda} D_\nu \mathcal{F}_{\nu\lambda}). \quad (\text{A.4})$$

The equations of motion are $\sum_\mu D_\mu \mathcal{F}_{\mu\lambda} = 0$ hence the $\mathcal{O}(a^2)$ ('on shell') Symanzik conditions imply only that the coefficients of R_1 and R_2 vanish when one expands a lattice action in powers of the lattice spacing a . The coefficient of R_3 is not required to vanish (and usually it does not for the FP action).

Let us now specify to constant gauge potentials, $\partial_\mu A_\nu = 0$. In the continuum one has

$$\mathcal{F}_{\mu\nu} = [A_\mu, A_\nu] \quad (\text{A.5})$$

and

$$D_\mu \mathcal{F}_{\nu\lambda} = [A_\mu, \mathcal{F}_{\nu\lambda}]. \quad (\text{A.6})$$

Here A_μ and $\mathcal{F}_{\mu\nu}$ are chosen to be anti-hermitian.

We can put a constant non-abelian gauge field on the lattice by defining

$$\mathcal{A}_\mu = i\alpha_\mu \cdot \frac{1}{2}\sigma_\mu, \quad (\text{A.7})$$

where $\sigma_k, \mu = k = 1, 2, 3$ are the Pauli matrices, while $\sigma_4 = (\sigma_1 + \sigma_2 + \sigma_3)/\sqrt{3}$. Expanding any lattice gauge action in powers of α_μ and identifying the coefficients of the operators defined in (A.1)-(A.4) one derives the $\mathcal{O}(a^2)$ Symanzik conditions and a normalization condition.

For the specific lattice gauge action ansatz considered in section 2.3 one obtains¹

$$\begin{aligned} \sum_{\mu < \nu} w_{\mu\nu} = & \frac{1}{4}R_0(1 + (4 + 2\eta_0)c_1) \\ & + \frac{1}{12}R_1 \left(1 - 2c_1(1 - 4\eta_0) + \frac{3}{2}(1 - \eta_0)^2(c_1^2 - 2c_2) \right) \\ & + \frac{1}{2}R_3 \left(c_1 + \frac{1}{4}(1 + 2\eta_0)(c_1^2 - 2c_2) \right). \end{aligned} \quad (\text{A.8})$$

The normalization condition is obtained from the coefficient of R_0 ,

$$p_{10} + p_{01}(1 + (4 + 2\eta_0)c_1) = 1. \quad (\text{A.9})$$

The first $\mathcal{O}(a^2)$ Symanzik condition requires the coefficient of R_1 to vanish,

$$p_{10} + p_{01} \left(1 - 2c_1(1 - 4\eta_0) + \frac{3}{2}(1 - \eta_0)^2(c_1^2 - 2c_2) \right) = 0. \quad (\text{A.10})$$

It is interesting to see that the operator R_2 is absent and hence the second $\mathcal{O}(a^2)$ Symanzik condition is satisfied automatically for the general ansatz considered here. Reflecting the fact that when the FP action is expressed in terms of simple loops some of them give a nonzero coefficient of R_2 , this is even more astonishing.

A.2 Conditions from constant abelian gauge fields

For any solutions of the lattice equations of motion the value of the FP action should coincide with the value of the continuum action on the corresponding continuum solution. Since a constant abelian gauge field ($F_{\mu\nu} = \text{const.}$) is a solution in the continuum, it should also be a solution on the lattice. This fact can be used to derive conditions which should be fulfilled by the FP action, however, it provides a nice and convenient method for calculating conditions, e.g. normalization or $\mathcal{O}(a^4)$ conditions, for any lattice gauge action. In the following we demonstrate the efficiency of the method by means of calculating the norm and $\mathcal{O}(a^4)$ Symanzik conditions. Note that the example is for a parametrization where $p_{11} = 0$ for simplicity.

¹From the non-linear parameters only the zeroth order coefficients contribute to the normalization and the $\mathcal{O}(a^2)$ Symanzik condition. To keep notation simple we substitute $c_i^{(0)} \rightarrow c_i$ in the rest of this section.

Let us first remark that the constant abelian gauge fields do not contribute to the $\mathcal{O}(a^2)$ Symanzik conditions since the corresponding dimension-6 operators are identically zero for this case. The $\mathcal{O}(a^4)$ conditions obtained below are therefore less important than the $\mathcal{O}(a^2)$ conditions obtained in the previous section and should be used in the fit only if they do not change significantly other, maybe more important, properties of the FP action.

Nevertheless, the formulae are very useful for checking the programs, even if the corresponding constraints are not implemented.

Consider now a lattice gauge potential on an infinite lattice given by

$$U_\mu(n) = \exp\left(i\frac{1}{2}\sigma_3\alpha_{\mu\nu}n_\nu\right), \quad (\text{A.11})$$

where $\alpha_{\mu\nu} = -\alpha_{\nu\mu}$. Then one has

$$S_\mu^{(\nu)}(n) = 2 \cos \alpha_{\mu\nu} U_\mu(n), \quad (\text{A.12})$$

$$Q_\mu^s(n) = -\frac{1}{3} \sum_{\lambda \neq \mu} (1 - \cos \alpha_{\mu\lambda}) U_\mu(n) \quad (\text{A.13})$$

and

$$x_\mu = -\frac{2}{3} \sum_{\lambda \neq \mu} (1 - \cos \alpha_{\mu\lambda}). \quad (\text{A.14})$$

With this one calculates $\eta(x_\mu)$ and $c_i(x_\mu)$. Further one finds

$$Q_\mu^{(\nu)}(n) = A_\mu^{(\nu)} U_\mu(n), \quad (\text{A.15})$$

where

$$A_\mu^{(\nu)} = -\frac{1}{2} \left[\sum_{\lambda \neq \mu\nu} (1 - \cos \alpha_{\mu\lambda}) + \eta(x_\mu)(1 - \cos \alpha_{\mu\nu}) \right]. \quad (\text{A.16})$$

The asymmetrically smeared link is

$$W_\mu^{(\nu)}(n) = B_\mu^{(\nu)} U_\mu(n), \quad (\text{A.17})$$

where

$$B_\mu^{(\nu)} = 1 + c_1(x_\mu) A_\mu^{(\nu)} + c_2(x_\mu) (A_\mu^{(\nu)})^2 + \dots \quad (\text{A.18})$$

The smeared plaquette variable is

$$w_{\mu\nu} = 2 \left[1 - \cos \alpha_{\mu\nu} \left(B_\mu^{(\nu)} B_\nu^{(\mu)} \right)^2 \right], \quad (\text{A.19})$$

and the standard plaquette variable yields

$$u_{\mu\nu} = 2(1 - \cos \alpha_{\mu\nu}). \quad (\text{A.20})$$

Expanding in powers of $\alpha_{\mu\nu}$ one obtains for the $\mathcal{O}(a^2)$ terms²

$$\mathcal{A} = V (p_{10} + p_{01}(1 + (4 + 2\eta_0)c_{10})) (\alpha_{12}^2 + \alpha_{13}^2 + \dots), \quad (\text{A.21})$$

²For simplicity of notation we set $c_i^{(j)} \rightarrow c_{ij}$ for the rest of this section.

which yields again the normalization condition eq. (A.9).

The value of the action should be purely quadratic in α , hence the terms proportional to $\alpha_{12}^2\alpha_{13}^2$ and α_{12}^4 should vanish. This gives two conditions,

$$p_{01} \left[3c_{10} + \frac{9}{4}c_{10}^2(1+2\eta_0) + 2c_{11}(2+\eta_0) + \frac{3}{2}c_{20}(1+2\eta_0) \right] - 12p_{02} [c_{10} + c_{10}^2(1+2\eta_0)] = 0, \quad (\text{A.22})$$

and

$$p_{20} - \frac{1}{12}p_{10} + p_{02} (1 + 4c_{10}\eta_0 + 4c_{10}^2(1 + \eta_0^2)) - \frac{1}{12}p_{01} (1 + 2c_{10}(2 + 7\eta_0) + 3c_{10}^2(2 + 3\eta_0^2) + 8c_{11}(2 + \eta_0) + 6c_{20}(2 + \eta_0^2)) = 0. \quad (\text{A.23})$$

By expressing p_{01} through the normalization condition eq. (A.9) one gets equivalently

$$p_{20} = \frac{1}{12} + \frac{1}{3}p_{01} \left[3c_{10}\eta_0 + \frac{3}{4}c_{10}^2(2 + 3\eta_0^2) + 2c_{11}(2 + \eta_0) + \frac{3}{2}c_{20}(2 + \eta_0^2) \right] - p_{02} [1 + 4c_{10}\eta_0 + 4c_{10}^2(1 + \eta_0^2)]. \quad (\text{A.24})$$

Equations (A.22) and (A.24) define e.g. p_{20} and p_{02} as a function of the non-linear parameters η_i and $c_i^{(j)} \equiv c_{ij}$. Note that higher order coefficients do not contribute to this order, and that p_{10} and p_{01} are assumed to be fixed from the normalization and the $\mathcal{O}(a^2)$ Symanzik conditions.

Appendix B

Instanton classical solutions on the lattice

In this appendix we describe the construction and generation of instanton configurations on the lattice and how they can be used in the determination of a parametrized FP action.

FP actions are classically perfect lattice actions, which possess scale-invariant instanton solutions down to a minimum size of around one lattice spacing. The FP action value for these solutions coincides with the continuum value, $A_{\text{inst}}^{\text{cont}}, A^{\text{FP}} = |Q^{\text{FP}}| A_{\text{inst}}^{\text{cont}}$, where Q^{FP} is the FP topological charge operator on the lattice defined through the FP equation, eq. (2.4). For any other configuration U the FP action will be larger than the corresponding continuum one-instanton action $A^{\text{FP}}(U) \geq |Q^{\text{FP}}(U)| A_{\text{inst}}^{\text{cont}}$. Therefore FP actions are especially suited for lattice studies of topology, which are usually hampered by the presence of large lattice artifacts, caused by so called dislocations [93, 94], i.e. non-zero charged configurations whose contribution to the topological charge comes entirely from small localized regions of $\mathcal{O}(a^4)$. FP actions, however, allow a theoretically clean approach to topology on the lattice [2, 95, 96, 3, 97], which has been applied successfully in SU(2) lattice gauge theory [11, 12, 13].

Strictly speaking one-instanton solutions on a lattice with periodic boundary conditions do not exist. This problem can in principle be circumvented by either using twisted boundary conditions or one-instanton classical solutions on open lattices [14]. However, despite of all this, approximate classical solutions as constructed below can still be taken into account in the determination of parametrized FP actions on the footing of normal configurations and they can serve to check the flexibility of the present ansatz for the parametrization.

We will first review the construction of SU(2) one-instanton classical solutions on the lattice and then report on some results and observations in the context of generating these configurations.

B.1 Construction of SU(2) single instanton configurations

We begin with the known gauge potential for a single continuum SU(2) instanton of size ρ centered at $x = 0$ in the smooth regular gauge:

$$A_\mu(x) = \frac{x^2}{x^2 + \rho^2} g^\dagger(x) \partial_\mu g(x), \quad (\text{B.1})$$

with

$$g(x) = \frac{x_4 + i x_i \sigma_i}{|x|}, \quad (\text{B.2})$$

where $\sigma_i, i = 1, 2, 3$ are the Pauli matrices. This solution can be trivially shifted to any center x_c . As mentioned above, such a single instanton configuration is not a solution of the classical equations of motion on a periodic volume. Indeed, putting the solution on a periodic torus of size L one finds [11] that its action diverges linearly due to the discontinuity of the field configuration on the boundary $x_4 = \pm L/2$, $A(L) = A_{\text{inst}} + \mathcal{O}(L)$. Following Pugh and Teper [94] the problem can be alleviated by considering instead configurations made of an instanton and a superimposed dislocation¹. This is achieved by performing a singular gauge transformation on the configuration given in (B.1) before putting it on the lattice,

$$V_\mu(n) = g(n) U_\mu(n) g^\dagger(n + \hat{\mu}), \quad (\text{B.3})$$

where $g(x)$ is defined in equation (B.2) and U_μ, V_μ are gauge link matrices on the lattice. Following [11] the finite volume correction to the action of this configuration is $A(L) = A_{\text{inst}} + \mathcal{O}(1/L^3)$ and we will use the ansatz

$$A(L) = A_{\text{inst}} + a_1 \left(\frac{\rho}{L}\right)^3 + a_2 \left(\frac{\rho}{L}\right)^5 \quad (\text{B.4})$$

when studying the finite size behavior of the configurations.

In order to discretize the above configurations we define the link variables on the lattice by approximating the path ordered exponential

$$U_\mu(n) = \mathcal{P} \exp \left(i \int_n^{n+\hat{\mu}} A_\mu(x) dx \right) \quad (\text{B.5})$$

through a product along the lines of the lattice,

$$U_\mu(n) = \prod_j \Delta U_\mu(n, j), \quad (\text{B.6})$$

where the factors

$$\Delta U_\mu(n, j) = \exp(i A_\mu(x_j = na + j\Delta x \hat{\mu}) \Delta x) \quad (\text{B.7})$$

are evaluated for the interval $[x_j - \Delta x/2, x_j + \Delta x/2]$. One typically breaks the lattice spacing up into 20 equal intervals, $\Delta x = a/20$, in order to achieve an accurate evaluation of (B.5) for all cases of interest.

¹The dislocation can be interpreted as the remnant of a small anti-instanton that fell through the lattice.

A much nicer way is to use a closed expression of equation (B.5) obtained by performing the path ordered integral analytically [98]:

$$U_4(x) = \cos f_4(x) - i \frac{x_i \sigma_i}{\sqrt{x^2 - x_4^2}} \sin f_4(x), \quad (\text{B.8})$$

$$U_i(x) = \cos f_i(x) + i \frac{x_4 \sigma_i - \epsilon_{ijk} x_j \sigma_k}{\sqrt{x^2 - x_i^2}} \sin f_i(x), \quad i = 1, 2, 3, \quad (\text{B.9})$$

$$f_\mu(x) = \sqrt{\frac{x^2 - x_\mu^2}{x^2 - x_\mu^2 + \rho^2}} \times \left[\arctan \left(\frac{a + x_\mu}{\sqrt{x^2 - x_\mu^2 + \rho^2}} \right) - \arctan \left(\frac{x_\mu}{\sqrt{x^2 - x_\mu^2 + \rho^2}} \right) \right]. \quad (\text{B.10})$$

With these expressions the instanton configurations can directly be put on the lattice with $x_\mu/a = \text{integer}$ provided x_c is not a lattice site. In order to close the boundary we perform a singular gauge transformation as mentioned previously,

$$V_\mu(x) = g(x) U_\mu(x) g^\dagger(x + \hat{\mu}), \quad (\text{B.11})$$

where $V_\mu(x)$ is now as close as possible to the unity at the boundary.

B.2 Results and comments on $SU(2)$ single instanton configurations

We generated $SU(2)$ single instanton configurations on a 12^4 lattice with the instanton radius ρ/a ranging from 3.0 down to 1.1 centered in a hypercube, $x_c = (5.5, 5.5, 5.5, 5.5)$, in a cube, $x_c = (5.5, 5.5, 5.5, 6)$, and in a plaquette, $x_c = (5.5, 5.5, 6, 6)$, in the singular gauge following the construction as presented in the previous section. Then we blocked the configurations down to a 6^4 lattice, the instanton radii being halved, and then inverse blocked them back to the fine lattice. The inverse blocking means that, keeping the coarse configuration fixed, one searches for a configuration which minimizes the r.h.s. of the FP equation (2.4). The configurations are minimized until the action decrease per sweep was less than 10^{-6} to 10^{-8} . As the starting fine configuration we used the originally generated fine configuration.

It is interesting to investigate the minimization process more closely in order to observe the falling through the lattice of the instantons. As expected it turns out that the instanton solutions are relatively smooth configurations even on the coarse lattice having $u \leq 0.25$ except for some plaquettes near the instanton center. The fluctuations of these few plaquettes are growing when the instanton radius ρ/a is decreased, i.e. when the instantons are more and more localized objects, and they reach a maximum value between $1 \leq u \leq 2$ at around $\rho/a \simeq 1$. This is exactly when the instanton falls through the lattice to possibly become a dislocation.

This falling through is expressed in the minimization process through a jump in the value of the blocking kernel, which is exactly zero for a classical solution and non-zero for any other configuration. Figures B.1 shows the evolution of

one-instanton classical solutions on a 12^4 lattice centered in a hypercube during the minimization process. V is the fixed coarse configuration and U denotes the minimized configuration on the fine lattice. The radius ρ of the instanton configurations is in units of the coarse lattice spacing. Note, that $A^{\text{FP}}(V) = A^{\text{FP}}(U) + T(U, V)$ and that for an exact classical solution of the FP action one has $T(U, V) = 0$. The values of the action and the blocking kernel are in units of the continuum action value $4\pi^2$, while the action decrease per sweep is rescaled appropriately.

The first configuration with $\rho/a = 0.90$ is already close to a classical solution right from the beginning and it converges to the final minimized configuration very fast. Note that $T(U, V)$ is indeed zero up to finite volume corrections $\mathcal{O}((\rho/L)^3)$ from the boundaries.

The second configuration with $\rho/a = 0.85$ is still close to a classical solution at the beginning, but slowly deviates from it during the minimization process. After around 35 sweeps, a different more preferable minimizing configuration is found, which is no longer a classical solution ($T(U, V) \neq 0$). This is when the instanton falls through the lattice and it is expected to be accompanied by a drop of the FP topological charge Q^{FP} from $Q^{\text{FP}} = 1$ to $Q^{\text{FP}} = 0$, thereby preventing the configuration from being a dislocation.

The third configuration falls through the lattice after already 10 sweeps and first converges towards a local minimum in the space of minimizing configurations before finding the true, presumably global minimum.

These results are collected in figure 2.1 in section 2.5 on the example of configurations centered in a hypercube. The falling through the lattice is clearly visible from the jump in $A(U)$ and $T(U, V)$ and shows itself in the discontinuity in $A(V)$ at $\rho/a \sim 0.88$. Similar figures are obtained on configurations centered in a cube and a plaquette, respectively.

As is clear from section 2.5 one has large degrees of freedom in parametrizing a FP action, and indeed, we have several equally good parametrizations on the intermediate level being appropriate for fluctuations involved in the instanton configurations. It is interesting to see how the minimized configurations are influenced by the choice of the action in the minimization procedure. It turns out that minimized configurations differ significantly from each other: using some parametrized FP action on a configuration previously minimized with a different parametrized FP action can result in an action decrease during the first sweep as high as $8 \cdot 10^{-2}$, however, the action value itself, $A(U) + T(U, V)$ does not differ more than 1.2% in the end. This is just an artifact of our inability to parametrize the FP action accurately enough, but consolidates the expectation that the choice of the action should not be crucial apart from fulfilling some minimal requirements.

Having the final parametrization of the FP action at hand, it is interesting to see how the action performs on generic instanton solutions. For this purpose we generated several instanton configurations with varying radii $\rho/a = 1.1, \dots, 3.0$ and on different lattices $L = 8, 10, \dots, 18$ according to the procedure described above. These configurations are then blocked to a coarse lattice and evaluated with the parametrized FP action given in table 2.1, and finally, the results are extrapolated to infinite volume using formula (B.4). The results for instanton configurations centered in a cube is shown in figure 2.2 in section 2.5 and com-

pared to the results obtained with the Wilson action. Figure B.2 shows the same for instanton configurations centered in a plaquette.

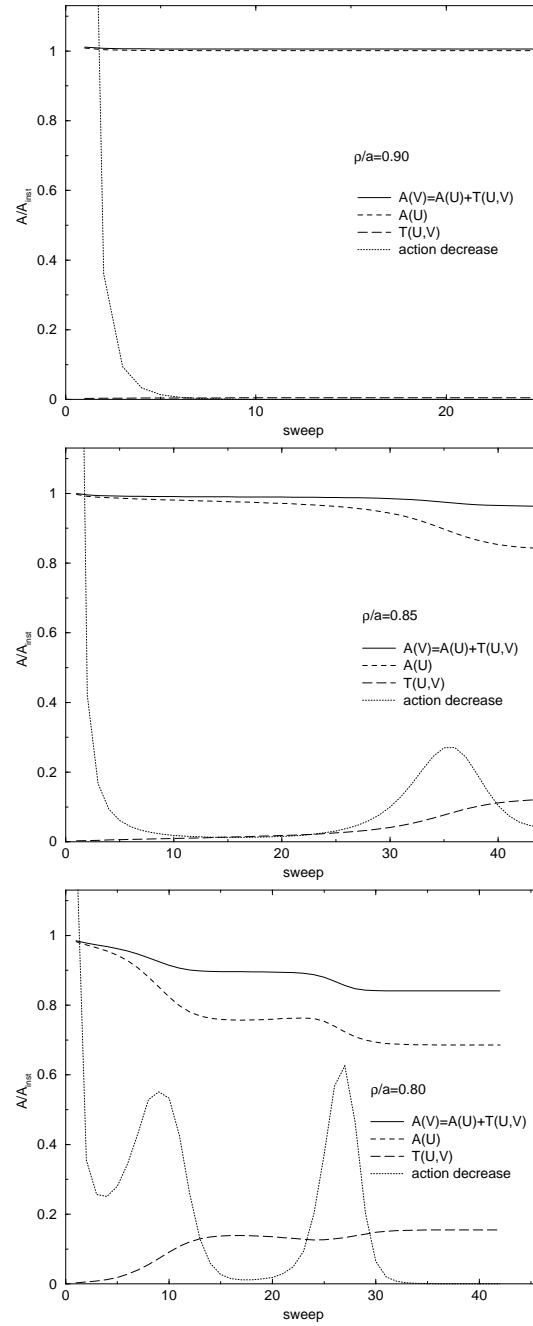


Figure B.1: SU(2) single instanton solutions of different sizes on a 12^4 lattice with center in a hypercube during the minimization process. The action decrease is per sweep and is rescaled appropriately.

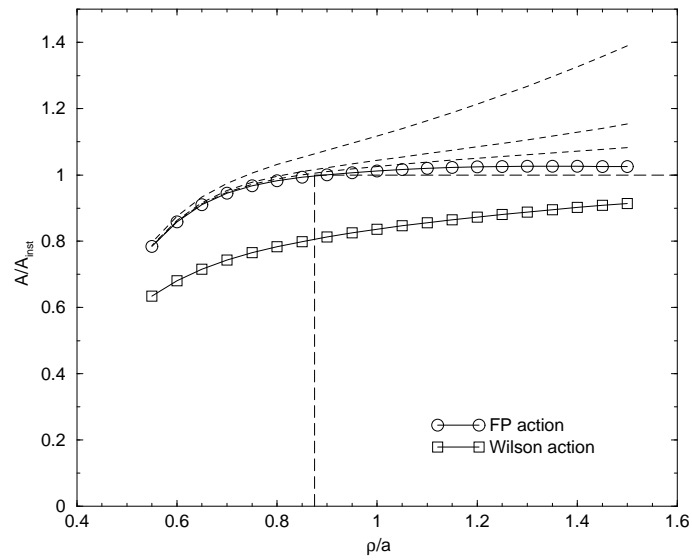


Figure B.2: $SU(2)$ single instanton solutions of different sizes centered inside a plaquette. The solid lines are extrapolations to infinite lattice. For the parametrized FP action we also plot the action values on the finite lattices with size $L = 4, 6, 8$ as dashed lines.

Appendix C

The Ferrenberg-Swendsen reweighting

In order to express quantities calculated on the lattice in physical units one has to find the relation between the coupling of the theory and the lattice cut-off a . This can, for instance, be achieved through a calculation of the critical couplings β_c for the phase transitions on lattices with given temporal extent N_τ . However, the determination of the critical couplings is in general a delicate and subtle matter and therefore having different methods of determining the critical points of the theory at hand may be of great help.

The Ferrenberg-Swendsen reweighting [46, 45] is a method for optimizing the analysis of data from single or multiple Monte Carlo (MC) computer simulations over wide ranges of parameter values and which is based on ideas first proposed by [43, 44]. The method is applicable to simulations in lattice gauge theories as well as statistical mechanics. The method allows explicit error estimates, which in turn provides a clear and simple guide for objective planning of the length of additional runs and parameter values to be simulated.

In section C.1 we will first review the Ferrenberg-Swendsen reweighting technique in the single-histogram case. Then the method is extended in section C.2 to the case when data from several MC runs are combined. Throughout the two sections, simulations of the two-dimensional Ising model will serve as elucidating examples in the case of a second order phase transition. In section C.3 finally, the method is applied to the 10-state Potts model in two dimensions as for illustration at a first order phase transition.

C.1 The single-histogram reweighting

All the information about a statistical system at a given temperature $T = 1/\beta$ is contained in the partition function,

$$Z(\beta) = \sum_{\{\sigma\}} e^{-\beta S(\sigma)} = \sum_S W(S) e^{-\beta S}, \quad (\text{C.1})$$

where $\{\sigma\}$ is the set of all configurations of the system, S is the energy for a given configuration and $W(S)$ is the density of states at energy S or the spectral density function.

The Ferrenberg-Swendsen interpolation or spectral density method relies on the fact that the density function is universal in the sense that it is the same at every temperature and thus contains in principle all the information about the system at any temperature or coupling β . In practice we can estimate the spectral density function only in some finite range of energies and we are therefore limited to a finite range of couplings near the original simulation point. However, for couplings near criticality the probability distributions for the states involved are very broad and thus there is a large overlap with typical configurations at different couplings. Therefore the method is most powerful in the vicinity of criticality.

Consider now a simulation at coupling β with n_β measurements. The value S for the action appeared $N_\beta(S)$ time, i.e. $\sum_S N_\beta(S) = n_\beta$. We can estimate the probability to find a configuration with energy S :

$$P_\beta(S) = \frac{W(S)e^{-\beta S}}{Z(\beta)} \approx \frac{N_\beta(S)}{n_\beta}. \quad (\text{C.2})$$

The same holds true for another arbitrary coupling β' :

$$P_{\beta'}(S) = \frac{W(S)e^{-\beta' S}}{Z(\beta')}. \quad (\text{C.3})$$

Dividing equations (C.2) and (C.3) we obtain

$$P_{\beta'}(S) = P_\beta(S) e^{(\beta-\beta')S} \frac{Z(\beta)}{Z(\beta')}. \quad (\text{C.4})$$

The ratio of the two partition functions can be written as

$$\begin{aligned} \frac{Z(\beta')}{Z(\beta)} &= \sum_S \frac{W(S)e^{-\beta' S}}{Z(\beta)} \\ &= \sum_S \frac{W(S)e^{-\beta S}}{Z(\beta)} e^{(\beta-\beta')S} \\ &= \sum_S P_\beta(S) e^{(\beta-\beta')S}, \end{aligned}$$

and together with equation (C.4) we arrive at

$$P_{\beta'}(S) = \frac{P_\beta(S) e^{(\beta-\beta')S}}{\sum_S P_\beta(S) e^{(\beta-\beta')S}}. \quad (\text{C.5})$$

We can now calculate an observable \mathcal{O} at any other coupling β' from our simulation at β ,

$$\langle \mathcal{O} \rangle = \frac{1}{Z(\beta')} \sum_{\{\sigma\}} \mathcal{O}(\sigma) e^{-\beta' S(\sigma)} \quad (\text{C.6})$$

$$= \frac{1}{Z(\beta')} \sum_{\{\sigma\}} \sum_S \delta(S - S(\sigma)) \mathcal{O}(\sigma) e^{-\beta' S} \quad (\text{C.7})$$

$$= \sum_S \bar{\mathcal{O}}(S) P_{\beta'}(S), \quad (\text{C.8})$$

where the effective value of the observable at action S reads

$$\bar{\mathcal{O}}(S) = \frac{\sum_{\{\sigma\}} \delta(S - S(\sigma)) \mathcal{O}(\sigma)}{W(S)} \approx \frac{\sum_{j=1}^{N_\beta(S)} \mathcal{O}(\sigma_j)}{N_\beta(S)}. \quad (\text{C.9})$$

For illustration and for checking the implemented code let us look at the specific heat of the Ising model in two dimensions, where the exact solution is known [99]. In figure C.1 - C.3 the filled circles show the results of three MC simulations near and at the infinite volume critical coupling $\beta_c = \ln(1 + \sqrt{2})/2$. All three simulations used the Swendsen-Wang cluster algorithm [100] with 5000 sweeps for equilibration and 30000 measurements on a 16^2 lattice. The results of the reweighting procedure are shown as open circles and compared to the exact curve. Error bars are estimated using the bootstrap method. Even with modest statistics we are able to reproduce the peak of the specific heat with reasonable accuracy. Note that the peak is shifted away from β_c due to finite size effects. To understand the deviations from the exact curve and the increasing error estimates for β -values away from the simulated point it is useful to look at the energy histograms in figure C.4. The curve labeled with $\beta = \beta_c$ is the histogram from the simulation at the critical coupling and the other two histograms at $\beta = 0.375$ and $\beta = 0.475$ are computed from the input histogram by reweighting. For comparison we have included the histograms obtained from the simulations at $\beta = 0.375$ and $\beta = 0.475$, indicated by the black dots. The figure clearly shows that the simulation at β_c for example does not provide enough information about configurations typically showing up in a simulation at $\beta = 0.375$ and thus a reweighting from β_c breaks down at around $\beta = 0.4$. This breakdown is also responsible for the increase of the error estimates in the reweighted curve of the specific heat in C.3 for $\beta \leq 0.4$.

To take full advantage of the histogram reweighting technique it is advisable to combine the information from different simulations. In the next section we will explain and illustrate how this can be achieved in an efficient way.

C.2 The multi-histogram reweighting

In the last section we showed how histograms can be used to increase the amount of information obtained from a single computer simulation in the neighborhood of a critical point. For more general problems, however, it is often necessary to perform simulations at more than one parameter value. We will now describe an optimized method proposed by Ferrenberg and Swendsen for combining the data from an arbitrary number of simulations to obtain information over a wider range of parameter values. Again the method is applicable to lattice gauge theory, but for simplicity we will illustrate and test the procedure on the 2D Ising model and later on the q -state Potts model.

Let us start with recalling two simple equations from the single-histogram case:

$$P_\beta(S) = \frac{W(S) e^{-\beta S}}{Z(\beta)} \approx \frac{N_\beta(S)}{n_\beta}, \quad (\text{C.10})$$

$$W(S) \approx \frac{N_\beta(S)}{n_\beta} Z(\beta) e^{\beta S}. \quad (\text{C.11})$$

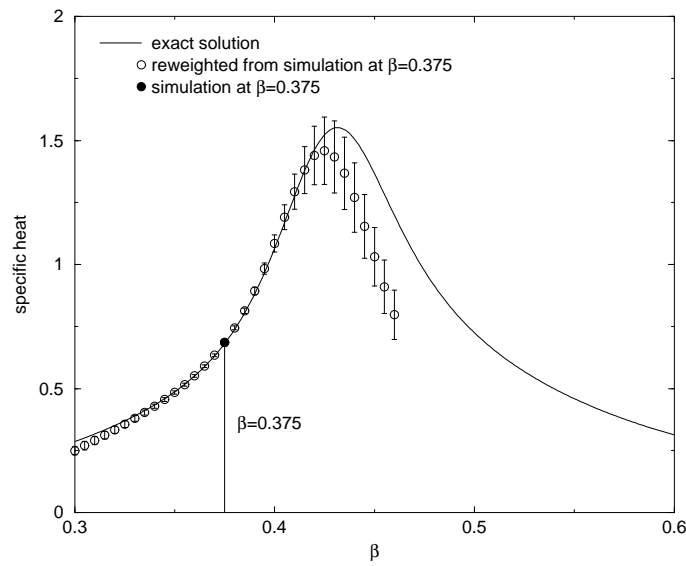


Figure C.1: The specific heat of the 2D Ising model computed by reweighting (empty circles) from a single MC simulation at $\beta = 0.375$ (filled circle) on a 16^2 lattice with 30000 measurements. The solid line indicates the exact result for comparison.

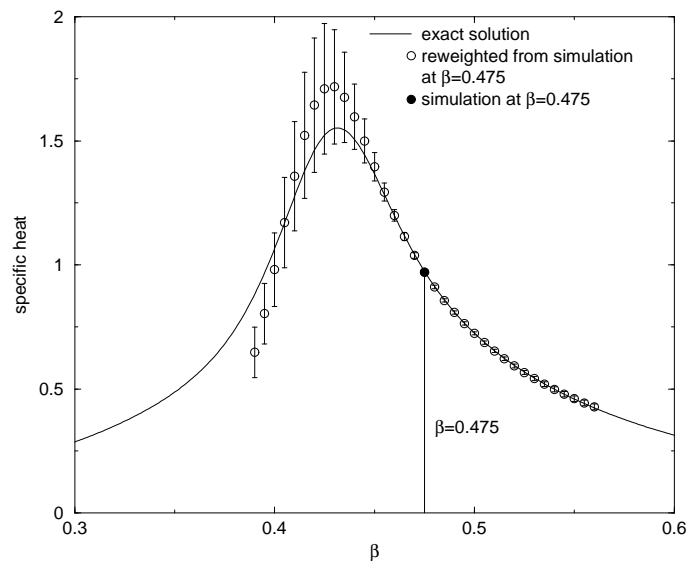


Figure C.2: The specific heat of the 2D Ising model computed by reweighting (empty circles) from a single MC simulation at $\beta = 0.475$ (filled circle) on a 16^2 lattice with 30000 measurements. The solid line indicates the exact result for comparison.

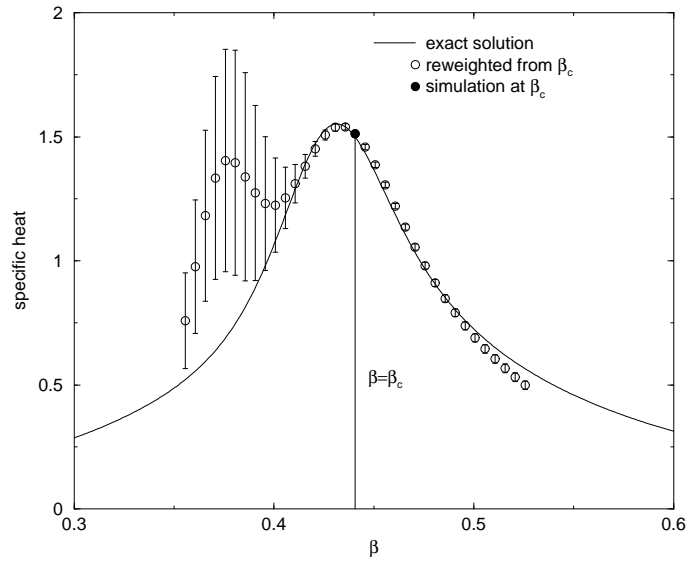


Figure C.3: The specific heat of the 2D Ising model computed by reweighting (empty circles) from a single MC simulation at $\beta = \beta_c$ (filled circle) on a 16^2 lattice with 30000 measurements. The solid line indicates the exact result for comparison .

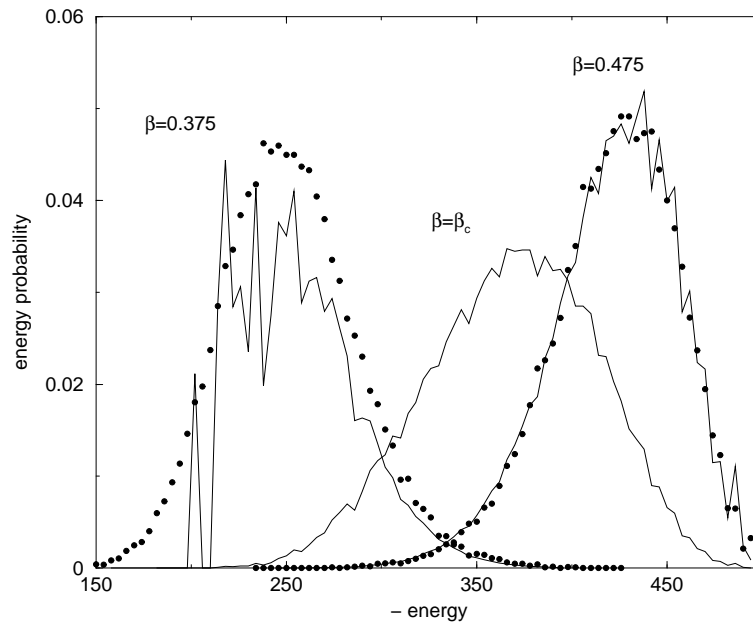


Figure C.4: The energy histogram at the simulation point $\beta = \beta_c$, and the ones reweighted to $\beta = 0.375$ and $\beta = 0.475$. The black dots indicate the histograms obtained in additional simulations at these temperatures.

Suppose we have performed MC runs at K different β -values $\beta = \beta_1, \beta_2, \dots, \beta_K$ of length n_k , where we measured the frequencies $N_k(S)$. For every run there is a partition function $Z(\beta_k)$ which corresponds to the free energy $f_k \equiv F(\beta_k)$ of the run:

$$F(\beta_k) = -\ln Z(\beta_k). \quad (\text{C.12})$$

We can write down the (estimated) spectral density function (C.10) for each of the K MC runs,

$$W_k(S) \approx \frac{N_k(S)}{n_k} Z(\beta_k) e^{\beta_k S} \quad (\text{C.13})$$

$$= \frac{N_k(S)}{n_k} e^{\beta_k S - f_k}, \quad (\text{C.14})$$

however, there should be only one unique function $\bar{W}(S)$. To get an improved estimate for $\bar{W}(S)$ one takes a weighted average of the previously defined density functions with the following ansatz:

$$\bar{W}(S) \equiv \sum_{k=1}^K p_k(S) W_k(S) \quad \text{with} \quad \sum_{k=1}^K p_k(S) = 1. \quad (\text{C.15})$$

Ferrenberg and Swendsen proposed to choose the weights such that the error in the resultant estimate for $\bar{W}(S)$ is minimized, assuming that the errors on the relative frequencies $N_k(S)/n_k$ is $g_k/n_k = (1 + 2\tau_k)/n_k$, with τ_k being the integrated autocorrelation time. With this condition one gets

$$p_k(S) = \frac{\frac{n_k}{g_k} e^{-\beta_k S + f_k}}{\sum_{l=1}^K \frac{n_l}{g_l} e^{-\beta_l S + f_l}} \quad (\text{C.16})$$

and

$$\bar{W}(S) = \frac{\sum_{k=1}^K \frac{N_k(S)}{g_k}}{\sum_{l=1}^K \frac{n_l}{g_l} e^{-\beta_l S + f_l}}. \quad (\text{C.17})$$

One can now calculate the partition function at an arbitrary β -value,

$$\bar{Z}(\beta) = \sum_S \bar{W}(S) e^{-\beta S}, \quad (\text{C.18})$$

and from this the corresponding free energies

$$f_k = -\ln \bar{Z}(\beta) \Big|_{\beta=\beta_k}, \quad (\text{C.19})$$

which have to be regarded as implicit conditions for each of the f_k 's. We now give up the original definition, that f_k is the free energy of the particular MC run at β_k , but instead assume them to be free parameters, using equations (C.18) and (C.19) iteratively to find a self-consistent solution. Efficient convergence is obtained by using the derivatives of the new values of f_k as functions of the old values in the iteration process.

The expectation value of any observable can be calculated at some arbitrary coupling β' using the formula

$$\langle \mathcal{O} \rangle_{\beta'} = \frac{1}{\bar{Z}(\beta')} \sum_S \bar{\mathcal{O}}(S) \bar{W}(S) e^{-\beta' S}. \quad (\text{C.20})$$

In practise all the formulas are expressed in terms of action differences and β -value shifts in order to deal with numerically stable quantities.

For illustration we again resort to the 2D Ising model and calculate the reweighted specific heat from the two simulations at $\beta = 0.375$ and $\beta = 0.475$. The impressive result is displayed in figure C.5. One sees that the error estimates are small over the whole range of β -values considered indicating that the reweighted curve is calculated accurately enough to determine the critical coupling very precisely. Indeed, the reweighted curve coincides with the exact result within less than one standard deviation.

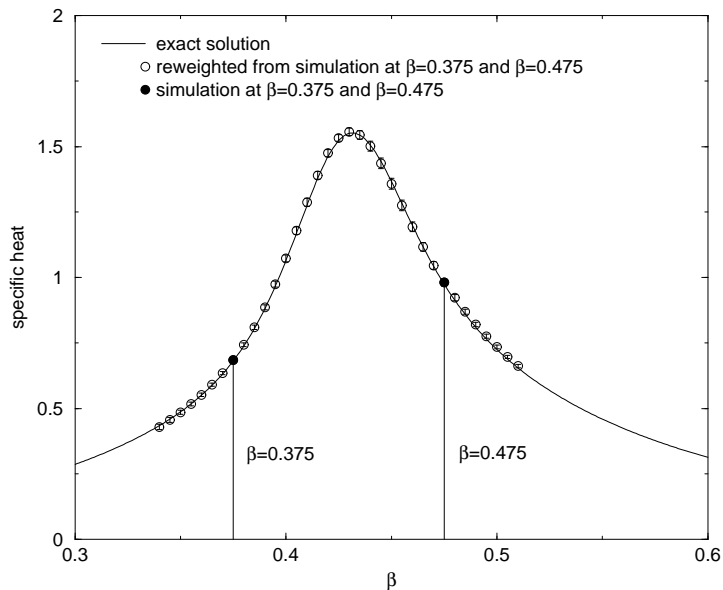


Figure C.5: The specific heat of the 2D Ising model computed by reweighting (empty circles) from two MC simulations at $\beta = 0.375$ and $\beta = 0.475$ (filled circles) on a 16^2 lattice with 30000 measurements each. The solid line indicates the exact result for comparison.

C.3 Reweighting at first order phase transitions

The mechanism of the reweighting procedure relies on the fact that the distribution of configurations at a given β -value overlaps with the distribution at another β -value. As emphasized in the previous sections this feature is even enhanced near the criticality of a second order phase transition, where the probability distributions for the states involved are very broad. Reflecting the fact that at a first order phase transition, the energy probability distributions shows a double peak structure (cf. figure 3.3) it is not obvious from the beginning if the proposed method is as powerful as for a second order phase transition. Indeed, by simulating at a temperature slightly below or above the critical temperature, we are collecting information about configurations in one or the other phase only and it is merely exactly at the critical point where we encounter coexistence of

the two distinct phases and thus have access to information on both phases.

As it turns out the difficulties are relieved due to the fact that one has to work on finite volumes, where the sharp first order phase transition is rounded off. In fact, near the critical temperature the system will jump from one phase to the other from time to time, thence yielding information about the probability distributions of configurations in both phases. As a testing ground for this claim we have to resort to a statistical system which is easy to simulate and which exhibits a first order phase transition. Such a model is provided by a generalization of the Ising model in two dimensions, the q -state Potts model [101]. The model is defined through the Hamiltonian

$$H_{\text{Potts}} = -\beta \sum_{\langle ij \rangle} \delta_{\sigma_i \sigma_j}, \quad \sigma_i \in 1, \dots, q, \quad (\text{C.21})$$

where $\sum_{\langle ij \rangle}$ denotes the sum over all nearest neighbors, and where we recover the Ising model by setting $q = 2$. In two dimensions the system is exactly known to exhibit a second order phase transition for $q \leq 4$ and a first order transition for all $q \geq 5$ [102]¹. Since the first order phase transition is known to be weak for small q , we choose $q = 10$ in our study.

Let us first look at the energy probability distribution of the system. In figure C.6 we display the energy distribution of a simulation at $\beta = 1.405$ near the finite volume critical coupling. The other two histograms are the

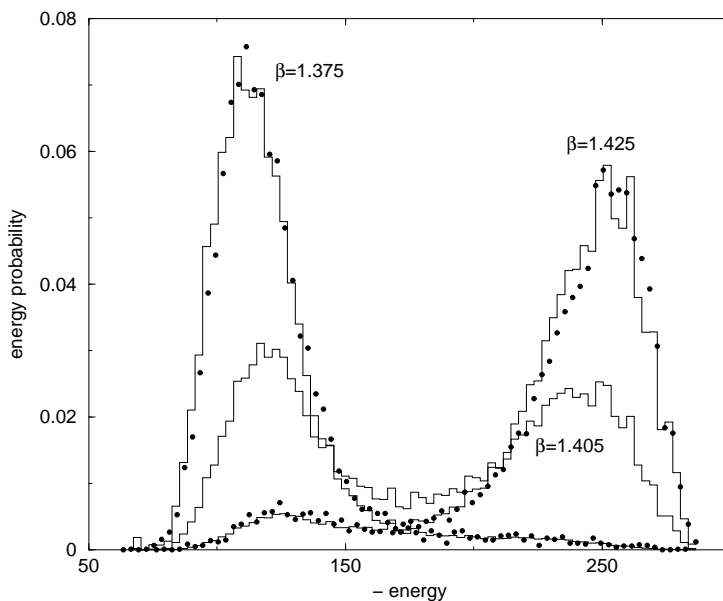


Figure C.6: The energy histogram at the simulation point $\beta = 1.405$ near the critical coupling and the ones reweighted to $\beta = 1.375$ and $\beta = 1.425$. The black dots indicate the histograms obtained in additional simulations at these temperatures.

energy distributions obtained by reweighting to $\beta = 1.375$ and $\beta = 1.425$, while

¹In three dimensions the model enjoys a first order phase transition for all $q \geq 3$.

the black dots show the results of the corresponding additional simulations for comparison. In all simulations we use the Metropolis update algorithm on a 12^2 lattice with 10^4 sweeps for equilibration and 10^4 measurements on 10^6 sweeps. The quantitative coincidence of the reweighted distributions with the simulated ones is very convincing even in the tails of the distributions.

As a final check let us look at the magnetic susceptibility of the system. As opposed to the Ising model in two dimensions no exact solution is known for the q -state Potts model. Therefore we compare the result obtained from the reweighting to additional simulations near the estimated critical temperature². In figure C.7 the filled circles denote the results of two MC simulations at $\beta = 1.375$ and $\beta = 1.425$ and the solid line shows the results obtained by reweighting the data from the two simulations. Error bars and bands are calculated using a bootstrap procedure. The empty circles show the results of additional simulations at several couplings around the critical value. For clarity the region around the peak is enlarged in figure C.8, where we also include the curve obtained by reweighting the data from the additional simulations. As in the Ising model the susceptibility peak can be reproduced with an amazing accuracy. Indeed, if we determine the critical coupling as the location of the susceptibility peak we obtain $\beta_c = 1.4051(11)$ from the simulations at $\beta = 1.375$ and $\beta = 1.425$ and $\beta_c = 1.4050(4)$ from the additional simulations.

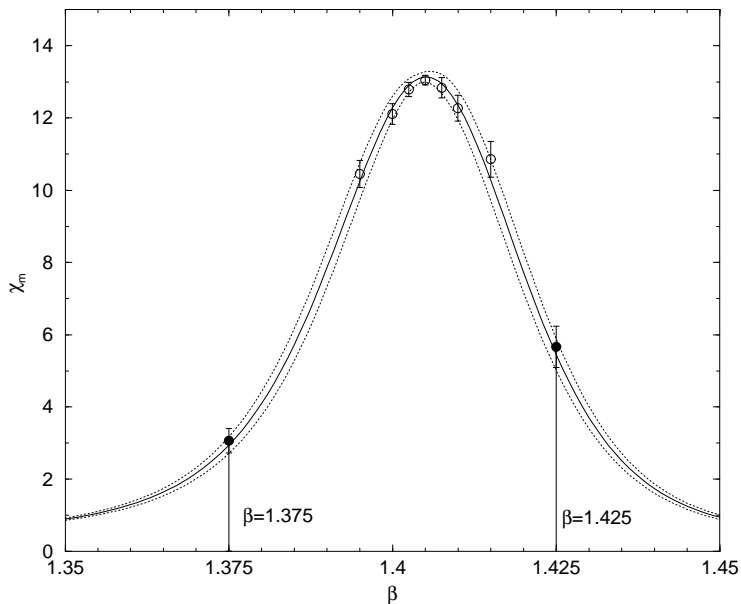


Figure C.7: The magnetic susceptibility of the 2D 10-state Potts model on a 12^2 lattice. The reweighted curve (solid line) is computed from MC simulations $\beta = 1.375$ and $\beta = 1.425$ (filled circle) and compared to additional MC simulations (empty circles).

²Although the critical coupling for the q -state Potts model is known exactly in the thermodynamic limit, $\beta_c = \ln(1 + \sqrt{q})$, we can not rely on this value due to the considerable finite volume shift.

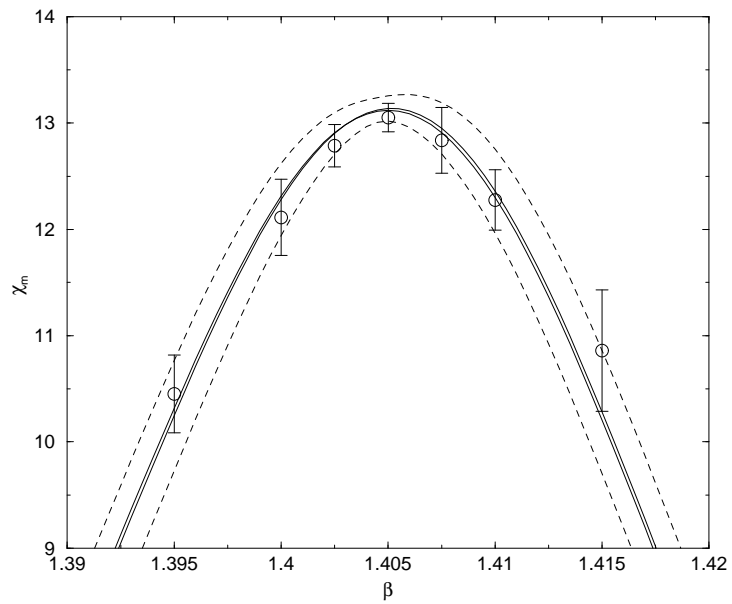


Figure C.8: Enlargement of the region around the magnetic susceptibility peak in figure C.7. The additional solid line is the reweighted curve computed from the MC simulations displayed as empty circles.

Appendix D

Extracting masses from correlation functions

It is well known that energies of particles and gauge strings can be extracted from correlation functions of operators having appropriate quantum numbers. Here we are concerned in particular with the extraction of particle and string masses, thence it suffices to consider correlation functions with zero momentum only and we suppress the momentum dependence in the following. In Euclidean space with a lattice periodic in time T we have

$$\langle 0|\mathcal{O}(t)\mathcal{O}^\dagger(0)|0\rangle \equiv C(t) = \sum_n Z_n e^{-E_n t} \quad (\text{D.1})$$

for Wilson loop correlators and

$$C(t) = \sum_n Z_n \left(e^{-E_n t} + e^{-E_n(T-t)} \right) \quad (\text{D.2})$$

for glueballs and mesons¹. The energy spectrum can in principle be extracted from the correlation functions. In particular, only the lightest state survives at large times,

$$\lim_{\text{large } t} C(t) \sim \begin{cases} e^{-E_0 t} & \text{Wilson loops,} \\ e^{-E_0 t} + e^{-E_0(T-t)} & \text{mesons, glueballs,} \end{cases} \quad (\text{D.3})$$

and thus the ground state energy can be determined from the exponential decay of the correlation function at large times.

The primary difficulty in this stage is one of reliably identifying the regions of time slices where the correlator takes the asymptotic form in equation (D.3), i.e. identifying the plateau region. For finite values of t we always have excited state contributions and therefore it is of crucial importance to have an operator with large overlap to the ground state. For this purpose different operators \mathcal{O}_n having the same quantum numbers are measured and a linear combination is constructed in order to disentangle the ground state contribution from the

¹This relation only holds for particles with integer spin and is slightly modified for spin-1/2 particles like baryons, where forwardly and backwardly propagating particles have to be distinguished.

excited state contributions. To determine the appropriate linear combination we invoke variational techniques which are described in detail in the first section of this appendix.

Once the excited state contributions are unraveled from the ground state a plateau region is identified and one can extract the ground state mass by either calculating the effective mass,

$$m_{\text{eff}}(t) = -\ln \left[\frac{C(t+1)}{C(t)} \right], \quad (\text{D.4})$$

in the plateau region or fitting the ground state correlation function $C(t)$ to an ansatz of the form given in equation (D.1) or (D.2). This issue is given further consideration in the second section of this appendix.

D.1 Variational techniques

In a simulation we estimate the elements of the $N \times N$ correlation matrix using the Monte Carlo (MC) method,

$$C_{\alpha\beta}(t) = \langle 0 | \mathcal{O}_\alpha(t) \mathcal{O}_\beta^\dagger(0) | 0 \rangle, \quad (\text{D.5})$$

where the rank N of the matrix depends on the number of smearing schemes and the number of operators under consideration. The coefficients v_α in the linear combination $\sum_{\alpha=1}^N v_\alpha \mathcal{O}_\alpha$ with the largest overlap to the ground state are determined by minimizing the effective mass²,

$$m(t_0, t_1) = -\ln \left[\frac{(v, C(t_1)v)}{(v, C(t_0)v)} \right] / (t_1 - t_0). \quad (\text{D.6})$$

This is equivalent to solving a generalized eigenvalue equation,

$$C(t_1)v = e^{-E(t_1-t_0)} C(t_0)v, \quad (\text{D.7})$$

which is well defined only for positive definite $C(t_0)$. In general, however, positiveness of $C(t_0)$ is not automatically fulfilled for $t_0 \geq 1$, but can be achieved in the following way.

We first diagonalize $C(t_0)$,

$$C(t_0)\varphi_i = \lambda_i\varphi_i, \quad \lambda_1 \geq \dots \geq \lambda_N, \quad (\text{D.8})$$

and project the correlation matrices to the space of eigenvectors corresponding to the M highest eigenvalues,

$$C_{ij}^M(t) = (\varphi_i, C(t)\varphi_j), \quad i, j = 1, \dots, M. \quad (\text{D.9})$$

By choosing the operator space too large we introduce numerical instabilities caused by very small (even negative) eigenvalues with large statistical errors due to the fact that the chosen operator basis is not independent on the given MC sample. By choosing M appropriately we can get rid of those unphysical

²In the following we use matrix notation for $C_{\alpha\beta}(t)$ and suppress the indices whenever it is appropriate.

modes while still keeping all the physical information. In this way we render the generalized eigenvalue problem well defined.

Of course the final result should not depend on the choice of M and one has to take care in each case that this is really so. Our observation is that for any acceptable statistics one always finds a plateau in M for which the extracted masses are stable under variation of M .

Note that the above procedure is not necessary for the choice $t_0 = 0$ since $C(t_0 = 0)$ is positive definite by definition. However, determining the operator basis from $C(t_0 = 0)$ and $C(t_1 = 1)$ in eq. (D.7) is under suspicion of containing little physical information about the correlation lengths, since $C(t_0 = 0)$ actually just describes the relative normalization of the operators. This is the reason for choosing $t_0 = 1, t_1 = 2$ in our analysis whenever it is possible³.

In a next step we determine the vectors $v_n, n = 1, \dots, M$ through the generalized eigenvalue equation (the index $\alpha = 1, \dots, M$ is suppressed)

$$C^M(t_1)v_n = e^{-E_n(t_1-t_0)}C^M(t_0)v_n, \quad E_1 \leq \dots \leq E_M, \quad (\text{D.10})$$

and project the correlation matrices $C^M(t)$ again to the eigenspace corresponding to the $K \leq M$ highest eigenvalues, i.e. the $K \leq M$ lowest energies,

$$C_{ij}^K(t) = (v_i, C^M(t)v_j), \quad i, j = 1, \dots, K \leq M, \quad (\text{D.11})$$

for the data-fitting phase. The truncated correlation matrices $C_{ij}^K(t)$ are fitted in the range $t = t_{\min} \dots t_{\max}$ using the ansatz

$$C_{ij}(t; \{\psi, m\}) = \sum_{n=1}^{K'} \psi_{ni} \psi_{nj}^* e^{-m_n t} \quad \text{Wilson loops} \quad (\text{D.12})$$

for the Wilson loop correlators and

$$C_{ij}(t; \{\psi, m\}) = \sum_{n=1}^{K'} \psi_{ni} \psi_{nj}^* (e^{-m_n t} + e^{-m_n(T-t)}) \quad \text{glueballs} \quad (\text{D.13})$$

for the glueball correlators. In both formulas, $\psi_{ni} \equiv (C^K(t_0)v_n)_i$ and $K' \neq K$ in general.

For all practical purposes we choose $K' = K = 1$ to obtain an energy estimate of the lowest-lying state and $K' = K = 2$ for an energy estimate of the first-excited state and an additional estimate of the ground-state energy. Increasing $K' = K$ allows to check for the stability of the energy estimate of the lowest-lying state. In the glueball analysis we choose $K' = K = 2$ or 3 for the A_1^{++} -channel where we also fit the vacuum energy and its wave function since we do not subtract the vacuum contribution $\langle \mathcal{O}_\alpha \rangle \langle \mathcal{O}_\beta^\dagger \rangle$ from the correlators, cf. remarks in section 5.4.

D.2 Correlated fits

The standard way to fit a functional form to a set of data is to minimize a measure of the goodness of the fit as a function of the fit parameters such as

³It is prevented only by badly measured operators due to insufficient statistics.

$\{\psi, m\}$ given above. If this procedure is to be a meaningful test of the fitting function, such a measure must take into account all kind of correlations in the data $C_{ij}(t)$ between different operators at different time slices. In all our fits we use the correlated χ^2 -function where the correlation between the data points is accounted for with the covariance matrix (Cov),

$$\chi^2(\{\psi_{ni}, m_n\}) = \sum_{ijkl} \sum_{t,t'} \left(C_{ij}(t) - C_{ij}(t; \{\psi, m\}) \right) (\text{Cov})_{ijt;kl t'}^{-1} \left(C_{kl}(t') - C_{kl}(t'; \{\psi, m\}) \right), \quad (\text{D.14})$$

where the sum \sum_{ijkl} is over $i \geq j$ and $k \geq l$ only and $\sum_{t,t'}$ is meant as a sum over the fitting range $t, t' = t_{\min} \dots t_{\max}$. The (symmetric) data covariance matrix is defined as

$$(\text{Cov})_{ijt;kl t'} = \frac{1}{N(N-1)} \sum_{k=1}^N \left(C_{ij}^{(k)}(t) - \langle C_{ij}(t) \rangle \right) \left(C_{kl}^{(k)}(t') - \langle C_{kl}(t') \rangle \right). \quad (\text{D.15})$$

Here the sum is over N configurations or bins, $C_{ij}^{(k)}(t)$ denotes the value of the correlation matrix element i, j at time slice t from configuration or bin k and $\langle C_{ij}(t) \rangle = 1/N \sum_{k=1}^N C_{ij}^{(k)}(t)$. To prevent the covariance matrix from getting too large it is calculated only in the last step of the analysis, i.e. when the full correlation matrix is truncated down to the small $K \times K$ matrix $C^K(t)$ and the fitting range $t_{\min} \dots t_{\max}$ is specified. The smallness of the covariance matrix is even more important regarding the fact that the number N of configurations or bins must be at least as large as the number of columns of the covariance matrix since otherwise it contains repeated columns and is rendered singular.

For linear statistics θ it is easy to show that the covariance matrix can be calculated directly from the Jackknife samples, say $\theta^{(k)}$, through the formula

$$(\text{Cov})_{ij} = \frac{N-1}{N} \sum_{k=1}^N (\theta_i^{(k)} - \theta_i^{(\cdot)}) (\theta_j^{(k)} - \theta_j^{(\cdot)}), \quad (\text{D.16})$$

where $\theta_i^{(\cdot)} = 1/N \sum_{k=1}^N \theta_i^{(k)}$ is the average of the Jackknife samples. For non-linear statistics, however, the relation no longer holds true but the r.h.s. can still be used as an estimate for the elements of the covariance matrix. Equation (D.16) turns out to be most convenient for the analysis of the glueball correlation matrices where we are dealing with a large number of operators and therefore working with Jackknife instead of Bootstrap samples due to memory and speed limitations.

Appendix E

The cubic point group O_h

On a cubic lattice the rotation symmetry is broken down to the symmetry group of a cube, the cubic (or octahedral) group O consisting of 24 discrete rotations. In addition to the transformations of the cubic group we consider the discrete symmetry of total spatial inversion of which the eigenvalues are denoted by parity $P = \pm 1$. Combining these transformations we obtain the cubic point group $O_h = O \times Z_2$ containing 48 group elements.

E.1 The group elements of O_h

The notation for the rotations follows [103], E denoting the unity element, C_{nj} denoting a proper rotation through $2\pi/n$ in the right-hand screw sense about the axis O_j and I denoting the spatial inversion operator. All the axes involved are indicated in figure E.1.

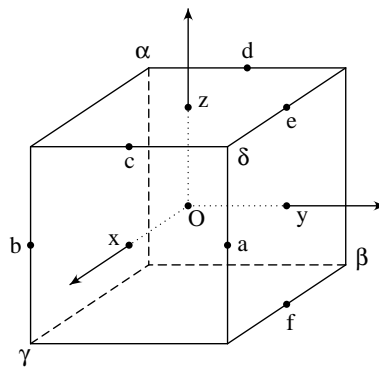


Figure E.1: The rotation axes $Oa, Ob, Oc, Od, Oe, Of, Ox, Oy, Oz, O\alpha, O\beta, O\gamma$ and $O\delta$.

An element T' of a group \mathcal{G} is said to be conjugate to another element T of \mathcal{G} if there exists an element X of \mathcal{G} such that

$$T' = XT X^{-1}. \quad (\text{E.1})$$

A set of mutually conjugate elements of \mathcal{G} is called a conjugacy class. A class can be constructed from any $T \in \mathcal{G}$ by forming the set of products XTX^{-1} for each $X \in \mathcal{G}$, keeping only the distinct elements. It is clear that, for example, the identity E forms a class by its own.

In the following the elements of the cubic point group are listed in conjugacy classes:

$$\begin{aligned}
\mathcal{C}_1 &= \{E\}, \\
\mathcal{C}_2 &= \{C_{3\alpha}, C_{3\beta}, C_{3\gamma}\}, C_{3\delta}, C_{3\alpha}^{-1}, C_{3\beta}^{-1}, C_{3\gamma}^{-1}, C_{3\delta}^{-1}\}, \\
\mathcal{C}_3 &= \{C_{2x}, C_{2y}, C_{2z}\}, \\
\mathcal{C}_4 &= \{C_{4x}, C_{4y}, C_{4z}, C_{4x}^{-1}, C_{4y}^{-1}, C_{4z}^{-1}\}, \\
\mathcal{C}_5 &= \{C_{2a}, C_{2b}, C_{2c}, C_{2d}, C_{2e}, C_{2f}\}, \\
\mathcal{C}_6 &= \{I\}, \\
\mathcal{C}_7 &= \{IC_{3\alpha}, IC_{3\beta}, IC_{3\gamma}, IC_{3\delta}, IC_{3\alpha}^{-1}, IC_{3\beta}^{-1}, IC_{3\gamma}^{-1}, IC_{3\delta}^{-1}\}, \\
\mathcal{C}_8 &= \{IC_{2x}, IC_{2y}, IC_{2z}\}, \\
\mathcal{C}_9 &= \{IC_{4x}, IC_{4y}, IC_{4z}, IC_{4x}^{-1}, IC_{4y}^{-1}, IC_{4z}^{-1}\}, \\
\mathcal{C}_{10} &= \{IC_{2a}, IC_{2b}, IC_{2c}, IC_{2d}, IC_{2e}, IC_{2f}\}.
\end{aligned} \tag{E.2}$$

Of special interest in the context of irreducible representations are the following theorems :

Theorem 1 *For a finite group \mathcal{G} the number of inequivalent irreducible representations is equal to the number of classes of \mathcal{G} .*

Theorem 2 *For a finite group \mathcal{G} , the sum of squares of the dimensions of the inequivalent irreducible representations is equal to the order of \mathcal{G} .*

Taking together both theorems, it is sufficient in the case of the cubic point group O_h to specify the dimensions of the inequivalent irreducible representations. From Theorem 1 it follows that there are five inequivalent irreducible representations for the cubic group, $\Gamma^p, p = 1, \dots, 5$, and ten for the cubic point group, respectively. In the case of the cubic group Theorem 2 amounts to the equation

$$\sum_{p=1}^5 d_p^2 = 24, \tag{E.3}$$

where d_p denotes the dimension of the corresponding irreducible representation Γ^p . The equation has a unique solution given by $\{n_1 = n_2 = 1, n_3 = 2, n_4 = n_5 = 3\}$ and thereby yielding a unique specification of the dimensions of the irreducible representations of the cubic group. The solution is trivially extended to the cubic point group since the additional irreducible representations are connected to the ones of the cubic group by the parity transformation.

In the following one-dimensional representations are denoted by A , two-dimensional irreducible representations by E and three-dimensional irreducible representations by T with superscripts \pm indicating representations that are even and odd under the parity transformation I , respectively.

E.2 The character table

The characters are a set of quantities which are the same for all equivalent representations. For finite groups (and compact Lie groups) they uniquely determine the representations up to equivalence, in particular they provide a complete specification of the irreducible representations that appear in a reducible representation Γ .

The number of times n_p that an irreducible representation Γ^p appears in a reducible representation Γ ,

$$\Gamma = n_1\Gamma^1 \oplus n_2\Gamma^2 \oplus \dots, \quad (\text{E.4})$$

is given for a finite group \mathcal{G} by

$$n_p = \frac{1}{g} \sum_{T \in \mathcal{G}} \chi(T) \chi^p(T)^*, \quad (\text{E.5})$$

where $\chi(T)$ and $\chi^p(T)$ are the characters of Γ and Γ^p , respectively, and g is the order of the group \mathcal{G} . Note that for matrix representations the character of a group element, $\chi(T)$, is simply given by the trace of the corresponding matrix representative and that the character is the same for all elements in a given conjugacy class.

In table E.2 we list for each irreducible representation $\Gamma^1, \dots, \Gamma^{10}$ of the cubic point group the characters of the conjugacy classes $\mathcal{C}_1, \dots, \mathcal{C}_{10}$.

		\mathcal{C}_1	\mathcal{C}_2	\mathcal{C}_3	\mathcal{C}_4	\mathcal{C}_5	\mathcal{C}_6	\mathcal{C}_7	\mathcal{C}_8	\mathcal{C}_9	\mathcal{C}_{10}
Γ^1	A_1^+	1	1	1	1	1	1	1	1	1	1
Γ^2	A_2^+	1	1	1	-1	-1	1	1	1	-1	-1
Γ^3	E^+	2	-1	2	0	0	2	-1	2	0	0
Γ^4	T_1^+	3	0	-1	1	-1	3	0	-1	1	-1
Γ^5	T_2^+	3	0	-1	-1	1	3	0	-1	-1	1
Γ^6	A_1^-	1	1	1	1	1	-1	-1	-1	-1	-1
Γ^7	A_2^-	1	1	1	-1	-1	-1	-1	-1	1	1
Γ^8	E^-	2	-1	2	0	0	-2	1	-2	0	0
Γ^9	T_1^-	3	0	-1	1	-1	-3	0	1	-1	1
Γ^{10}	T_2^-	3	0	-1	-1	1	-3	0	1	1	-1

Table E.1: Character table for the cubic point group.

E.3 Wave functions of glueball operators

In this section we list the orthogonal wave functions of the irreducible operators which can be built from some of the Wilson loop shapes up to length eight. The loop shape numbers correspond to the ones in figure 5.1. Each row corresponds to a given orientation of the loop shape under consideration. Notation is fixed through ordering the orientations in the following way. We construct a loop shape prototype with the path first going in 1-, then in 2- and finally, if necessary, in 3-direction as displayed in figure 5.1. From this reference orientation all others are generated by applying the group elements in the order as given in (E.2). Care

has to be taken not to generate orientations equivalent up to translations. The numbers in each row denote the contribution of the specific orientation to the wave function in question. Suitable normalization factors are understood and, according to C-parity $C = \pm 1$, the real or imaginary part has to be taken.

Consider now an example explicitly and take a look at the single plaquette operator (loop shape #1). The three (positive) orientations of the single plaquette can be labeled as O_{12}, O_{13} and O_{23} . The first E^{++} wave function is then constructed as $O^{E^{++}} = 2O_{12} - O_{13} - O_{23}$.

The two and three wave functions in the E - and T -channels, respectively, are degenerate states having the same quantum numbers and can thus be regarded as different "polarizations" belonging to the same "spin state" and transforming among each other under the cubic point group. The freedom in the choice of the orthogonal basis functions can be used to construct basis functions which are simultaneous eigenfunctions of mutually commuting group elements.

Thus for the irreducible representations of dimension greater than one (E, T_1 and T_2) we have chosen a basis of wave functions which are simultaneous eigenfunctions under the group elements C_{2x}, C_{2y}, C_{2z} and their parity transformed partners. In the E -channel the wave functions are in addition eigenfunctions under $C_{4z}, C_{4z}^{-1}, C_{2a}, C_{2b}$ and the corresponding parity transformed group elements.

In the following tables on page 107 – 113 we list the orthogonal wave functions of the irreducible operators which can be built from Wilson loops up to length eight. Note that the expressions for loop shape #8, 9, 11, 18, 20 and 22 are too lengthy and can thus not be displayed.

loop shape #1			
A_1^{++}	1	1	1
E^{++}	2	-1	-1
	0	1	-1
T_1^{+-}	0	0	1
	0	1	0
	1	0	0

loop shape #2						
A_1^{++}	1	1	1	1	1	1
A_2^{++}	1	1	1	-1	-1	-1
E^{++}	2	-1	-1	-1	-1	2
	0	1	-1	1	-1	0
E^{++}	0	1	-1	-1	1	0
	-2	1	1	-1	-1	2
T_1^{+-}	0	0	1	0	1	0
	0	1	0	1	0	0
	1	0	0	0	0	1
T_2^{+-}	1	0	0	0	0	-1
	0	0	1	0	-1	0
	0	-1	0	1	0	0

		loop shape #3									
A_1^{++}	1	1	1	1	1	1	1	1	1	1	1
E^{++}	1	-2	-2	-2	-2	1	1	1	1	1	1
	1	0	0	0	0	-1	-1	-1	-1	1	1
T_2^{++}	0	1	-1	1	-1	0	0	0	0	0	0
	-1	0	0	0	0	0	0	0	0	-1	1
	0	0	0	0	0	-1	1	1	-1	0	0
T_1^{-+}	0	1	-1	-1	1	1	-1	1	-1	0	0
	-1	-1	-1	1	1	0	0	0	0	1	-1
	-1	0	0	0	0	-1	-1	1	1	1	-1
T_2^{-+}	1	0	0	0	0	-1	-1	1	1	-1	-1
	0	1	-1	-1	1	-1	1	-1	1	0	0
	1	-1	-1	1	1	0	0	0	0	-1	1
T_1^{+-}	0	1	-1	1	-1	1	-1	-1	1	0	0
	-1	-1	-1	-1	-1	0	0	0	0	-1	1
	-1	0	0	0	0	-1	-1	-1	-1	-1	-1
T_2^{+-}	1	0	0	0	0	-1	-1	-1	-1	1	1
	0	1	-1	1	-1	-1	1	1	-1	0	0
	1	-1	-1	-1	-1	0	0	0	0	1	-1
A_1^{--}	1	1	1	-1	-1	1	1	-1	-1	-1	-1
E^{--}	1	-2	-2	2	2	1	1	-1	-1	-1	-1
	1	0	0	0	0	-1	-1	1	1	-1	-1
T_2^{--}	0	1	-1	-1	1	0	0	0	0	0	0
	-1	0	0	0	0	0	0	0	0	1	-1
	0	0	0	0	0	-1	1	-1	1	0	0

		loop shape #4			
A_1^{++}		1		1	1
T_2^{++}		1		-1	-1
		1		-1	1
		-1		-1	1
A_2^{+-}		1		-1	-1
T_1^{+-}		1		1	-1
		1		-1	1
		1		1	1

		loop shape #5		
A_1^{++}		1		1
E^{++}		2		-1
		0		1
T_1^{+-}		0		0
		0		1
		1		0

	loop shape #6											
A_1^{++}	1	1	1	1	1	1	1	1	1	1	1	1
E^{++}	1	-2	-2	-2	-2	1	1	1	1	1	1	1
	1	0	0	0	0	-1	-1	-1	-1	1	1	1
T_2^{++}	0	1	-1	1	-1	0	0	0	0	0	0	0
	-1	0	0	0	0	0	0	0	0	-1	1	1
	0	0	0	0	0	-1	1	1	-1	0	0	0
T_1^{-+}	0	1	-1	-1	1	1	-1	1	-1	0	0	0
	-1	-1	-1	1	1	0	0	0	0	1	-1	1
	-1	0	0	0	0	-1	-1	1	1	1	1	-1
T_2^{-+}	1	0	0	0	0	-1	-1	1	1	-1	-1	1
	0	1	-1	-1	1	-1	1	-1	1	0	0	0
	1	-1	-1	1	1	0	0	0	0	-1	1	-1
T_1^{+-}	0	1	-1	1	-1	1	-1	-1	1	0	0	0
	-1	-1	-1	-1	-1	0	0	0	0	-1	1	1
	-1	0	0	0	0	-1	-1	-1	-1	-1	-1	-1
T_2^{+-}	1	0	0	0	0	-1	-1	-1	-1	1	1	1
	0	1	-1	1	-1	-1	1	1	-1	0	0	0
	1	-1	-1	-1	-1	0	0	0	0	1	-1	-1
A_1^{--}	1	1	1	-1	-1	1	1	-1	-1	-1	-1	1
E^{--}	1	-2	-2	2	2	1	1	-1	-1	-1	-1	1
	1	0	0	0	0	-1	-1	1	1	-1	-1	1
T_2^{--}	0	1	-1	-1	1	0	0	0	0	0	0	0
	-1	0	0	0	0	0	0	0	0	1	-1	1
	0	0	0	0	0	-1	1	-1	1	0	0	0

loop shape #7												
A_1^{++}	1	1	1	1	1	1	1	1	1	1	1	1
E^{++}	2	-1	-1	-1	-1	-1	-1	-1	-1	2	2	2
	0	1	1	1	1	-1	-1	-1	-1	0	0	0
T_2^{++}	1	0	0	0	0	0	0	0	0	-1	-1	1
	0	0	0	0	0	-1	1	-1	1	0	0	0
	0	-1	-1	1	1	0	0	0	0	0	0	0
T_1^{+-}	1	1	-1	-1	1	0	0	0	0	1	-1	-1
	-1	0	0	0	0	-1	1	1	-1	1	-1	1
	0	-1	1	-1	1	-1	-1	1	1	0	0	0
T_2^{--}	0	1	-1	1	-1	-1	-1	1	1	0	0	0
	-1	1	-1	-1	1	0	0	0	0	-1	1	1
	1	0	0	0	0	-1	1	1	-1	-1	1	-1
A_2^{+-}	1	-1	1	1	-1	1	-1	-1	1	1	-1	-1
E^{+-}	0	1	-1	-1	1	1	-1	-1	1	0	0	0
	2	1	-1	-1	1	-1	1	1	-1	2	-2	-2
T_1^{+-}	0	0	0	0	0	1	1	-1	-1	0	0	0
	0	1	-1	1	-1	0	0	0	0	0	0	0
	-1	0	0	0	0	0	0	0	0	1	-1	1
T_1^{--}	1	1	1	1	1	0	0	0	0	1	1	1
	1	0	0	0	0	-1	-1	-1	-1	-1	-1	1
	0	1	1	-1	-1	1	-1	1	-1	0	0	0
T_2^{--}	0	1	1	-1	-1	-1	1	-1	1	0	0	0
	1	-1	-1	-1	-1	0	0	0	0	1	1	1
	1	0	0	0	0	1	1	1	1	-1	-1	1

loop shape #10							
A_1^{++}	1		1		1		1
A_2^{++}	1		1		1		-1
E^{++}	2		-1		-1		-1
	0		1		-1		1
E^{++}	0		1		-1		-1
	-2		1		1		-1
T_1^{+-}	0		0		1		0
	0		1		0		1
	1		0		0		0
T_2^{+-}	1		0		0		0
	0		0		1		0
	0		-1		0		1

loop shape #12												
A_1^{++}	1	1	1	1	1	1	1	1	1	1	1	1
A_2^{++}	1	1	1	1	1	1	-1	-1	-1	-1	-1	-1
E^{++}	2	-1	-1	-1	-1	2	-1	-1	2	-1	-1	2
	0	1	1	-1	-1	0	1	-1	0	1	-1	0
E^{++}	0	1	1	-1	-1	0	-1	1	0	-1	1	0
	-2	1	1	1	1	-2	-1	-1	2	-1	-1	2
T_1^{++}	0	0	0	1	-1	0	0	1	0	0	-1	0
	0	-1	1	0	0	0	1	0	0	-1	0	0
	-1	0	0	0	0	1	0	0	-1	0	0	1
T_2^{++}	1	0	0	0	0	-1	0	0	-1	0	0	1
	0	0	0	-1	1	0	0	1	0	0	-1	0
	0	-1	1	0	0	0	-1	0	0	1	0	0
T_1^{+-}	1	0	0	0	0	-1	1	0	0	-1	0	0
	0	0	0	-1	1	0	0	0	1	0	0	1
	0	1	1	0	0	0	0	1	0	0	-1	0
T_1^{+-}	0	1	-1	0	0	0	0	0	-1	0	0	1
	1	0	0	0	0	1	0	1	0	0	1	0
	0	0	0	1	1	0	1	0	0	1	0	0
T_2^{+-}	0	1	1	0	0	0	0	-1	0	0	1	0
	1	0	0	0	0	-1	-1	0	0	1	0	0
	0	0	0	1	-1	0	0	0	1	0	0	1
T_2^{+-}	0	0	0	1	1	0	-1	0	0	-1	0	0
	0	1	-1	0	0	0	0	0	1	0	0	-1
	-1	0	0	0	0	-1	0	1	0	0	1	0

loop shape #13						
A_1^{++}	1	1	1	1	1	1
E^{++}	1	1	1	-2	-2	1
	-1	1	1	0	0	-1
T_2^{-+}	0	0	0	1	-1	0
	0	-1	1	0	0	0
	-1	0	0	0	0	1
T_1^{+-}	0	1	-1	0	0	0
	1	0	0	0	0	1
	0	0	0	1	1	0
A_2^{--}	1	-1	-1	1	-1	-1
E^{--}	1	1	1	0	0	-1
	1	-1	-1	-2	2	-1

loop shape #14												
A_1^{++}	1	1	1	1	1	1	1	1	1	1	1	1
E^{++}	1	-2	-2	-2	-2	1	1	1	1	1	1	1
	1	0	0	0	0	-1	-1	-1	-1	1	1	1
T_1^{++}	0	1	-1	-1	1	-1	1	-1	1	0	0	0
	-1	1	1	-1	-1	0	0	0	0	1	-1	1
	1	0	0	0	0	-1	-1	1	1	-1	-1	1
T_2^{++}	1	0	0	0	0	1	1	-1	-1	-1	-1	1
	0	-1	1	1	-1	-1	1	-1	1	0	0	0
	-1	-1	-1	1	1	0	0	0	0	1	-1	1
T_2^{+-}	0	1	-1	1	-1	0	0	0	0	0	0	0
	-1	0	0	0	0	0	0	0	0	-1	1	1
	0	0	0	0	0	-1	1	1	-1	0	0	0
A_2^{+-}	1	-1	1	-1	1	1	1	-1	-1	-1	-1	1
E^{+-}	1	0	0	0	0	-1	-1	1	1	-1	-1	1
	-1	-2	2	-2	2	-1	-1	1	1	1	1	-1
T_1^{+-}	1	0	0	0	0	0	0	0	0	-1	1	-1
	0	0	0	0	0	-1	1	-1	1	0	0	0
	0	1	1	1	1	0	0	0	0	0	0	0
T_1^{--}	0	1	1	-1	-1	-1	1	1	-1	0	0	0
	1	-1	1	1	-1	0	0	0	0	1	-1	-1
	1	0	0	0	0	1	1	1	1	1	1	1
T_2^{+-}	1	0	0	0	0	-1	-1	-1	-1	1	1	1
	0	-1	-1	1	1	-1	1	1	-1	0	0	0
	1	1	-1	-1	1	0	0	0	0	1	-1	-1

loop shape #15			
A_1^{++}		1	1
E^{++}		2	-1
		0	1
T_1^{+-}		0	0
		0	1
		1	0

loop shape #16						
A_1^{++}	1	1	1	1	1	1
A_2^{++}	1	1	1	-1	-1	-1
E^{++}	2	-1	-1	-1	-1	2
	0	1	-1	1	-1	0
E^{+-}	0	1	-1	-1	1	0
	-2	1	1	-1	-1	2
T_1^{--}	0	1	0	0	0	1
	1	0	0	0	-1	0
	0	0	-1	-1	0	0
T_2^{--}	0	0	1	-1	0	0
	0	-1	0	0	0	1
	1	0	0	0	1	0

loop shape #17						
A_1^{++}	1	1	1	1	1	1
E^{++}	2	-1	-1	-1	-1	2
	0	1	1	-1	-1	0
T_2^{++}	1	0	0	0	0	-1
	0	0	0	-1	1	0
	0	-1	1	0	0	0
T_1^{--}	1	1	1	0	0	1
	1	0	0	-1	-1	-1
	0	1	-1	1	-1	0
T_2^{--}	0	1	-1	-1	1	0
	1	-1	-1	0	0	1
	1	0	0	1	1	-1

loop shape #19						
A_1^{++}	1	1	1	1	1	1
E^{++}	2	-1	-1	-1	-1	2
	0	1	1	-1	-1	0
T_2^{++}	1	0	0	0	0	-1
	0	0	0	-1	1	0
	0	-1	1	0	0	0
A_2^{+-}	1	1	-1	-1	1	-1
E^{+-}	0	1	-1	1	-1	0
	-2	1	-1	-1	1	2
T_1^{+-}	0	0	0	1	1	0
	0	1	1	0	0	0
	1	0	0	0	0	1

	loop shape #21											
A_1^{++}	1	1	1	1	1	1	1	1	1	1	1	1
E^{++}	1	1	1	1	1	-2	-2	-2	-2	1	1	1
	-1	1	1	1	1	0	0	0	0	-1	-1	-1
T_2^{++}	0	0	0	0	0	1	1	-1	-1	0	0	0
	0	-1	1	1	-1	0	0	0	0	0	0	0
	-1	0	0	0	0	0	0	0	0	1	-1	1
T_1^{-+}	1	0	0	0	0	1	-1	1	-1	1	-1	-1
	0	-1	-1	1	1	-1	1	1	-1	0	0	0
	-1	-1	1	-1	1	0	0	0	0	1	1	-1
T_2^{-+}	1	-1	1	-1	1	0	0	0	0	-1	-1	1
	1	0	0	0	0	-1	1	-1	1	1	-1	-1
	0	-1	-1	1	1	1	-1	-1	1	0	0	0
T_1^{+-}	1	0	0	0	0	1	1	-1	-1	-1	1	-1
	0	-1	1	1	-1	1	1	1	1	0	0	0
	1	1	1	1	1	0	0	0	0	1	1	1
T_2^{+-}	1	-1	-1	-1	-1	0	0	0	0	1	1	1
	-1	0	0	0	0	1	1	-1	-1	1	-1	1
	0	1	-1	-1	1	1	1	1	1	0	0	0
A_2^{--}	1	-1	1	-1	1	-1	1	1	-1	-1	-1	1
E^{--}	1	1	-1	1	-1	0	0	0	0	-1	-1	1
	1	-1	1	-1	1	2	-2	-2	2	-1	-1	1
T_1^{--}	0	1	1	-1	-1	0	0	0	0	0	0	0
	1	0	0	0	0	0	0	0	0	1	-1	-1
	0	0	0	0	0	-1	1	-1	1	0	0	0

Appendix F

Collection of data

F.1 Data from the static potential

β	fit range	V_0	α	σ	χ^2/N_{DF}
3.400	2 - 6	0.7805(7)	-0.251(9)	0.0629(13)	1.02
3.150	2 - 5	0.820(15)	-0.286(19)	0.0992(27)	0.75
3.150	2 - 6	0.804(14)	-0.264(17)	0.1017(25)	1.03
2.927	2 - 6	0.812(16)	-0.272(20)	0.1606(33)	1.35
2.860	1 - 4	0.8007(48)	-0.2623(33)	0.1885(17)	1.17
2.860	2 - 4	0.789(38)	-0.291(43)	0.1844(72)	1.41
2.680	1 - 4	0.7766(52)	-0.2547(37)	0.2871(15)	0.43
2.680	2 - 6	0.778(41)	-0.256(54)	0.2868(70)	0.65
2.361	1 - 4	0.615(11)	-0.1791(78)	0.6286(37)	0.99
2.361	2 - 5	0.59(11)	-0.15(13)	0.634(22)	1.41

Table F.1: Results from correlated fits of the form (4.4) to the static quark potentials. The second column indicates the fit range in r and the last two columns the value of c from which r_0 is determined through (4.5) and χ^2 per degree of freedom, χ^2/N_{DF} , respectively.

β	r	N_{op}	fit range	$V(r)$	χ^2/N_{DF}
3.400	1	5	2 - 6	0.5874(2)	0.76
	2	5	2 - 6	0.7804(5)	2.19
	3	5	3 - 6	0.885(2)	1.27
	4	3	3 - 6	0.969(3)	1.24
	5	4	2 - 6	1.046(4)	0.91
	6	4	2 - 5	1.116(8)	0.38
	7	3	3 - 6	1.17(2)	0.18
3.150	1	5	3 - 5	0.6405(3)	0.77
	2	4	2 - 6	0.8756(5)	0.63
	3	5	2 - 6	1.022(2)	0.43
	4	3	2 - 5	1.147(2)	0.15
	5	3	2 - 6	1.258(3)	0.84
	6	3	2 - 6	1.38(1)	1.08
2.927	1	4	2 - 7	0.7032(2)	0.42
	2	3	2 - 7	0.9969(5)	0.65
	3	3	2 - 7	1.202(2)	0.56
	4	4	2 - 5	1.383(5)	0.31
	5	3	2 - 7	1.560(8)	0.81
	6	3	2 - 5	1.71(2)	0.82
	7	2	2 - 6	1.92(3)	1.28
2.860	1	3	2 - 4	0.7267(4)	1.50
	2	3	1 - 4	1.047(1)	0.56
	3	4	1 - 4	1.278(2)	0.68
	4	2	2 - 4	1.488(5)	0.30
	5	3	2 - 4	1.67(2)	0.68
2.680	1	4	2 - 6	0.8091(3)	0.21
	2	4	2 - 6	1.2231(9)	0.98
	3	4	2 - 6	1.553(3)	0.33
	4	3	1 - 5	1.862(3)	0.33
	5	2	2 - 6	2.15(3)	0.89
	6	2	2 - 5	2.51(8)	0.14
2.361	1	3	2 - 5	1.0641(6)	0.33
	2	3	1 - 6	1.783(1)	0.31
	3	2	1 - 5	2.443(4)	0.75
	4	2	1 - 6	3.09(2)	0.84
	5	1	1 - 5	3.73(6)	2.31
	6	1	1 - 6	4.5(3)	0.44

Table F.2: Potential values extracted from fits of the form $Z(r) \exp(-tV(r))$ to the ground state of the Wilson loop correlators. Note that $t_0 = 1$ and $t_1 = 2$ was chosen in all cases. The column entitled with N_{op} denotes the number of operators kept after the first truncation.

F.2 Data from the glueball simulations

Channel	t_0/t_1	N_{op}	fit range	χ^2/N_{DF}	energies
A_1^{++}	1/2	6	1 - 4	0.79	0.836(23)
	0/1	30	1 - 4	0.54	0.835(20)
E^{++}	1/2	11	1 - 4	0.03	1.233(48)
		8	1 - 4	0.19	1.271(34)
T_2^{++}	0/1	60	1 - 4	0.02	1.232(23)
	1/2	5	1 - 4	0.40	1.234(28)
A_1^{-+}		7	1 - 4	0.16	1.202(31)
	0/1	48	1 - 4	1.16	1.247(21)
E^{-+}	1/2	3	1 - 3	0.24	1.395(86)
	0/1	15	1 - 3	0.12	1.458(52)
T_2^{-+}		15	2 - 4	0.10	1.38(20)
	1/2	3	1 - 3	0.34	1.681(72)
T_1^{+-}	1/2	4	1 - 3	0.09	1.631(72)
	1/2	8	1 - 3	2.49	1.64(16)
		6	1 - 3	0.17	1.76(10)
	0/1	25	1 - 3	0.07	1.654(55)

Table F.3: Results from fits to the $\beta = 3.40$ glueball correlators on the 14^4 lattice obtained from the large simulation.

Channel	t_0/t_1	N_{op}	fit range	χ^2/N_{DF}	energies
A_1^{++}	1/2	5	1 - 3	0.50	0.831(33)
	2/3	3	1 - 3	0.50	0.839(32)
	0/1	7	1 - 3	0.94	0.813(27)

Table F.4: Results from fits to the $\beta = 3.40$ glueball correlators on the 14^4 lattice obtained from the small simulation where only five loop shapes were measured on five smearing schemes.

Channel	t_0/t_1	N_{op}	fit range	χ^2/N_{DF}	energies
A_1^{++}	1/2	5	1 - 3	0.61	1.034(33)
			2 - 3	0.00	1.10(10)
			1 - 4	2.02	1.032(32)
			2 - 4	1.07	1.12(11)
E^{++}	0/1	25	1 - 4	1.62	1.017(28)
			2 - 4	0.02	1.119(92)
T_2^{++}	1/2	4	1 - 3	1.26	1.534(62)
			0/1	48	1 - 3
A_1^{-+}	1/2	3	1 - 3	0.84	1.65(18)
			0/1	48	2 - 4
E^{-+}	1/2	3	1 - 3	0.00	1.97(20)
			0/1	15	1 - 3
T_2^{-+}	1/2	5	1 - 3	0.00	1.39(27)
			0/1	22	1 - 3
T_1^{+-}	1/2	4	1 - 3	2.70	2.10(18)
			0/1	25	1 - 3

Table F.5: Results from fits to the $\beta = 3.15$ glueball correlators on the 12^4 lattice.

Channel	t_0/t_1	N_{op}	fit range	χ^2/N_{DF}	energies		
A_1^{++}	1/2	3	1 - 4	0.02	1.411(96)		
			2 - 4	0.02	1.40(38)		
			0/1	25	1 - 4	0.56	1.378(80)
			2 - 4	0.36	1.50(40)		

Table F.6: Results from fits to the $\beta = 2.86$ glueball correlator on the 10^4 lattice. Only five loop shapes were measured on 5 different smearing schemes.

Bibliography

- [1] K. G. Wilson, Phys. Rev. **D10**, 2445 (1974).
- [2] P. Hasenfratz and F. Niedermayer, Nucl. Phys. **B414**, 785 (1994), hep-lat/9308004.
- [3] M. Blatter, R. Burkhalter, P. Hasenfratz, and F. Niedermayer, Phys. Rev. **D53**, 923 (1996), hep-lat/9508028.
- [4] R. Burkhalter, Phys. Rev. **D54**, 4121 (1996), hep-lat/9512032.
- [5] T. DeGrand, A. Hasenfratz, P. Hasenfratz, and F. Niedermayer, Nucl. Phys. **B454**, 587 (1995), hep-lat/9506030.
- [6] T. DeGrand, A. Hasenfratz, P. Hasenfratz, and F. Niedermayer, Nucl. Phys. **B454**, 615 (1995), hep-lat/9506031.
- [7] T. DeGrand, A. Hasenfratz, P. Hasenfratz, and F. Niedermayer, Phys. Lett. **B365**, 233 (1996), hep-lat/9508024.
- [8] M. Blatter and F. Niedermayer, Nucl. Phys. **B482**, 286 (1996), hep-lat/9605017.
- [9] T. DeGrand, A. Hasenfratz, P. Hasenfratz, P. Kunszt, and F. Niedermayer, Nucl. Phys. Proc. Suppl. **53**, 942 (1997), hep-lat/9608056.
- [10] P. Kunszt, Nucl. Phys. **B516**, 402 (1998), hep-lat/9706019.
- [11] T. DeGrand, A. Hasenfratz, and D. Zhu, Nucl. Phys. **B475**, 321 (1996), hep-lat/9603015.
- [12] T. DeGrand, A. Hasenfratz, and D. cai Zhu, Nucl. Phys. **B478**, 349 (1996), hep-lat/9604018.
- [13] T. DeGrand, A. Hasenfratz, and T. G. Kovacs, Nucl. Phys. **B505**, 417 (1997), hep-lat/9705009.
- [14] F. Farchioni and A. Papa, Phys. Rev. **D58**, 054502 (1998), hep-lat/9711030.
- [15] P. Hasenfratz, Nucl. Phys. **B525**, 401 (1998), hep-lat/9802007.
- [16] P. Hasenfratz, V. Laliena, and F. Niedermayer, Phys. Lett. **B427**, 125 (1998), hep-lat/9801021.

-
- [17] MILC, T. DeGrand, Phys. Rev. **D58**, 094503 (1998), hep-lat/9802012.
Phys. Rev. **D60**, 094501 (1999), hep-lat/9903006.
- [18] C. Bernard and T. DeGrand, (1999), hep-lat/9909083.
- [19] M. Stephenson, C. DeTar, T. DeGrand, and A. Hasenfratz, (1999), hep-lat/9910023.
- [20] MILC, C. Bernard *et al.*, (1999), hep-lat/9912018.
- [21] P. Hasenfratz *et al.*, (2000), hep-lat/0003013.
- [22] A. M. Polyakov, Phys. Lett. **B72**, 477 (1978).
- [23] L. Susskind, Phys. Rev. **D20**, 2610 (1979).
- [24] J. Kuti, J. Polonyi, and K. Szlachanyi, Phys. Lett. **B98**, 199 (1981).
- [25] A. V. Smilga, Ann. Phys. **234**, 1 (1994).
- [26] N. H. Christ and A. E. Terrano, Phys. Rev. Lett. **56**, 111 (1986).
- [27] M. Creutz, *Quarks, Gluons and Lattices* (Cambridge University Press, 1983).
- [28] H. J. Rothe, *Lattice Gauge Theories. An Introduction.* (World Scientific Lecture Notes in Physics, Vol. 43, 1992).
- [29] A. V. Smilga, Phys. Rept. **291**, 1 (1997), hep-ph/9612347.
- [30] N. Weiss, Phys. Rev. **D24**, 475 (1981).
- [31] N. Weiss, Phys. Rev. **D25**, 2667 (1982).
- [32] J. Polonyi and K. Szlachanyi, Phys. Lett. **B110**, 395 (1982).
- [33] L. G. Yaffe and B. Svetitsky, Phys. Rev. **D26**, 963 (1982).
- [34] B. Svetitsky and L. G. Yaffe, Nucl. Phys. **B210**, 423 (1982).
- [35] J. Engels *et al.*, Nucl. Phys. **B280**, 577 (1987).
- [36] J. Engels, J. Fingberg, and M. Weber, Nucl. Phys. **B332**, 737 (1990).
- [37] M. Fukugita, M. Okawa, and A. Ukawa, Nucl. Phys. **B337**, 181 (1990).
- [38] S. A. Gottlieb *et al.*, Phys. Rev. Lett. **55**, 1958 (1985).
- [39] A. D. Kennedy, J. Kuti, S. Meyer, and B. J. Pendleton, Phys. Rev. Lett. **54**, 87 (1985).
- [40] F. R. Brown, N. H. Christ, Y. F. Deng, M. S. Gao, and T. J. Woch, Phys. Rev. Lett. **61**, 2058 (1988).
- [41] Y. Iwasaki, K. Kanaya, T. Kaneko, and T. Yoshie, Nucl. Phys. Proc. Suppl. **53**, 429 (1997), hep-lat/9608090.
- [42] Y. Iwasaki, K. Kanaya, T. Kaneko, and T. Yoshie, Phys. Rev. **D56**, 151 (1997), hep-lat/9610023.

-
- [43] I. R. McDonald and K. Singer, *Discuss. Faraday Soc.* **43**, 40 (1967).
- [44] M. Falcioni, E. Marinari, M. L. Paciello, G. Parisi, and B. Taglienti, *Phys. Lett.* **B108**, 331 (1982).
- [45] A. M. Ferrenberg and R. H. Swendsen, *Phys. Rev. Lett.* **63**, 1195 (1989).
- [46] A. M. Ferrenberg and R. H. Swendsen, *Phys. Rev. Lett.* **61**, 2635 (1988).
- [47] G. Boyd *et al.*, *Nucl. Phys.* **B469**, 419 (1996), hep-lat/9602007.
- [48] F. Karsch and M. Lutgemeier, *Nucl. Phys.* **B550**, 449 (1999), hep-lat/9812023.
- [49] B. Beinlich, F. Karsch, E. Laermann, and A. Peikert, *Eur. Phys. J.* **C6**, 133 (1999), hep-lat/9707023.
- [50] B. Efron, *The Jackknife, the Bootstrap and other Resampling Plans* (SIAM, 1982).
- [51] B. Efron and R. J. Tibshirani, *An Introduction to the Bootstrap* (Monographs on Statistics and Applied Probability, Vol. 57, 1993).
- [52] A. Papa, *Nucl. Phys.* **B478**, 335 (1996), hep-lat/9605004.
- [53] S. Spiegel, *Phys. Lett.* **B400**, 352 (1997), hep-lat/9611027.
- [54] A. Gall, Diploma work (Univ. Bern (1995), unpublished).
- [55] C. B. Lang and C. Rebbi, *Phys. Lett.* **B115**, 137 (1982).
- [56] M. Alford, W. Dimm, G. P. Lepage, G. Hockney, and P. B. Mackenzie, *Phys. Lett.* **B361**, 87 (1995), hep-lat/9507010.
- [57] R. Balian, J. M. Drouffe, and C. Itzykson, *Phys. Rev.* **D11**, 2104 (1975).
- [58] G. Munster, *Nucl. Phys.* **B180**, 23 (1981).
- [59] E. Eichten, K. Gottfried, T. Kinoshita, K. D. Lane, and T. M. Yan, *Phys. Rev.* **D21**, 203 (1980).
- [60] G. Parisi, R. Petronzio, and F. Rapuano, *Phys. Lett.* **B128**, 418 (1983).
- [61] APE, M. Albanese *et al.*, *Phys. Lett.* **B192**, 163 (1987).
- [62] R. Sommer, *Nucl. Phys.* **B411**, 839 (1994), hep-lat/9310022.
- [63] J. L. Richardson, *Phys. Lett.* **B82**, 272 (1979).
- [64] ALPHA, M. Guagnelli, R. Sommer, and H. Wittig, *Nucl. Phys.* **B535**, 389 (1998), hep-lat/9806005.
- [65] R. G. Edwards, U. M. Heller, and T. R. Klassen, *Nucl. Phys.* **B517**, 377 (1998), hep-lat/9711003.
- [66] G. S. Bali and K. Schilling, *Phys. Rev.* **D46**, 2636 (1992).
- [67] G. S. Bali and K. Schilling, *Phys. Rev.* **D47**, 661 (1993), hep-lat/9208028.

-
- [68] QCD-TARO, P. de Forcrand *et al.*, (1999), hep-lat/9911033.
- [69] D. W. Bliss, K. Hornbostel, and G. P. Lepage, (1996), hep-lat/9605041.
- [70] M. J. Teper, (1998), hep-th/9812187.
- [71] Y. Iwasaki, Nucl. Phys. **B258**, 141 (1985).
- [72] SESAM, G. S. Bali *et al.*, Nucl. Phys. Proc. Suppl. **63**, 209 (1998), hep-lat/9710012.
- [73] D. Toussaint, (1999), hep-lat/9909088.
- [74] SESAM, G. S. Bali *et al.*, Nucl. Phys. Proc. Suppl. **53**, 239 (1997), hep-lat/9608096.
- [75] SESAM, G. S. Bali *et al.*, (2000), hep-lat/0003012.
- [76] UKQCD, C. Michael, M. S. Foster, and C. McNeile, (1999), hep-lat/9909036.
- [77] S. Godfrey and J. Napolitano, Rev. Mod. Phys. **71**, 1411 (1999), hep-ph/9811410.
- [78] K. Ishikawa, G. Schierholz, and M. Teper, Z. Phys. **C19**, 327 (1983).
- [79] C. J. Morningstar and M. Peardon, Phys. Rev. **D56**, 4043 (1997), hep-lat/9704011.
- [80] C. J. Morningstar and M. Peardon, Phys. Rev. **D60**, 034509 (1999), hep-lat/9901004.
- [81] UKQCD, G. S. Bali *et al.*, Phys. Lett. **B309**, 378 (1993), hep-lat/9304012.
- [82] H. Chen, J. Sexton, A. Vaccarino, and D. Weingarten, Nucl. Phys. Proc. Suppl. **34**, 357 (1994), hep-lat/9401020.
- [83] A. Vaccarino and D. Weingarten, Phys. Rev. **D60**, 114501 (1999), hep-lat/9910007.
- [84] I. Montvay and G. Muenster, *Quantum fields on a lattice* (Cambridge monographs on mathematical physics, 1994).
- [85] B. Berg and A. Billoire, Nucl. Phys. **B221**, 109 (1983).
- [86] H. Wittig, (1999), hep-ph/9911400.
- [87] K. Symanzik, Nucl. Phys. **B226**, 187 (1983).
- [88] K. Symanzik, Nucl. Phys. **B226**, 205 (1983).
- [89] P. Weisz, Nucl. Phys. **B212**, 1 (1983).
- [90] P. Weisz and R. Wohlert, Nucl. Phys. **B236**, 397 (1984).
- [91] M. Luscher and P. Weisz, Commun. Math. Phys. **97**, 59 (1985).
- [92] M. Luscher and P. Weisz, Phys. Lett. **B158**, 250 (1985).

-
- [93] M. Kremer *et al.*, Nucl. Phys. **B305**, 109 (1988).
 - [94] D. J. R. Pugh and M. Teper, Phys. Lett. **B224**, 159 (1989).
 - [95] P. Hasenfratz, Contributed to Lattice 93, Dallas, TX, Oct 1993.
 - [96] F. Niedermayer, Prepared for LATTICE 93: 11th International Symposium on Lattice Field Theory, Dallas, TX, 12-16 Oct 1993.
 - [97] M. Blatter, R. Burkhalter, P. Hasenfratz, and F. Niedermayer, Nucl. Phys. Proc. Suppl. **42**, 799 (1995), hep-lat/9411068.
 - [98] M. L. Laursen, J. Smit, and J. C. Vink, Nucl. Phys. **B343**, 522 (1990).
 - [99] A. E. Ferdinand and M. E. Fisher, Phys. Rev. **185**, 832 (1969).
 - [100] R. H. Swendsen and J.-S. Wang, Phys. Rev. Lett. **58**, 86 (1987).
 - [101] R. B. Potts, Proc. Camb. Phil. Soc. **48**, 106 (1952).
 - [102] F. Y. Wu, Rev. Mod. Phys. **54**, 235 (1982).
 - [103] J. Cornwell, *Group theory in physics* (Academic Press, 1984).

Acknowledgments

It is a pleasure to thank Philipp Rüfenacht and Ferenc Niedermayer for many enjoyable discussions and a very pleasant collaboration. I also thank Peter Hasenfrazz for his continuous support and help during the thesis. I am especially indebted to Ferenc and Peter for reading the manuscript carefully.

Then, I am grateful to all the people at the institute for provoking my social skills. Especially Thomas Becher, Alex Gall, Jürg Käppeli, Roland Kaiser and Patrick Liniger are responsible for crucially improving my quality of life over the last years.

I will not miss the opportunity to thank Andrea for her comprehension and support in many ways.

Finally, I would like to thank whoever belongs to my family for just being there.

Curriculum vitae

Personal Data

Name Wenger, Urs Rudolf
Date of birth 27. 5. 1971
Place of birth Thun
Nationality Swiss
Marital status Unmarried
Present adress Institute for Theoretical Physics
 University of Bern
 Sidlerstr. 5
 CH-3012 Bern
 E-mail: wenger@itp.unibe.ch

Schools

1978-1982 Primary school in Thun
1982-1987 Secondary school in Thun
1987-1990 Gymnasium in Thun,
 completed with Eidgenössische Matura Typus C

University

1991-1996 University of Bern,
 Studies in physics, mathematics and philosophy
1996 University of Bern,
 Diploma in theoretical physics
 “CP-violation in effective field theories”
 Supervisor: Prof. J. Gasser
1997-2000 University of Bern,
 PhD student of Prof. P. Hasenfratz:
 “Lattice gauge theory with fixed point actions”